

# Multiparametric bioprocess monitoring based on automated fluorescence microscopy and image processing

Vorgelegt von

Diplom Ingenieur Andreas Balzer  
Novartis Pharma AG Basel, Schweiz

Fakultät III – Prozesswissenschaften  
der Technischen Universität Berlin

Zur Erlangung des akademischen Grades  
Doktor der Ingenieurwissenschaften  
- Dr.-Ing. –

genehmigte Dissertation

Promotionsausschuß:

Vorsitzender :	Prof. Dipl. Ing. Dr. Ulf Stahl
Berichter:	Prof. Dr. rer. nat. Rainer Buchholz
Berichter:	Prof. Dr. rer. nat. Thomas H. Scheper
Berichter:	Dr. rer. nat. Christian Leist

Tag der wissenschaftlichen Aussprache: 28. Mai 2001

Berlin 2001

D 83

A PICTURE IS WORTH A THOUSANDS WORDS

(unknown)

## **Acknowledgments / Danksagung**

Herrn Prof. Dr. R. Buchholz danke ich herzlich für sein Interesse an meiner Arbeit und für die interessanten Diskussionen und Anregungen während meiner Besuche in Berlin.

Herrn Prof. Dr. T. Scheper danke ich für die Übernahme des Zweitgutachtens und sein Interesse bei der Vorstellung meiner Arbeit in Hannover.

Mein besonderer Dank gilt Dr. Christian Leist, welcher mich während der gesamten Arbeit betreut hat und mir mit vielen Ideen und Ratschlägen zur Seite stand. Darüber hinaus möchte ich ihm auch für die Freiheit danken, die ich in diesem Projekt hatte und die Möglichkeit all das zu realisieren was zu dieser Arbeit geführt hat.

Herrn Dipl. Ing. Jörg Schmidt möchte ich danken für die vielen kreativen Ideen und Diskussionen die wesentlich zum Gelingen dieser Arbeit beigetragen haben.

Ohne die Hilfe Simon Bianchi, Renato Moraschi, Jean-Michel Kessler und Noel Boesinger wäre eine Realisierung dieses Projektes nie möglich gewesen, da nur durch ihre Arbeit der grösste Teil der Zellkultivierungen durchgeführt werden konnte, welche die Basis für die ausgiebigen Tests der entwickelten Algorithmen und des fertigen Systems bildeten.

Besonders möchte ich Marcello Marangi danken der durch sein Interesse an meiner Arbeit, seinen vielen Ideen und Tips mich immer wieder aufs Neue motiviert hat und dem es zu verdanken ist, dass von vornherein das fertige System routinemässig zur Überwachung der laufenden Zellkulturprozesse in der Entwicklung der Novartis Pharma AG eingesetzt wurde.

Dr. Jochen Kuhla danke ich für die vielen Gespräche und Diskussionen und auch die Möglichkeit mal wieder ein bisschen Abstand zu meiner Arbeit zu gewinnen.

Barbara Hess möchte ich danken, die mir nicht nur im Labor immer wieder geholfen hat, sondern mich auch sonst immer wieder gestützt hat, wenn etwas nicht auf Anhieb funktioniert hat.

Besonders bedanken möchte ich mich auch bei Peter Bolt und Stephanie Schäfer die während ihrer Diplomarbeiten einen wesentlichen Beitrag zum Gelingen dieser Arbeit geleistet haben.

Bedanken möchte ich mich auch bei Eric Weber der den ersten Grundstein zum Entstehen dieser Arbeit geleistet hat.

Für die nächtelangen Diskussionen über Image Processing, Labview Programmierung und der kritischen Prüfung, ob denn auch alles noch der Physik entspricht was ich da mache, möchte ich mich bei meinem Onkel Axel bedanken, von dem ich eine Menge lernen konnte, auch wenn ich immer noch nicht richtig rechnen kann.

Ohne die Hilfe von Sabine Schreck und ihrer kritischen Korrektur dieser Arbeit, hätte ich den Fehlerteufel nie besiegt, dafür kann ich ihr gar nicht genug danken.

Mein besonderer Dank gilt meiner Freundin für ihre unendliche Geduld, mit der sie mich ohne zu zögern, während ich Nächte lang am Computer sass oder sogar noch am Wochenende oder im Urlaub am Laptop gesessen habe, mit allem notwendigen versorgt und umsorgt hat, was man neben Bits und Bytes noch so zum Leben braucht.

Zum Schluss möchte ich mich noch bei meinen und den Eltern meiner Freundin bedanken, die bis jetzt all meine Schritte gespannt verfolgt haben und auch, wenn sie wieder fragen werden „wofür“, all die Zeit einen erheblichen Teil dazu beigetragen haben, das ich nun diese Arbeit schreiben konnte.

## Table of contents

<b>ABBREVIATIONS AND DEFINITIONS .....</b>	<b>IV</b>
<b>SUMMARY.....</b>	<b>VI</b>
<b>ZUSAMMENFASSUNG .....</b>	<b>VIII</b>
<b>1. INTRODUCTION .....</b>	<b>1</b>
1.1. PRODUCTION OF BIOPHARMACEUTICALS .....	1
1.2. PROCESS CONTROL DURING BIOPHARMACEUTICAL PRODUCTION.....	2
1.3. LOSS OF PRODUCTIVITY DURING CULTIVATION.....	3
1.3.1. <i>Stability of mammalian cell lines</i> .....	3
1.3.2. <i>Cell Death during cultivation of commercially important cell lines</i> .....	3
1.4. PROCESS OPTIMIZATION STRATEGIES .....	5
1.4.1. <i>Genetic engineering of production cell lines</i> .....	6
1.4.2. <i>Feeding Strategies</i> .....	6
1.5. MICROSCOPY, IMAGE PROCESSING AND ANALYSIS IN BIOTECHNOLOGY.....	7
1.5.1. <i>Comparison of human and artificial perception</i> .....	7
1.5.2. <i>Application of image processing and image analysis in bioscience</i> .....	9
<b>2. AIMS OF THE WORK.....</b>	<b>13</b>
<b>3. MATERIALS .....</b>	<b>14</b>
3.1. NEWLY DEVELOPED OR MODIFIED DEVICES .....	14
3.1.1. <i>Microscope</i> .....	14
3.1.2. <i>Liquid Handling and Staining System</i> .....	14
3.1.3. <i>Flow-Through-Chamber</i> .....	17
3.1.4. <i>Mixing-Chamber</i> .....	19
3.2. STANDARD MATERIALS .....	21
3.2.1. <i>Computer</i> .....	21
3.2.2. <i>CCD Camera and Framegrabber</i> .....	21
3.2.3. <i>Fluorescent Dye 4',6-diamidino-2-phenylindole (DAPI)</i> .....	21
3.2.4. <i>Microspheres for Autofocus Calibration</i> .....	22
3.2.5. <i>Cell Cultivation</i> .....	22
3.2.6. <i>Media</i> .....	22
3.2.7. <i>Analytics</i> .....	22
3.2.8. <i>CIP-Soution</i> .....	22
3.2.9. <i>Hemocytometer – Trypan blue dye-exclusion method</i> .....	23
3.2.10. <i>Induction of Apoptosis - Actinomycin D</i> .....	23
<b>4. METHODS .....</b>	<b>24</b>
4.1. SOFTWARE CONCEPT.....	24

4.1.1.	<i>Script language</i> .....	27
4.2.	SCANNING PROCEDURES – FULLSCAN AND SNAPSCAN.....	29
4.2.1.	<i>Scanning at different focal planes - FullScan</i> .....	29
4.2.2.	<i>Time resolved Scans – SnapScans</i> .....	31
4.3.	PRINCIPLES OF IMAGE PROCESSING ALGORITHMS .....	32
4.3.1.	<i>“Out-of-focus” algorithm</i> .....	32
4.3.2.	<i>“Nearly-in-focus” algorithm</i> .....	35
4.3.3.	<i>Morphological Parameters</i> .....	41
4.3.4.	<i>“In-focus” algorithm</i> .....	41
4.4.	OVERVIEW OF USED ALGORITHMS AND CALCULATION FORMULAS .....	42
4.5.	AUTOFOCUS CALIBRATION PROCEDURE.....	44
<b>5.</b>	<b>RESULTS</b> .....	<b>45</b>
5.1.	COMPARISON OF DIFFERENT AUTO-FOCUS FUNCTIONS.....	45
5.1.1.	<i>Evaluation of autofocus functions on bright-field images</i> .....	47
5.1.2.	<i>Autofocus functions applied to bright field and fluorescence images sets</i> .....	49
5.1.3.	<i>Focus Functions and Microspheres</i> .....	52
5.1.4.	<i>Implemented autofocus calibration procedure</i> .....	52
5.2.	MORPHOLOGICAL STUDIES - SNAPSCANS.....	54
5.2.1.	<i>Bright Field Focal Plane SnapScan</i> .....	54
5.2.2.	<i>Two focal plane SnapScan</i> .....	57
5.2.3.	<i>Blebbing and Dying of Cells – Two focal plane SnapScan</i> .....	60
5.3.	ANALYSIS OF FULLSCANS.....	62
5.3.1.	<i>Refractive activity and fluorescent events</i> .....	62
5.4.	AUTOMATED DETERMINATION OF CELL NUMBER AND VIABILITY IN COMPARISON WITH CLASSICAL TRYPAN-BLUE HEMOCYTOMETER MEASUREMENTS.....	66
5.4.1.	<i>Fed-Batch CHO cultivation</i> .....	66
5.4.2.	<i>Fed-Batch cultivation with temperature shift</i> .....	69
5.4.3.	<i>Fed-Batch Hybridoma cultivation</i> .....	73
5.4.4.	<i>Conclusion</i> .....	74
5.5.	LINEARITY OF FULLSCAN MEASUREMENTS.....	78
5.6.	QUANTIFIED MORPHOLOGICAL CHANGES .....	81
5.6.1.	<i>Heywood circularity factor</i> .....	81
5.6.2.	<i>Morphological changes during production</i> .....	84
5.7.	MORPHOLOGICAL CHANGES BY INDUCED APOPTOSIS.....	88
5.8.	ERROR ESTIMATION OF THE USED ALGORITHMS.....	95
5.8.1.	<i>“out of focus” and “in focus” algorithms</i> .....	95
5.8.2.	<i>“nearly in focus” algorithm</i> .....	96
<b>6.</b>	<b>DISCUSSION</b> .....	<b>99</b>
6.1.	SPEED OF THE IMPLEMENTED AUTOFOCUS .....	99
6.2.	FULLSCANS - BASIS FOR THE DETERMINATION OF AN EXTENDED VIABILITY.....	100

6.3.	COMPARISON OF AUTOMATED CELL COUNTS AND PRODUCT TITER.....	102
6.4.	DIRECT DETECTION OF APOPTOSIS.....	102
6.5.	APPLICATIONS FOR SNAPSCANS.....	103
6.5.1.	<i>Morphological changes under defined conditions</i> .....	103
6.5.2.	<i>Test of stability - Clone selection</i> .....	103
6.6.	SYSTEM ROBUSTNESS AND OVERALL PERFORMANCE.....	104
6.7.	COMPARISON OF THE DEVELOPED SYSTEM WITH COMMERCIALY AVAILABLE VARIANTS.....	105
6.8.	SUGGESTIONS FOR FUTURE WORK – AN OUTLOOK.....	107
6.8.1.	<i>Improvement of the image analysis of fluorescent spots</i> .....	107
6.8.2.	<i>Fast adaption of new staining procedures</i> .....	107
6.8.3.	<i>Multi-color staining with different fluorochromes</i> .....	108
6.8.4.	<i>Scanning of microtiter-plates</i> .....	110
6.8.5.	<i>Binding assays with spherical agarose beads</i> .....	111
<b>7.</b>	<b>LITERATURE.....</b>	<b>112</b>
<b>8.</b>	<b>APPENDIX.....</b>	<b>118</b>
8.1.	SCRIPTS.....	118
8.1.1.	<i>Fullscan &amp; Processing Script</i> .....	118
8.1.2.	<i>SnapScan Script</i> .....	120
8.2.	LABVIEW SOURCE CODE.....	122
8.2.1.	<i>“Out of focus” algorithm</i> .....	122
8.2.2.	<i>Focus Functions - Source code</i> .....	123

## Abbreviations and definitions

<b>“In focus”</b>	Image plane for fluorescence microscopy. Majority of objects (cells)
<b>image plane</b>	gives the sharpest image
<b>“Nearly in focus”</b>	Image plane normally chosen by human observer as sharpest image plane for bright field microscopy
<b>image plane</b>	
<b>“Out of focus”</b>	Image plane outside the normally observed focal image plane during classical bright field microscopy
<b>image plane</b>	
<b>AMS</b>	Automatic microscopy system
<b>ANN</b>	Artificial neural network
<b>Annexin-V-FITC</b>	Fluorescent labeled protein that bound specifically to phosphatidylserines
<b>Bcl-2</b>	Anti-apoptotic protein of the proto-oncogene bcl-2
<b>BHK</b>	Baby hamster kidney cells
<b>CHO</b>	Chinese Hamster Ovary cells
<b>CIP</b>	Cleaning in place
<b>DAPI</b>	4',6-Diamidino-2-Phenylindol
<b>DHFR</b>	Dihydrofolate reductase
<b>DMEM</b>	Dulbecco's modification of Eagle's MEM
<b>dsDNA</b>	Double stranded DNA
<b>FDA</b>	Food and Drug Administration
<b>FullScan</b>	Scan of the complete flow-through chamber in 100 positions at 3 different image planes, totally 300 grayscale images
<b>GFP</b>	Green fluorescent protein
<b>HAM</b>	A Standard Cell Culture medium (Ham, 1982)
<b>huMAb</b>	Human monoclonal Antibody
<b>IMAQ</b>	IMAQ-Vision: Image Processing library of National Instruments
<b>LDAO</b>	N,N-Dimethyldodecylamine-N-oxide
<b>MEM</b>	Minimal essential medium
<b>OCR</b>	Optical character recognition
<b>PBS</b>	Phosphate buffer solution
<b>PI</b>	Propidium iodide
<b>PMMA</b>	Polymethylmethacrylate

<b>RAO</b>	Refractive active objects: Objects in the flow-through chamber that refracts light and focuses the light in an “out of focus” image plane as a bright shining spot. Detection of viable cells which acts as thick lenses and focus the light at best
<b>rDNA</b>	Recombinant DNA
<b>RGB</b>	Red, green, blue
<b>Sf9</b>	Insect cells ( <i>Spodoptera frugiperda</i> )
<b>SnapScan</b>	Time resolved scan of the flow-through chamber at a single position in one to three image planes
<b>Uv</b>	Ultraviolet
<b>Vis</b>	Visible

## Summary

The purpose of this work was to develop an automatic microscopy system (AMS) to monitor the physiological state of mammalian cells during the production of biopharmaceuticals. On the basis of an inverse fluorescent microscope, a device for liquid handling and staining, in combination with two computers for image processing and analysis, a system was developed that can automatically prepare and analyze samples, which come directly from a bioreactor.

With the AMS, it was possible to determine the concentration of viable mammalian cells and their viability. Furthermore, the system is able to classify scanned cell samples based on their morphology and allows an assessment of whether a mammalian cell culture is entering the apoptotic pathway of cell death.

During the course of the project, two different scan methods have been developed. The first scan method, referred to as "FullScan", scans the developed flow-through-chamber in three different image planes at 100 positions. The second method, referred to as "SnapScan", allows a time resolved scanning of the chamber at a single position. While FullScans were used predominately for routine observation of cells during cultivation, SnapScans were used to investigate the changes in cell-morphology and the capability of dye-uptake, as time-lapse studies. Subsequently, video-sequences of long-time studies were generated that allowed observation of dynamic processes lasting for hours in just minutes and which are normally too slow for a manual observation.

Recording and analysis of different image planes at several chamber positions allow the determination of the physiological state of cells considerably better than can be done manually. The analysis of the "out of focus" image-plane of a FullScan, even makes it possible to recognize and count viable cells without any staining. In combination with a fluorescent dye to identify dead cells, a robust, objective, non-tiring and operator independent method has been developed. The results of fed-batch cultivations, examined by the AMS, showed that the system can describe the courses of cultivations far better than it can be done by a human operator using the manual trypan-blue exclusion method. The investigation of different image planes and the possibility to record time-resolved scans eliminates almost all problems of a manual staining method. In contrast to all other methods, the AMS can even differentiate unstained viable cells directly through their refraction behavior which changes with cell shape. Moreover, in combination with a fluorescent dye, the AMS ensures a considerably better detection of dead cells and can also quantify changes in the cell morphology.

The present work allows for the first time the automatic analysis of cell samples by their optical properties in minutes. The system has been used in an industrial environment for the observation of more than 40 batch and fed-batch cultivations, thus emphasizing the robustness of the system. Moreover, the AMS has been constructed as a base-platform for fast adaption of new staining procedures and the developed image processing and analysis algorithms can easily be adjusted to new methods.

## Zusammenfassung

Für die Bestimmung des physiologischen Zustandes von tierischen Zellkulturen die zur Produktion von Biopharmaka verwendet werden, wurde in dieser Arbeit ein System auf der Basis eines inversen Fluoreszenz Mikroskops in Kombination mit einer Färbereinheit entwickelt, welches in der Lage ist die gesamte Probenvorbereitung automatisch durchzuführen (Zellfärbung, Befüllen der Durchflusszelle, Reinigung des Systems).

Das entwickelte Gerät ist in der Lage sowohl die Anzahl lebender Zellen und die Vitalität der Zellen zu bestimmen, als auch die Morphologie der Zellen zu beschreiben, welches eine Abschätzung erlaubt, wann die untersuchten Zellen apoptotisch sterben.

Es wurden in dieser Arbeit insgesamt zwei unterschiedliche Meßprinzipien bzw. Abtastverfahren entwickelt und implementiert. Das erste Verfahren, hier „FullScan“ genannt, dient zur Routineüberwachung der Zellkultur und liefert Bilddaten von 100 verschiedenen Positionen der abgetasteten Durchflußzelle in drei unterschiedlichen Bildebenen. Aus diesen Daten können anschließend sowohl die Zellzahl wie auch die Vitalität und die morphologischen Veränderungen ermittelt werden.

Das zweite Abtastverfahren genannt „SnapScan“ dient dagegen mehr zur Klärung grundsätzlicherer Fragestellungen, wie der Messung des Anfärbeverhaltens einzelner Zellen. Dazu kann eine einzelne Position der Durchflußzelle über ein frei definierbares Zeitintervall in ein bis drei verschiedenen Bildebenen beobachtet werden. Die aufgenommenen Bilder können anschließend zu Video-Sequenzen zusammengesetzt werden, die ein schnelles Betrachten zeitlich langsamer Prozesse, wie das Eindringen eines Farbstoffes in die Zellen, in wenigen Minuten erlauben.

Mit dem hier vorgestellten System ist es nun erstmals möglich, Proben vollautomatisch zu färben und unter dem Mikroskop zu analysieren. Im Gegensatz zu jeder manuellen Beobachtung ist das System Beobachter unabhängig und arbeitet zeitlich konstant. Die Ergebnisse von Untersuchungen in über 40 Fed-Batch und Batch Kultivierungen zeigen, das es mit dem hier entwickelten System möglich ist, den Kulturverlauf während der Kultivierung vollständig zu beschreiben. Die Analyse mehrerer optischer Ebenen liefert deutlich mehr Informationen, die auch in Zweifelsfällen eine richtige Einschätzung des Kulturverlaufes erlaubt, welches mit einer manuellen Färbung wie der Trypan-blau Färbung nicht immer möglich ist. Im Gegensatz zu anderen Methoden ist das in dieser Arbeit entwickelte Gerät in der Lage, ohne Hilfe eines Farbstoffes lebende Zellen durch Messung der Refraktion der

Zellen, welche durch ihre Form und Struktur beeinflusst wird, direkt zu erkennen. Die Verwendung eines Fluoreszenz-Farbstoffes gewährleistet darüber hinaus eine zuverlässige Detektion auch der toten Zellen und zusätzlich können die morphologischen Veränderungen der Zellen quantifiziert werden.

Das System wurde als Basis-Plattform entwickelt und erlaubt z.B. eine schnelle Adaption an neue FärbeprozEDUREN. Die entwickelten Bildverarbeitungsalgorithmen sind parametrisierbar und können so schnell an neue Fragestellungen angepasst werden. Alle gemessenen Daten werden in Datenbanken gespeichert und erlauben so einen schnellen Vergleich einzelner Versuche.

## 1. Introduction

### ***1.1. Production of biopharmaceuticals***

Over the last few decades production of biopharmaceuticals has increased steadily. In particular, more and more therapeutic glycoproteins arise and come to market because the pharmaceutical industry is entering a new phase of designing drugs based on the latest discoveries in genetics. Today, five of the 50 most sold pharmaceuticals worldwide are biopharmaceuticals with sales of 10 billion US\$, ca. 4% of the worldwide pharma-market. In the next three to five years the approval of more than 100 new biopharmaceutical drugs is expected [Werner, 2001]. The market for protein medicines derived from rDNA technology was worth well over US\$ 13 billion in 1999 and is growing at a rate of more than 14% per year. Several established recombinant protein products already command annual sales well in excess of US\$ 1 billion [Grindley, Ogden, 1999].

It seems likely that before small molecules from high-throughput methods or new lead structures from combinatorial chemistry enter the market, that a new generation of genetically designed therapeutic proteins will arise. Many of these new products are complex second generation proteins, which are no longer natural proteins as isolated from different organisms or tissue. The proteins of this second generation are modified in many cases and show improved or new properties. Insulin, for example, can be modified by inversion of the amino acid sequence to be more effective or to exhibit a longer half-life in humans. Other examples are recombinant antibodies with superior immunogenic and pharmacokinetic properties, or a modified interferon- $\beta$  that is more soluble due to the change of cysteine into serine [Bömmel and Duschl, 2001].

Monoclonal antibodies in particular have had a comeback since it is now possible to create fully human antibodies in mice. The HuMAb-Mouse Technology by Medarex for example can now be used to rapidly create new fully human high affinity antibodies. The technology was originally developed by Genpharm International Inc., which was acquired by Medarex in 1997. The HuMAb-Mouse creates fully human antibodies in a matter of months avoiding the need for humanization or for complicated genetic engineering [Medarex, 2001]. Before this technique was established, monoclonal antibodies were expressed as heterologous proteins containing human and human-foreign peptide sequences, which often led to immunological or allergic reactions.

Many of these proteins are manufactured using mammalian cell lines, especially Chinese Hamster Ovary (CHO) cells, hybridoma and insect cells [Werner *et al.*, 1998]. Large-scale production of biopharmaceuticals is carried out by fermentation with mammalian cells in bioreactors. Most production systems are batch, fed-batch or continuous biologically catalyzed reactions in stirred vessels. Fed-batch culture is a frequently used method for the industrial manufacturing of cell culture based recombinant therapeutics [Sauer *et al.*, 2000].

### **1.2. Process control during biopharmaceutical production**

One major drawback in the production of biopharmaceuticals with mammalian cultures is the complex manufacturing process with many unknown or difficult to detect process parameters. Therefore, during commercial production of biopharmaceuticals with mammalian cells only a small number of parameters are logged. Most of these process parameters describe only the environment of a bioreactor and the physical conditions in the fermentation broth, but there is almost no information about the physiological state of the cells itself. Furthermore, there is also a lack in fast analytical methods to determine these complex process parameters on-line to avoid lengthy analytical procedures after the fermentation process has been completed. Within the scope of FDA conform production processes, many parameters related to the product quality are determined, but so far no really established analytical method exists that gives information about the conditions of cells in the reactor during production [Olsson, Schulze and Nielsen, 1998].

In practice, many analytical methods exist to determine the physiological state of cultivated cells. Unfortunately these methods are generally too slow to generate fast data for process control, because most methods are designed for the lab and require manual labour. Over the last decade automated systems have been developed to overcome this problem. A lot of automated sample probes have been developed, but most of these systems were not applicable in an industrial environment because of a lack of stability or durability.

In general, the information available about a production process decreases with increasing scale of the process, often due to a reduced number of measured process parameters. Only simple measurable parameters e.g.  $pO_2$ , pH, temperature, the gas flow rates for  $O_2$ ,  $N_2$ , and  $CO_2$ , and the speed of agitation in stirred reactors are usually observed and recorded continuously for reactors with a volume larger than 1000 liters. Unfortunately to date, no precise predictive models are available for the estimation of such complex processes [Faraday, Hayter and Kirkby, 2001].

### 1.3. Loss of productivity during cultivation

#### 1.3.1. Stability of mammalian cell lines

Monoclonal antibodies produced by the cultivation of hybridomas have become important in both research and therapeutic applications. A major complication in these endeavors is the inherent instability of hybridoma cell lines [Al-Rubeai, Mills and Emery, 1990]. It could be demonstrated that hybridoma cell lines are often mixed populations consisting of both antibody-producing and non-producing hybridoma cells [Kromenaker and Srienc, 1994].

A model based on two differential equations (see below) describes the growth of viable producer and nonproducer cell populations in a mixed cell line. Using this very simple batch-model, flow-cytometric measurements and cell sorting of surface-associated IgG stained cells, the amounts of producer and non-producer hybridoma cells were quantified and the conversation rate of an antibody producing murine hybridoma cell was determined [Kromenaker and Srienc, 1994].

$$\text{producer cells : } \frac{dP}{dt} = m_p P - aP$$

$$\text{non - producer cells : } \frac{dN}{dt} = m_N N + aP$$

P= conc. producer cells, N= conc. Non-producer cells,  $\mu(P,N)$ = specific growth rates (producer, non-producer),  $\alpha$ = rate of conversion of producers to non-producers

Not only hybridoma, also other cell lines, e.g. CHO cells lose their stability during cultivation. Even stable transfected cell lines do so, because of genetic instabilities due to chromosomal rearrangements [Werner, Walz and Konrad, 1992].

#### 1.3.2. Cell Death during cultivation of commercially important cell lines

In the late 1980's the first research groups investigated the cell death of commercially important mammalian cell lines used for the production of biopharmaceuticals [Al-Rubeai, 1990]. The mechanism by which the cells die may be either necrosis, a passive form of cell death due to toxicity, or by apoptosis, in which the cells respond to an inadequate or perturbed environment by undergoing an actively programmed cell death. For a long time, opinions and reports were conflicting about the principal mode of death in mammalian cells during cultivation, especially in CHO cells [Moore *et al.* 1995], [Moore *et al.* 1997], [Singh *et*

*al.* 1994], [Singh *et al.* 1997]. However, the majority of recent publications shows that mammalian cells also CHO cells die almost exclusively via apoptosis [Moore *et al.*, 1995], [Goswami *et al.*, 1999].

Apoptosis is an active and physiological mode of cell death, in which the cell itself designs and executes the program of its own demise and subsequent body disposal. A cell triggered to undergo apoptosis activates a cascade of molecular events, which leads to its total disintegration. [Darzynkiewicz *et al.*, 1997]. Both death modes in direct comparison are shown in Fig. 1-1. The apoptosis cascade starts with the loss of intracellular water, which leads to a condensation of cytoplasm, followed by a change in cell shape and size. The cells shrink while potassium and sodium concentrations dramatically decrease [Bortner and Cidlowski, 1998]. Subsequently, condensation and fragmentation of chromatin occur, followed by cell blebbing. The chromatin collapses down into crescents along the nuclear envelope [Cohen, 1993]. During this process apoptotic cells can undergo membrane breakdown that allows the emergence of a population of “secondary necrotic” cells characterized by apoptotic nuclear morphology and necrotic membranes [Simpson, Miller and Al-Rubeai, 1997]. At the end of the apoptotic process the cells fragment into apoptotic bodies. In contrast to apoptosis, necrosis starts with swelling of the cells which is followed by a rupture of the plasma membrane and release of cytoplasmic constituents, including proteolytic enzymes [Bolt, 2000].

However, cell death does not always manifest classical features of either apoptosis or necrosis. Darzynkiewicz reviewed many examples of cell death in which neither all typical apoptosis nor necrosis features occur. Often features of both cell death modes were described [Darzynkiewicz and Traganos, 1998]. For example, a comparative characterization of cell death between Sf9 insect cells and hybridoma cells showed that Sf9 cells died by atypical apoptosis in absence of nuclear fragmentation, scarce association of condensed chromatin to the nuclear envelope and nonspecific DNA degradation without building a typical DNA ladder [Meneses-Acosta *et al.*, 2001].

The different measurement principles to detect apoptosis have been reviewed in numerous publications [Sgonc and Wick, 1994], [Belloc *et al.*, 1994], [Dive, Darzynkiewicz and Ormerod, 1995], [Darzynkiewicz *et al.*, 1997], [Bedner *et al.*, 1997], [Martelli *et al.*, 1999], [Weber *et al.*, 1997]. Besides very complex detection protocols, the DNA dye DAPI was found to be one of the earliest staining methods for the detection of apoptotic cell death and hence, was used also here in the present work. [van Adrichem, 1997].

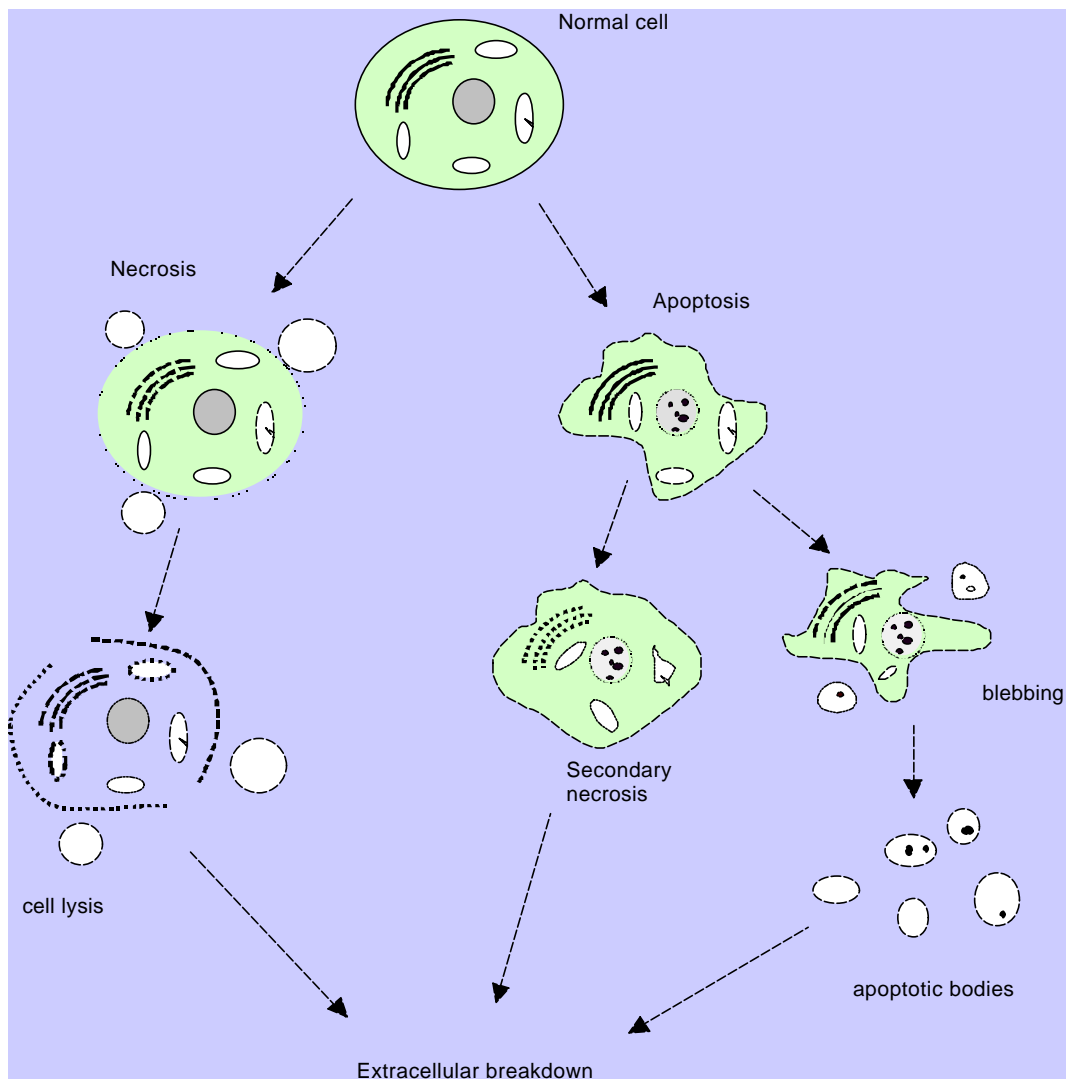


**Fig. 1-1 Scheme illustrating morphological and biochemical changes during apoptosis and necrosis [based on Al-Rubeai, 1996 and Darzynkiewicz *et al.*, 1997]**

#### **1.4. Process Optimization Strategies**

Optimization of biopharmaceutical processes using mammalian cell culture may lead to two areas of interest:

1. Higher reproducibility of cultivation due to improved measurement and control of the process
2. Increase in productivity (yield)

Reproducibility can be increased by the use of better or new equipment, e.g. improved measurement and reliable, highly sophisticated process control systems [Konstantinov, Aarts and Yoshida, 1993], [Schügerl, 2001]. Improvement of productivity in terms of fed-batch

cultivation, which is the most common production mode for manufacturing biopharmaceuticals with mammalian cell culture, equals maximizing the final product concentration. Mathematically speaking, the final product concentration equals the product of the specific production rate and the integral of the viable cell concentration versus time [Sauer *et al.*, 2000], see Eq. 1.

$$P = \beta \int x_v dt$$

**Eq. 1** P = product concentration,  $\beta$  = specific productivity,  $x_v$  = viable cell conc.

Two strategies can be applied to improve productivity: Firstly, by modification of the process itself, i.e. changing the process mode or using improved feeding strategies [Dhir *et al.*, 2000]. Secondly, by genetic engineering of the used cell line [Singh *et al.* 1997].

#### 1.4.1. Genetic engineering of production cell lines

Apart from the improvement of the expression-system to increase the protein production several attempts have been made to prolong the lifetime of a production cell line. Towards the end of a fed-batch cultivation almost all cells enter the apoptotic pathway, i.e. the culture has reached the point of no return and all cells will definitely die. To prevent cells from entering the apoptotic pathway the bcl-2 family proteins that serve as critical regulators of pathways involved in apoptosis were used for genetic engineering approaches [Reed, 1998]. It has been shown that over-expression of bcl or bcl-xL was able to abrogate cell death in BHK and CHO cells after glucose deprivation or serum withdrawal [Mastrangelo *et al.*, 2000] [Tey *et al.*, 1999].

#### 1.4.2. Feeding Strategies

Fed-batch culture offers various advantages over other culture operations such as batch, perfusion, and continuous [Xie and Wang, 1994]. It is easy to implement and allows a high product concentration as well as high product yield in the medium [Patel *et al.*, 2000]. However, its performance strongly depends upon the effectiveness of the feeding strategy. The nutrients fed in general are glucose, amino acids, and other essential nutrients such as insulin, cholesterol and vitamins. Phosphate and other salts are often excluded in order to avoid increased osmolarity in the culture [Zanghi *et al.*, 1999].

Several features of cultivation processes have not yet been fully understood. For example, the duration of CHO cultures can be increased 2-3-fold by adding back serum that has been

shown to contain unidentified survival factors in serum that can greatly reduce apoptosis in protein competent cell lines in all phases of the culture [Zanghi, Fussenegger and Bailey, 1999].

Although many cultivation processes have not been fully understood, improved feeding strategies make it possible to increase the final product concentration significantly. For example, Zhou *et al.* reached a final product concentration of 2.7 g/l in 672h by using an amplified NSO myeloma cell line and a feeding strategy based on daily feedings. The feeding strategy was based on the projected integral of viable cell concentration over time and assumed constant specific nutrient consumption rates or yields to maintain concentrations of the key nutrient components around their initial level [Zhou *et al.*, 1997].

### **1.5. Microscopy, image processing and analysis in biotechnology**

Since the 1980's researchers have been dreaming of a fully automatic system that can be used to observe specimens by microscopy coupled with a computer that understands what the system has seen [Walter and Berns, 1981]. Although, during the last decade, when more powerful and cheaper computer equipment became available and many improvements were made, this dream could still not be realized and we are nowadays still far away from a realization of an artificial intelligent system that can replace a human observer [Sabri *et al.*, 1997]. The complexity of human perception is enormous and understanding is still in its infancy, thus, automatic image processing and analysis systems can solve only very simple tasks. The next chapter will show in two simple examples that point out two major differences between human seeing and image processing and analysis based on the use of classical morphometric methods.

#### **1.5.1. Comparison of human and artificial perception**

The associative capabilities of human vision in comparison with artificial systems can be shown in two simple examples. In contrast to any artificial system, a human being is instantaneously able to read the word in Fig. 1-2. However, no common OCR (optical character recognition) software would resolve this kind of character set unless the software were especially adapted for this type of character. Untrained OCR software that identifies characters by recognizing crossing junctions is normally not able to complement the missing parts and fights a losing battle.

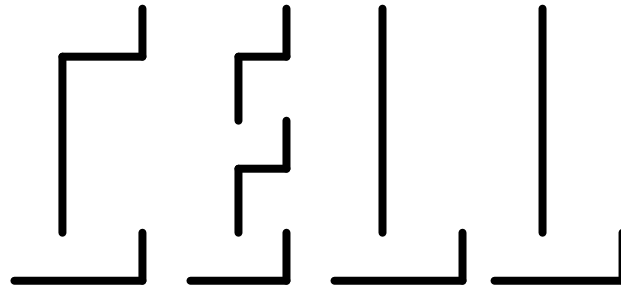


**Fig. 1-2 associative perception**

The capability to compensate missing image structures is one of the major advantages of human perception. Although the example in Fig. 1-2 shows only the shadows of the word “CELL” a human viewer can normally complement the missing information at once.

The second example (Fig. 1-3) demonstrates the relatively weak developed capability of human perception to quantify more than a few objects in an image. In contrast to a computer that needs only a few milliseconds to count the black objects in Fig. 1-3, a human viewer needs normally much more time to find out the correct number because he must count object by object.

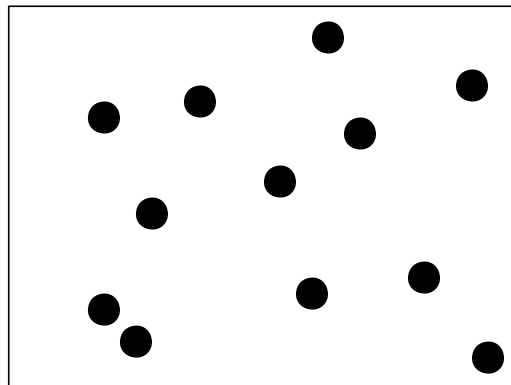


**Fig. 1-3 Test of counting objects**

Both examples show that human perception has many advantages in regard of analyzing complex images and textures. The capability to isolate objects from a complex background or to complete missing image information is unrivaled. But there are also some disadvantages. The ability to quantify similar objects very fast is not very well developed in humans. Probably, it was not an important advantage for a human being in the past to discern whether he was being attacking by six or nine lions. Hence, counting more than five objects at once has not been an evolutive selection advantage for humans – it was sufficient to know that there were many lions coming.

Thus, computer aided rapid counting of objects can help to compensate human shortcomings and moreover release us from tedious work. An overview of recently developed applications of image processing and analysis will be shown in the next chapter.

### 1.5.2. Application of image processing and image analysis in bioscience

For many years microscopists have counted or measured their specimens manually. Recently image processing and image analysis has become an invaluable accessory for such quantification because it reduces subjectivity and allows automation. Since the 1970's, commercial image analysis instruments have been available for bacterial colony counting [Thomas and Paul, 1996]. During the last five to six years the development of image processing and analysis systems has rapidly grown, forced by the fast development of computer hardware [Wilkinson, 1995]. Thus, here a short review is given of some interesting applications of image processing and analysis in the field of bioscience of the last few years.

Already 1994 Maruhashi *et al.* presented a system for automated measurement of cell concentration and viability of suspended animal cells. Based on a microscope, a flow-through chamber and an image processing and analysis computer, the system scanned the chamber and analyzed the resulting images by computer. A simple algorithm determined cells on their different brightness distribution and on the basis of these results calculated the viability [Maruhashi, Murakami and Baba, 1994].

Zhang *et al.* presented 1995 a machine vision sensor and a neural network-based supervisory control system for microbial cultivation. The vision sensor was capable of counting the number of microbial cells and acquiring other information like sporulation activity from the sample medium. The neuronal net, which was previously trained with 18 historical process data sets, was then used to optimize the set points for pH and temperature to optimize the course of the cultivation [Zhang *et al.*, 1995].

Kravtov and Fabian suggested that changes in morphology of cells undergoing apoptosis might cause characteristic changes in their optical properties. They presented a simple assay based on the observation of the changes of the optical density (OD) at 600nm, which allowed the observation of the influence of different chemotherapeutics. They found that there exist different characteristic patterns of changes of the OD during the time, which allows to distinguish between apoptotic and necrosis death of cells [Kravtov and Fabian, 1996].

Zalewski and Buchholz presented a fully automated sampling and analyzing system for the morphological investigation of yeast cells. The algorithm developed in this work was able to subdivide yeast into four different classes (single cells, double cells, tetrads and clusters with or without further sub-objects, i.e. vacuoles) on the basis of edge detection and closing of object structures. For that purpose, an algorithm was developed that seeks for yeast typical gray-value profiles in the image and marks them as object edges. Besides the determination of the growth of yeasts it was also possible to detect the degree of vacuolization and to determine different growth phases by classification of the morphology of yeasts for the first time [Zalewski, 1995], [Zalewski and Buchholz, 1996].

In 1997 Weisser *et al.* investigated the feasibility of a method to quantify apoptosis and lytic cell death by using video microscopy in combination with artificial neural networks (ANN). From a group of 20 morphometric features describing a stained nucleus they found eight features that discriminate apoptotic and necrotic nuclei from normal nuclei. Thus, an ANN was trained with a set of 90 different nuclei based on these three classes. After training the ANN, apoptosis induced cells were stained with the DNA dye Hoechst 33342 and 30 min later the nuclei of the stained cells were observed under the microscope. Images were taken and the nuclei were isolated from the images by using an algorithm based on dilation and erosion. After morphometric analysis, it could be shown that the trained ANN was able to identify most of the apoptotic nuclei correctly and that the ANN could better determine necrotic nuclei than a human investigator. Also Weisser *et al.* found that apoptotic nuclei were significant brighter than normal nuclei and also the variance of the gray values were greater [Weisser *et al.*, 1997].

Bittner, Wehnert and Scheper presented an in-situ sensor in 1998 that allows on-line microscopic observations of *Saccharomyces cerevisiae* during cultivation direct inside a bioreactor. The compact sensor consists of two CCD video cameras. With them the sensor is able to observe specimens in two different image planes without any mechanical focusing. To separate objects from the background, the system takes advantage of the optical properties of the yeasts that behaves as convex lenses and focus entering light as bright spots in one of the observed images planes.

In the same year, Wit and Busscher presented a fed-forward ANN that directly investigated 9x9 microscopic sub-images to count yeasts and bacteria adhering to solid substrata. Here, no prior image processing algorithm, which extracts several morphometric parameters was needed. On the contrary the original image was subdivided into small 9x9 images that were directly fed into the neural network. The ANN calculates the likelihood for the central pixel in

the 9x9 sub-image of being the center of an adhering microorganism [Wit and Busscher, 1998].

To evaluate aggressiveness of in vitro cell lines the motility of aggregated cells was measured because changes in adhesiveness and motility are of considerable importance in tumor regression and are major features to determine metastatic potential. Among other things, De Hauwer *et al.* developed a tracking algorithm on the basis of the watershed transformation to segment different cells from each other. To prevent over-segmentation a marker method was used so that only marked objects separated by building of basins appearing at a local minimum of brightness. At the end of segmentation all relevant object boundaries are part of the basin contours (for further details of the watershed algorithm see [Soille, 1998] and [Wegner *et al.*, 1997]). With the developed methods and algorithms de Hauwer *et al.* could show that with the help of image processing it was possible to realize a cell tracking system and to characterize the motility of every cell in a given cluster [de Hauwer *et al.*, 1999].

In 1999, Pläsier *et al.* compared a newly developed automatic image analysis assay for detecting of apoptotic animal cells based on dual staining with annexin-V and propidium iodide (PI) with data generated by flow cytometry and manual scoring. For the image analysis assay two different fluorescent dyes, PI and annexin-V-FITC, were used because both emit light at two different wavelengths and can be detected with a 3CCD color camera on separate color channels. Both fluorescent dyes were chosen because annexin-V binds specifically to phosphatidylserine that are exposed on the outer cell membrane of apoptotic cells and propidium iodide was used as a membrane impermeable counterstain to detect necrotic cells. Altogether the system took three images, one under bright field and two under fluorescent light, each at different color channels (red and green) of the camera. The bright field image serves as the basis for detection of the total cell number and both images taken under fluorescent light are analyzed to detect apoptotic and necrotic cells. Pläsier *et al.* concluded that all three methods were found to correspond well but there is no “perfect” correspondence between any of the three methods. However, similar trends were shown by the three methods and there was no overall tendency at all for one method to be high or low compared with the other two. Thus, Pläsier *et al.* found image analysis is a valid alternative method to manual microscopy or flow cytometry for measuring viability and apoptosis in animal cell cultures using annexin-V. Because the used sample preparation protocols involve several washing and centrifugation steps and cells could be easily lost all three were measured only as a percentage of the total [Pläsier *et al.*, 1999].

---

What could be possible in the future has been demonstrated by Lütkemeyer *et al.* who showed a combination of a cell imaging system and a robot automation. They coupled a developed sample device based on a 7-axes robot arm with a commercially available cell imaging system that does the trypan-blue exclusion method automatically. Their work shows the first steps on the way to a fully automated pilot plant where one of the most frequent infection source, a human operator, is replaced by a complete automatic environment.

Kino-oka *et al.*, presented a monitoring system for the observation of the production of keratinocytes for skin transplantation, using skin grafts of cultured keratinocytes in form of multilayer differentiated cell sheets for burn wounds and chronic leg ulcers. In this connection an on-line growth monitoring by measuring the degree of confluence of keratinocytes in t-flasks and Petri dishes based on image analysis was developed. The growth rate of keratinocytes was calculated subsequently from the linear relationship between average degree of confluence and cell concentration [Kino-oka and Prenosil, 2000].

The publications reviewed here should give a short overview about different developments in the field of image processing and analysis in biotechnology. As mentioned above, the number of image processing applications in all technical fields is increasing, also in biotechnology just seen by the here reviewed works. But just the observation of cells via a microscope and the subsequent analysis of these images is one of the particularly difficult areas because of the often very weak contrast of the images, especially when unstained cells are investigated by bright field microscopy. Although most image processing applications presented here were very promising with regard to industrial use only one has been recently commercially established. At the beginning, most image processing applications are deficient because of lack in resolution of the images, very simple algorithms and the low speed of available computer systems. The use of supervised artificial neural networks require large training sets, but especially cell culture processes lack in reproducibility and due to the cultivation length often only too few data sets for training a ANN are available. Simple OD measurements are often not reliable enough and are often affected by unknown media components or by changes of the media composition during cultivation. The development and use of complex image processing and analysis algorithms mostly requires an appropriate complex parameter set for tuning the algorithm. Very often the chosen parameter does not fit for all images that have to be analyzed by the algorithm and a manual tuning is required.

## 2. Aims of the work

The aim of the work was to develop an analytical device that can observe suspension cell cultures and give additionally information about the state of a cell culture. The system should be able to replace routinely manual counting of cells with a hemocytometer as well as the ordinary used trypan-blue exclusion method to determine the number of viable cells. System and software should be developed as a base-platform that allows fast implementation of new procedures without the need of complex programming. Additionally, the system should be able to do all liquid-handling automatically including the capability of staining cells and cleaning the system after a measurement have been done. The system should be user-friendly with an easy user interface that allows also untrained staff to use the system.

Moreover, the system should handle the complete sample management and offer a simple graphical visualization that allows assessment of the results of the investigated samples.

Further, it should be possible to use the developed system as on-line application later, with a direct connection to a bioreactor. Thus, the possibility to extend the system, so that it can be used on-line, should be implemented from the start of the development.

Also an interface should be included in the software that allows a communication between the analytical device and a process control system.

After development, the multiparametric analysis system should be used during the routine observation of mammalian cell cultivations in the biopharmaceutical industry to test the reliability and robustness of the system in an industrial environment and in comparison with the manual trypan blue exclusion method. An overview of the concept with all components and the major applications is shown in Fig. 2-1.

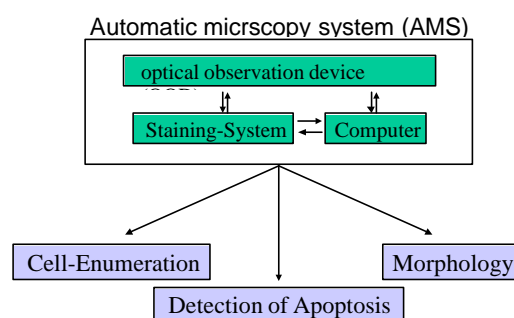


**Fig. 2-1 Concept of the automatic microscopy system (AMS)**

### 3. Materials

A major part of this thesis was the development of an analytical device for observing cells optically using an automated microscope and to build a system, which can do all needed liquid handling automatically. The current chapter contains all details about the construction and the actual state of the developed system. All developed programs and image processing algorithms necessary for the operation of the system will be described in the next chapter 4 (Methods). Experiments important for the development of the system and highlighting the potential of the developed system will be shown in chapter 5 (Results).

#### ***3.1. Newly developed or modified devices***

The developed system basically consists of three components: an inverse microscope, a liquid handling system and a computer for controlling the entire system. A flow-through chamber was developed to enable automatic sample transport to the microscope and automatic observation of the sample. A detailed view of all parts can be seen in Fig. 3-1, a diagram of the developed system is given in Fig. 3-2.

##### 3.1.1. Microscope

In all experiments performed a modified inverse microscope type Axiovert S 100 (Zeiss, Oberkochen, Germany) with an ACHROPLAN 20x objective (0,4/PH2) was used. The microscope was equipped with a Zeiss condenser type 0.55, a green-filter, and an HBO-50 arc lamp as uv-light source. As fluorescent filter the Zeiss standard filter set type 02 was used with a beamsplitter at 395 nm. The microscope was extended with a x,y-stage (Merzhäuser, Wetzlar, Germany), a motorized z-axis drive and an uv-light shutter-system for opening and closing the uv-light-path automatically. All these components were connected to a microprocessor driven control-unit (MCU-26, Zeiss) that allows manual control of the stage and the z-axis as well as remote control by a computer-system via the RS-232 serial-interface. Additionally, the vis-light source power supply was modified to enable the connected computer to switch the vis-light source on and off automatically.

##### 3.1.2. Liquid Handling and Staining System

A system was developed based on two automatic syringes and three multi-channel valves (all components from Hamilton AG, Bonaduz, Switzerland) controlling liquid handling as well as for the staining of the samples. This system will be referred to as the "staining system" from now on. All devices of the system could be controlled via a serial RS-232 connection.

Syringe S1 (volume 2,5 mL) is responsible for all liquid transport processes like filling the mixing chamber, loading the flow-chamber with cells and cleaning the entire system. Valve

V3 controls the distribution of all liquid flows to the connected devices. Syringe S2 (1 mL) serves as a reservoir for the fluorescent stain employed. Via Valve V1, a sample can be loaded directly into syringe S1 and valve V2 connects the syringe S2 to the external dye reservoir or to new fresh dye solution. Valve V2 also allows fading in a defined volume of dye solution in the liquid sample-stream which is transported into the mixing chamber. This set-up allows the system to introduce a very small amount of dye solution into a larger sample stream. In addition it guarantees good intermixing because the dye is faded in the liquid stream first and is then rinsed with the following sample.



**Fig. 3-1 The experimental prototype: Left, staining-system with syringes and valves. In front of the staining system the mixing-chamber. Middle: Fluorescent Microscope with video camera and mounted flow-through-chamber. Right: MCU 26 control unit.**

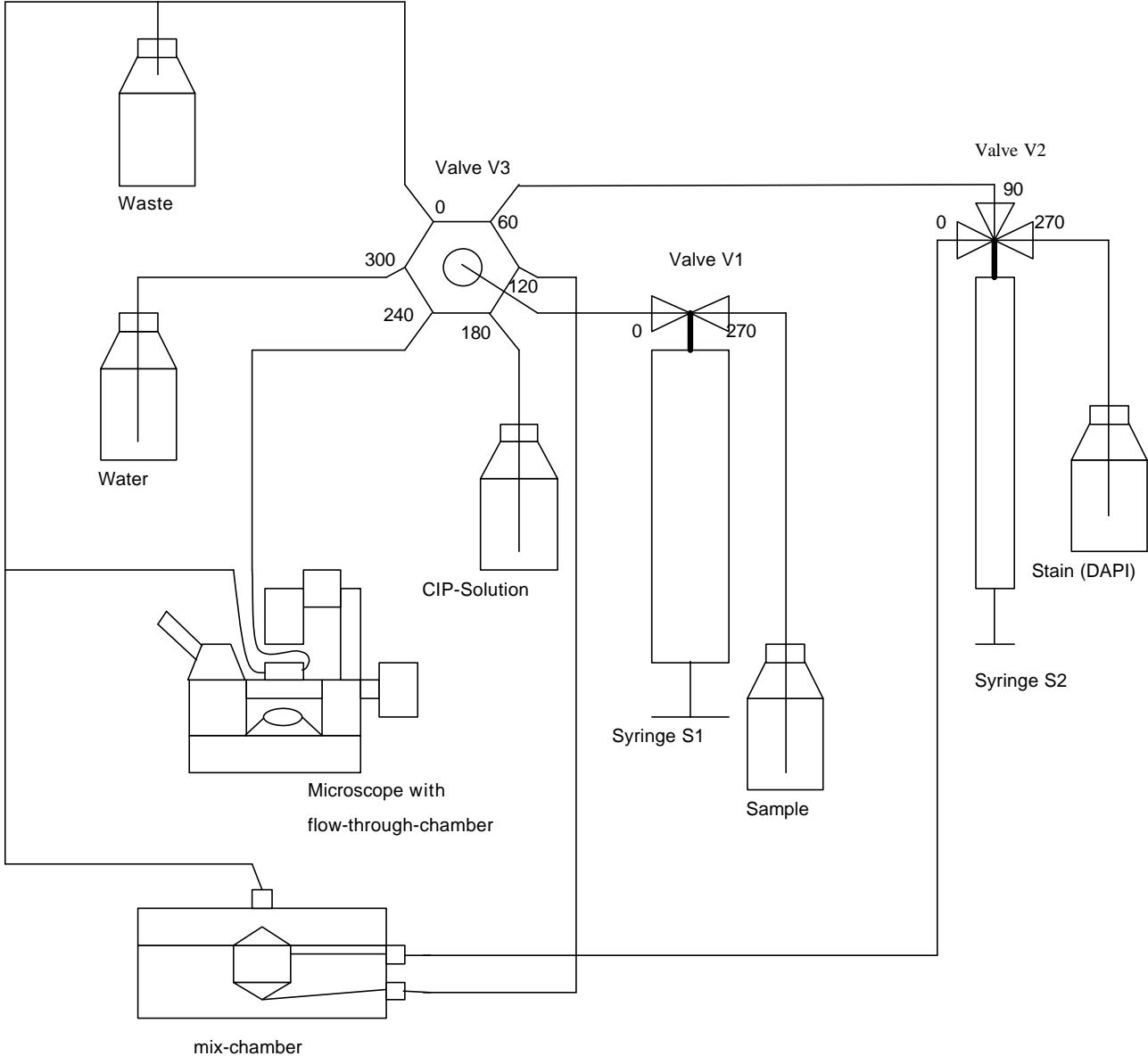


**Fig. 3-2 Entire automatic microscopy system with inverse microscope, flow-through-chamber, mixing chamber and all valves and syringes for liquid handling and staining**

### 3.1.3. Flow-Through-Chamber

The flow-through-chamber is based on a standard glass-slide as chamber bottom and is designed for discontinuous operation mode. This means, the chamber is loaded with a sample followed by a sedimentation phase. During this sedimentation phase the cells settle on the chamber bottom with the advantage that all cells are then lying in a single focal plane.

The flow-through-chamber consists of a PMMA block and is mounted with six screws on a metal base-plate. As plate format the dimensions of a standard microtiter plate (9x13 cm) were used to ensure that the base-plate fits correctly into the stage rack. PMMA was chosen because of its good optical properties and its better resistance against mechanical stress than glass. In- and outlet of the chamber were arranged at an angle of 45° to reduce shear stress in the bends of the chamber connectors.

Fig. 3-3 shows the chamber mounted on the stage and connected to the staining system via Teflon tubes. A defined volume was needed for quantification. Therefore, a rhombic area was milled out of the chamber top with a depth of 200 µm. A standard microscope glass slide (76x26x1 mm, Menzel-Gläser, Germany) sealed with an o-ring gasket was screwed onto the base-plate to generate a constant measurement volume. The set-up using a standard glass slide has the advantage that the optical path of the microscope remains almost unchanged. The detailed design of the flow-through-chamber can be seen in Fig. 3-4 and an assembly scheme is shown in Fig. 3-5.

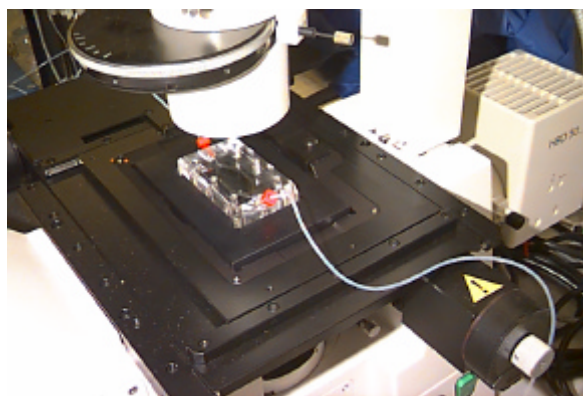


**Fig. 3-3 Flow-through-chamber mounted on the microscope stage**

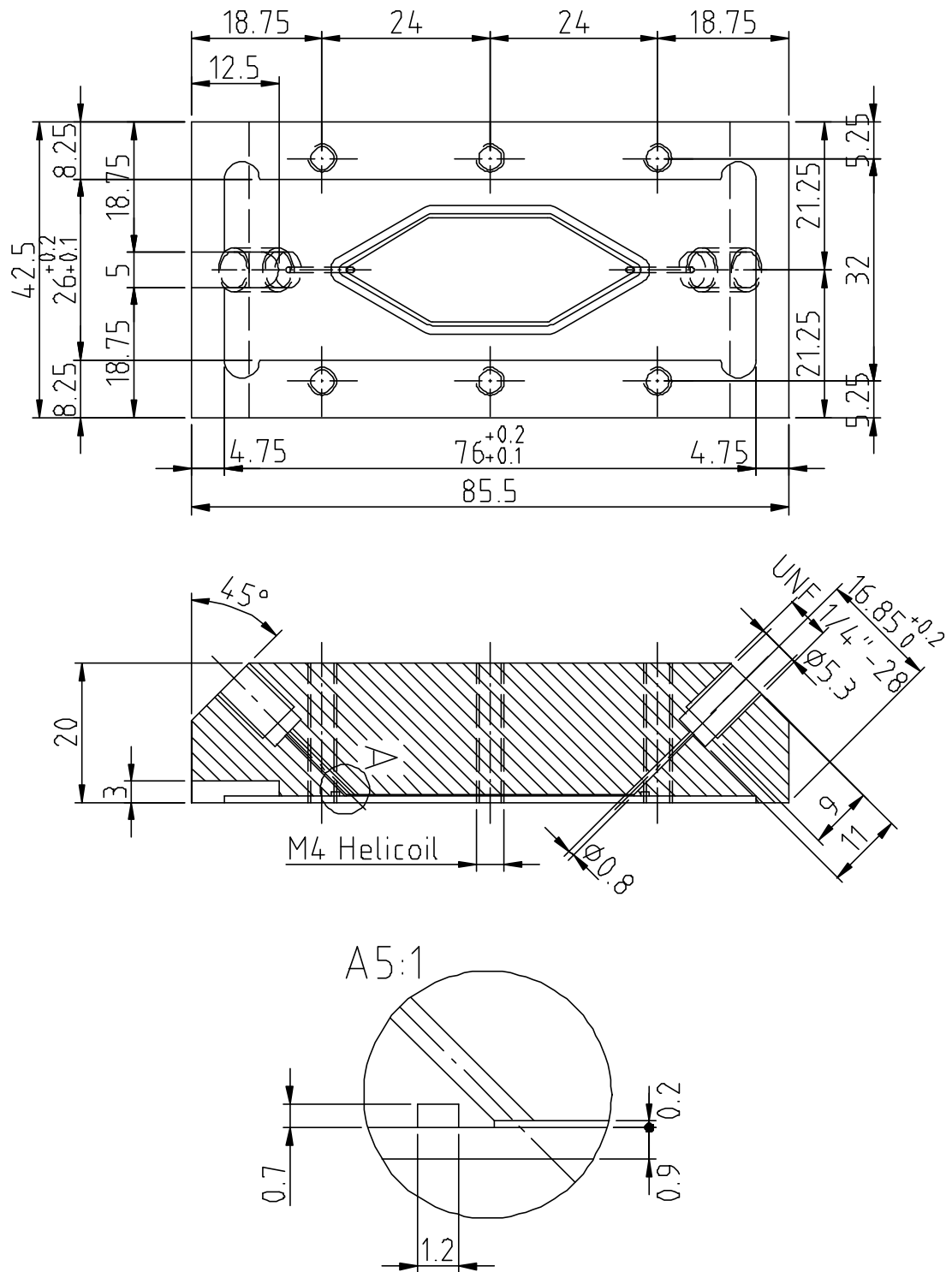
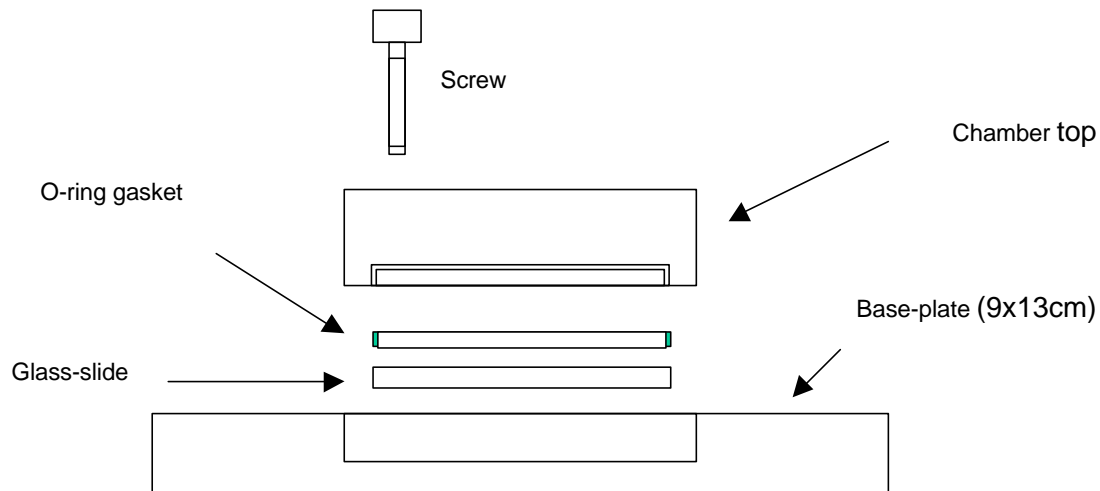


Fig. 3-4 Design of the flow-through-chamber



**Fig. 3-5 Assembly of the flow-through chamber**

#### 3.1.4. Mixing-Chamber

The mixing chamber is mainly designed for simply mixing the sample with the dye to be used. The chamber consists of a cylindrical mixing volume of ca. 2 ml with two in/outlets on the left side and a waste outlet on the top. The chamber top is held together with the chamber bottom by six screws. Top and bottom are sealed with a flat gasket. A small magnetic stirrer is added to improve the mixing (Fig. 3-6).

The design of the chamber allows the insertion of a flat filter membrane between top and bottom to perform simple washing procedures of the cell suspension, but this feature has not been tested yet.

One of the lateral in/outlets is asymmetrically arranged generating a vortex when the chamber is being filled. Originally, this feature was developed to clean the inserted membrane from cells and debris to prevent filter clogging but it has been found that the vortex is useful for cleaning the entire mixing chamber. The second in/outlet is arranged symmetrically on the bottom of the chamber to ensure a complete removal of all liquid (Fig.3-7). The entire mixing chamber is constructed as an open system and, therefore, it is important that the chamber is aerated via the waste tube to prevent vacuum formation inside the chamber when the chamber is emptied. If the waste tube was submerged in wastewater it would be sucked in.

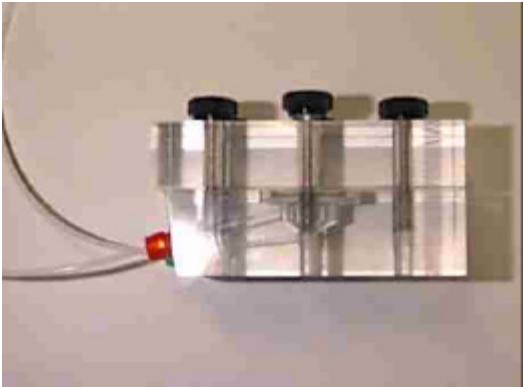
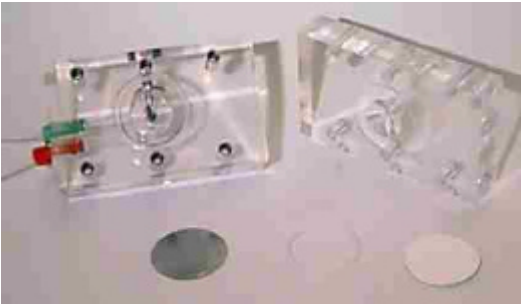


Fig. 3-6 Mixing chamber with membrane filter insert (left) and assembled

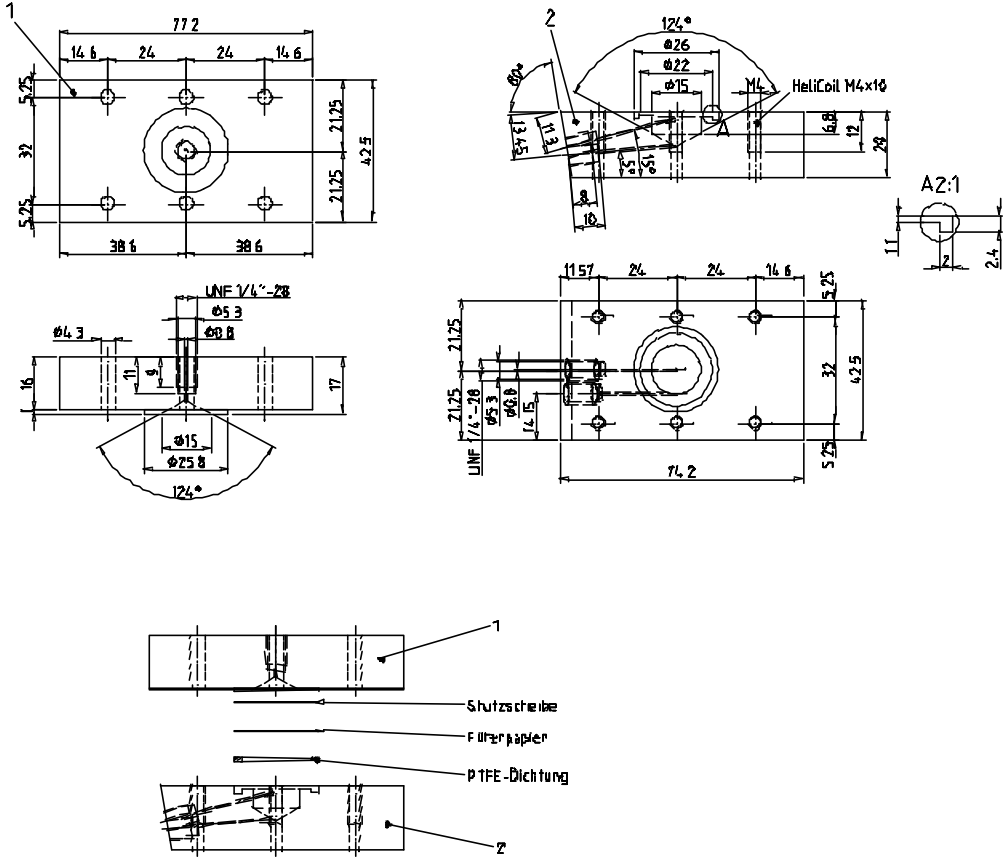


Fig.3-7 Construction plan of the mixing chamber

### 3.2. Standard Materials

#### 3.2.1. Computer

A dual pentium II computer (2x400Mhz) was used for controlling the microscope via a Zeiss control unit MCU26 and for controlling the staining system. The dual pentium II processor system was also used for the image processing of two focal planes when the system was scanning the flow-through chamber in the FullScan mode. During the image processing the system usage was split between the two processors. While one processor carried out all processing tasks, the other one controlled the microscope and the staining system.

A second computer (pentium III, 500Mhz) was employed for all further image processing steps. Using two separate computers allows a better separation of data acquisition and image processing which needs a lot of computational power. Freeing the second computer from all additional hardware control tasks, leads to maximum speed of all needed image-processing steps. While the second computer carries out the image processing, the other one can already prepare the system for a new sample.

Tasks	Type
<b>Control</b> <ul style="list-style-type: none"> <li>• Microscope</li> <li>• Staining system</li> </ul>	Pentium II Dual Processor (2x, 400 Mhz) 256 MB Memory 2x 4GB SCSI Harddisks
<b>Image Processing and Analysis</b> <ul style="list-style-type: none"> <li>• Cell Counting</li> <li>• Viability Determination</li> </ul>	Framegrabber
<b>Morphological Analysis</b>	Pentium III, (500 Mhz) 256 MB Memory 12 GB DIE-Hardisk

#### 3.2.2. CCD Camera and Framegrabber

For image acquisition a liquid cooled 256 gray-scale video camera (Camera: CF8/1 FMCC; Cooler and Power Supply MCC; Kappa, Gleichen, Germany) was used with an effective resolution of 752x576 pixel. The video signal of the camera was digitalized by a framegrabber (IMAQ PCI-1408, National Instruments, Austin, USA).

#### 3.2.3. Fluorescent Dye 4',6-diamidino-2-phenylindole (DAPI)

For all staining procedures the fluorescent dye 4',6-diamidino-2-phenylindole (DAPI) was used. The excitation maximum for DAPI bound to dsDNA is 358 nm, and the emission

maximum is 461 nm. DAPI can be excited with a xenon or mercury-arc lamp or with the UV lines of an argon-ion UV laser. Binding of DAPI to dsDNA produces a ~20-fold fluorescence enhancement, due to the displacement of water molecules from both DAPI and the minor groove.

As stock solution, 1 mg DAPI was dissolved in 1 ml pure water. The stock solution was spilt into 20 µl aliquots, which can be stored at 4°C for several months. As working solution, 20 µl was diluted with 980 µl PBS buffer. One milliliter of the working solution was directly loaded into syringe S2 of the staining system that served as a reservoir. Each diluted aliquot was sufficient for ten measurements

#### 3.2.4. Microspheres for Autofocus Calibration

For the calibration of the chamber and for all autofocus experiments with fluorescent polystyrene microspheres, FluoSpheres F-8837 from Molecular Probes (Oregon, USA) with a diameter of 15µm were used.

#### 3.2.5. Cell Cultivation

All cell cultivations were carried out as batch or fed-batch processes in industrial bioreactors on a scale ranging from 10 to 300 l reactor volume. All bioreactors were equipped with standard temp, pH, and pO<sub>2</sub> control devices. If not stated otherwise Rushton-type or pitched blade impellers were used as stirrer.

#### 3.2.6. Media

For production, optimized cultivation media on the basis of Ham F12 and DMEM supplemented with lipids and vitamins were used for all cultivations.

#### 3.2.7. Analytics

The In-Process Control Laboratory of the Novartis Pharma AG, Switzerland carried out the quantification of product titer, lactate and glucose. The product titer was quantified by either size-exclusion chromatography or in cases of antibodies by protein A affinity chromatography. Glucose and lactate were analyzed by cation-exchange chromatography using a Nucleogel Ion 300 OA column.

#### 3.2.8. CIP-Solution

For all Cleaning Procedures a CIP solution, containing sodium hydroxide and a detergent (Lauryldimethylamine-N-oxide = LDAO) was used to remove cell debris from the system.

---

0.25 % LDAO N,N-Dimethyldodecylamine-N-oxide Fluka Biochemika 40234

0.75 M NaCl

0.25 M NaOH

### 3.2.9. Hemocytometer – Trypan blue dye-exclusion method

All hemocytometer counting was performed with an “improved-neubauer” chamber. Viability was measured using the well-known trypan blue dye-exclusion method.

### 3.2.10. Induction of Apoptosis - Actinomycin D

All apoptosis induction experiments were induced with Actinomycin in a concentration of 2  $\mu\text{g}$  Actinomycin D per  $1 \times 10^6$  cells.

## 4. Methods

### 4.1. Software Concept

From the very beginning of the project an important objective was the creation of a user-friendly interface to make it also possible for non-experts to use the developed system. Therefore, Labview® from National Instruments was chosen as programming language, because Labview allows a very fast design of graphical user interfaces. Labview contains a graphical library with all elements for a complex front panel design, allows direct hardware access even under Windows NT 4.0 and is still a compiler language fast enough to cope with heavy computation problems like image processing and analysis. To solve the image processing problems and to realize the image analysis Labview was extended with the IMAQ-Vision library also from National Instruments. The database access was realized by using the SQL Toolbox, which is additionally available as an extension for Labview. All programs were written using the Labview versions 5.1 or 6.0.

The complete software concept is shown in Fig. 4-1. An independent program called “*OLM V.167*” was written for controlling the microscope and the liquid-handling. Integrated in this program was a script interpreter that can trigger all operations, which are needed to manage a full-automated system. During the developmental phase, numerous scripts were programmed to perform the following operations:

- Cleaning of individual parts or the entire system
- Calibrating the microscope stage and the z-axis (zero positioning)
- Starting different scan modes like FullScans, or SnapScans.

In addition, the *OLM V.167* program carries out also a part of the image processing. After a FullScan has been taken the program calculates the number of viable cells and counts the fluorescent events by analyzing two image planes, the refraction image plane and the fluorescence image plane of the FullScan.

As mentioned earlier, the image processing was divided into two steps. A basic image processing step in which the refraction and the fluorescence images were analyzed to generate the viable cell counts and the viability and a more advanced image processing step which was executed by a second computer. During the advanced image processing the bright field image plane of a FullScan is analyzed and the developed algorithms extract morphological data, which are stored in a database (see Fig. 4-1). To handle the large

---

amount of different data a database concept was developed based on three Microsoft Access databases also shown in Fig. 4-1. After a "FullScan" was taken and the basic image processing which follows was executed, a database called "FullScans" administered all data generated by the automated microscope system and the OLM V.167 software. These data contain the determined viable cell concentration, the viability, the destination directory of the saved images of the FullScan, and some additional information about the sample, which can be manually added by the operator. The second database contains all morphological data extracted from the bright field images analyzed by the second computer. The data in both databases are automatically linked together by the system. The third database contains all additional information of the observed processes such as manually counted cell densities, product titer concentrations and additional off-line analyzes e.g. nutrients and metabolites.

The results of the automatic cell counts and the viability can be directly compared with the off-line measured values in the database environment itself using the integrated graphical visualization tools of Microsoft Access. For the representation of the all-morphological data a separate program was developed, which can access all databases by the SQL tools of Labview and uses the visualization facilities of the Labview programming language.

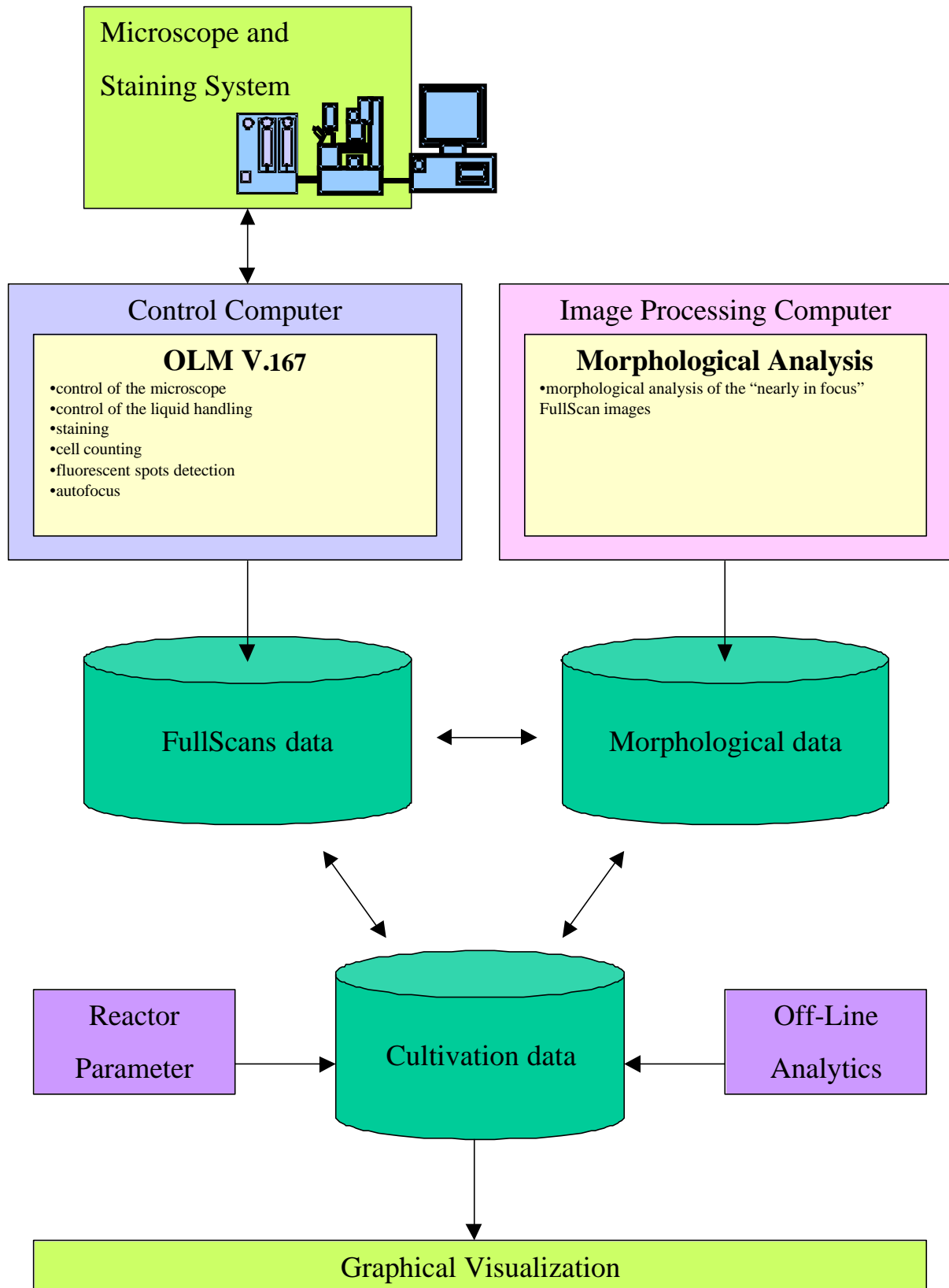


Fig. 4-1 Software concept



	Sends a command string to MCU-26 Microscope Control Unit (for detailed Information, see MCU26- Programming Manual)
<b>Mcu_read</b>	<i>mcu_read [mcu command string]</i> Reads information from the MCU-26 Microscope Control Unit and displays the information in the actual status-line of the status-monitor (for detailed information, see MCU26- Programming Manual)
<b>Zerpos</b>	<i>Zerpos</i> Zero positioning of microscope stage and z-axis
<b>Scanning Commands</b>	
Commands	Syntax/Description
<b>Fullscan</b>	<i>Fullscan</i> Starts FullScan procedure
<b>Fullscan_fl</b>	<i>fullscan_fl</i> Starts FullScan procedure (fluorescent plane only)
<b>Snapscan</b>	<i>snapscan time,cycles</i> Command generates SnapScans in combination with the command <i>select_pos</i>
<b>Select_pos</b>	<i>select_pos</i> Command starts a viewer modus and pop up a dialog box to select a sample position
<b>Snap_st_abs</b>	<i>snap_st_abs x-pos, y-pos, z-pos, time, cycles</i> Starts a SnapScan in a predefined position
<b>Other Commands</b>	
<b>Processing</b>	<i>Processing</i> Starts basic processing and saves results in the database
<b>Reset</b>	<i>Reset</i> Reset all serial ports of the system
<b>Wait</b>	<i>wait [seconds]</i> Wait for a period of seconds
<b>//</b>	<i>// [text]</i> script remark

## **4.2. Scanning Procedures – FullScan and SnapScan**

The developed automated microscope system is able to scan the flow-through chamber in two different scan modes. The first mode will be referred to as “*FullScan*”-mode in this work because the microscope scans the entire flow-through-chamber at 100 positions horizontally in x and y direction in three different focal planes. Thus, a FullScan consists of 300 images in total, with 100 images per plane.

The second implemented mode will be referred to as “SnapScan” to emphasize that a snapshot is taken at one position at discrete time intervals. In this mode a single position is observed exclusively but the chamber is not scanned by the system. Instead of this, a time resolved scan can be taken at this specific position.

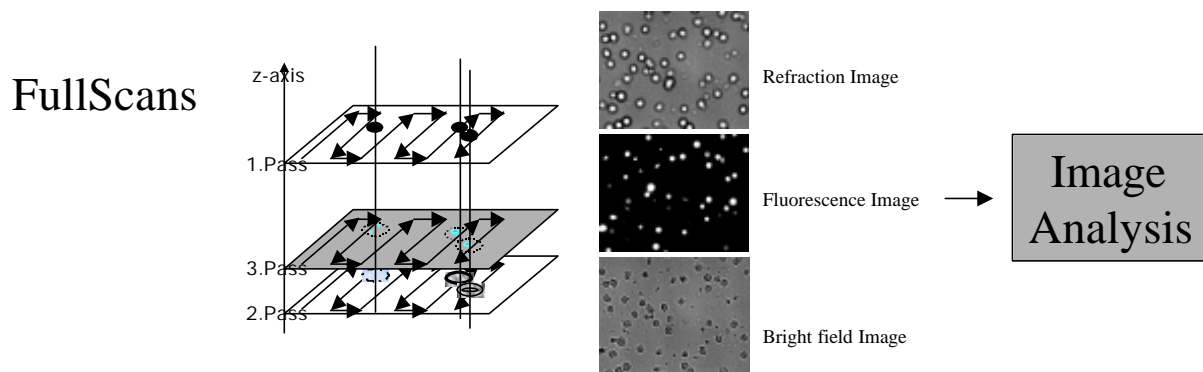
Both scan modes can be executed easily by the control-software in form of a script-file.

### **4.2.1. Scanning at different focal planes - FullScan**

As mentioned above, the flow-through-chamber is scanned in three different focal planes during a FullScan, with each plane scanned at 100 positions. The three planes were selected to obtain more information about the cells as it would be possible with only one image plane being observed. One of the three focal planes represents the conventional bright field plane, as a human observer would choose it. The second plane represents the so-called refraction image plane. This image plane is also known as the out-of-focus image plane, because the focal point of the objective lies outside the chosen object plane. The objects in this image plane come only into account if they do refract the light of the light-source and focus the light in the chosen “out of focus” image plane. All detected objects in an “out of focus” image will be referred to as “refractive active objects”. A model for this refraction effect will be described in the results section 5.3.1.

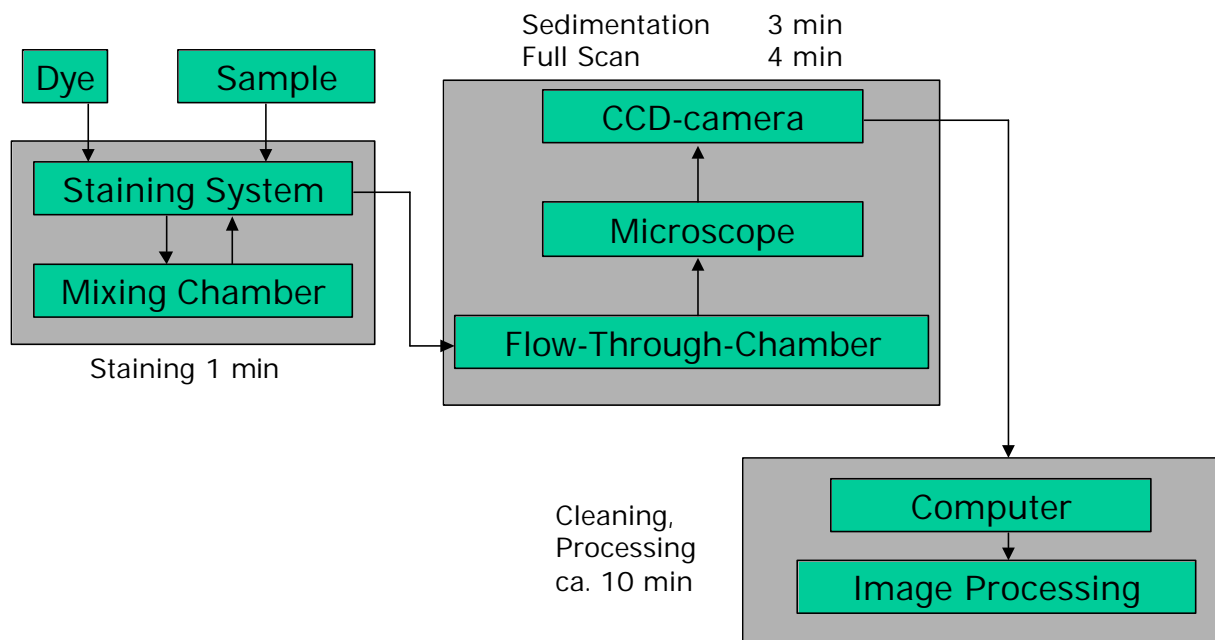
In the third image plane fluorescent events are observed. The detection of fluorescent events requires the addition of a fluorescence dye, which is added by the liquid-handling and staining system.

Fig. 4-2 shows the three image planes and the scan direction of the system. One image of every focal plane is shown as an example.



**Fig. 4-2 Different focal planes of a FullScan. Schematic on the left, shows the different focal planes; 1. Pass: Refraction Image, 2. Pass: Bright field image, 3. Pass Fluorescence Image. The images in the middle are examples of the three focal planes at one position of the flow-through-chamber taken during a FullScan.**

The general course of a FullScan measurement cycle is shown in Fig. 4-3. A run starts with loading of 1 ml cell suspension into the liquid handling syringe S1 (see Fig. 3-2). The cell suspension and the fluorescence dye (in this case DAPI) are mixed in the mixing chamber for 1min and then the stained cells are then loaded into the flow-through-chamber. After a sedimentation time of 3 min nearly all cells have settled on the bottom of the glass chamber and are lying in the same focal plane, ready for being scanned. The following FullScan takes approximately 4 min. All images are stored on hard-disk for subsequent image processing and analysis. In parallel the cleaning program is executed. Both programs together take approximately 10 min. In total a FullScan takes around 18 min including the image processing of the out-of-focus bright-field image and the in-focus fluorescence plane.



**Fig. 4-3 Schematic of a FullScan measurement cycle**

#### 4.2.2. Time resolved Scans – SnapScans

In addition to the possibility of generating Scans of the flow-through chamber at different focal planes a feature was implemented into the control software that allows the creation of time-resolved image sequences at a single position of the flow-through-chamber. SnapScans can be used to generate videosequences to demonstrate the morphological changes of the cells over the observed time (Fig. 4-4). The shutter of the microscope, which opens the uv-light path only when a fluorescence image is taken, prevents bleaching effects of the fluorescence dye, which can appear if the dye is not uv-light resistant. This makes it feasible to observe the dye uptake over a long period of time without any bleaching effects. After a SnapScan has been taken the image series can be overlapped in the subsequent image processing to create multilayer video-sequences. These videosequences give a better insight into the behavior of cells over a long period of time at a single position of the flow-chamber. Furthermore, the fluorescence signal can be quantified and gives an insight into the dynamics of the process of for example the dye uptake by the cells (see chapter 5.2. Morphological Studies).

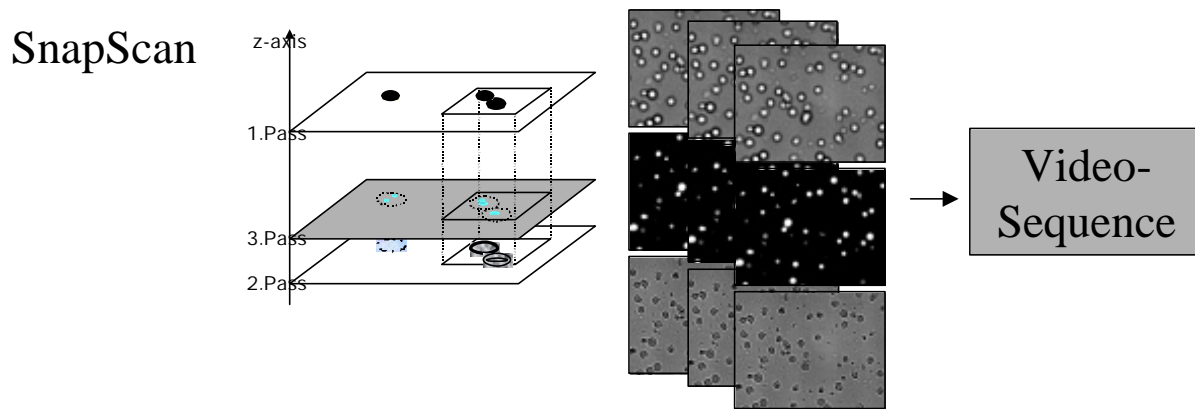


**Fig. 4-4** Time resolved scan at a single position of the flow-through chamber. Number of saved images planes can be flexibly selected.

### ***4.3. Principles of Image Processing Algorithms***

In the following chapters algorithms developed for image processing and analysis of the different image planes of the FullScans will be described. A specific algorithm was developed for the analysis of each of the three planes. The first algorithm described is the “out of focus” algorithm, which was developed for the analysis of the images taken from the refraction image plane. Next an algorithm will be described, which was used for analyzing all the morphology of the “nearly in focus” bright field images and lastly the fluorescence events counting algorithm will be described.

#### **4.3.1. “Out-of-focus” algorithm**

The algorithm for analysis of the “out-of-focus” plane with its refraction images is schematically shown in the block diagram in Fig. 4-6. The image processing starts with brightening up of the incoming gray-level image by using a lookup table transformation. The exponential correction used expands high gray-level ranges while compressing low gray-level ranges. This means the transformation decreases the overall brightness of an image and increases the contrast in bright areas at the expense of the contrast in dark areas. Subsequently the image is inverted so the bright gray-levels get darker and vice versa. In the following a smoothing convolution filter is used to attenuate the variations of light intensity in the neighborhood of a pixel. This smoothes the overall shape of objects, blurs edges, and removes details. The smoothing kernel (type 0), which has been used for smoothing in all cases, is shown in Fig. 4-5. After smoothing, the image was eroded by a very similar kernel (type 1) also shown in Fig. 4-5.

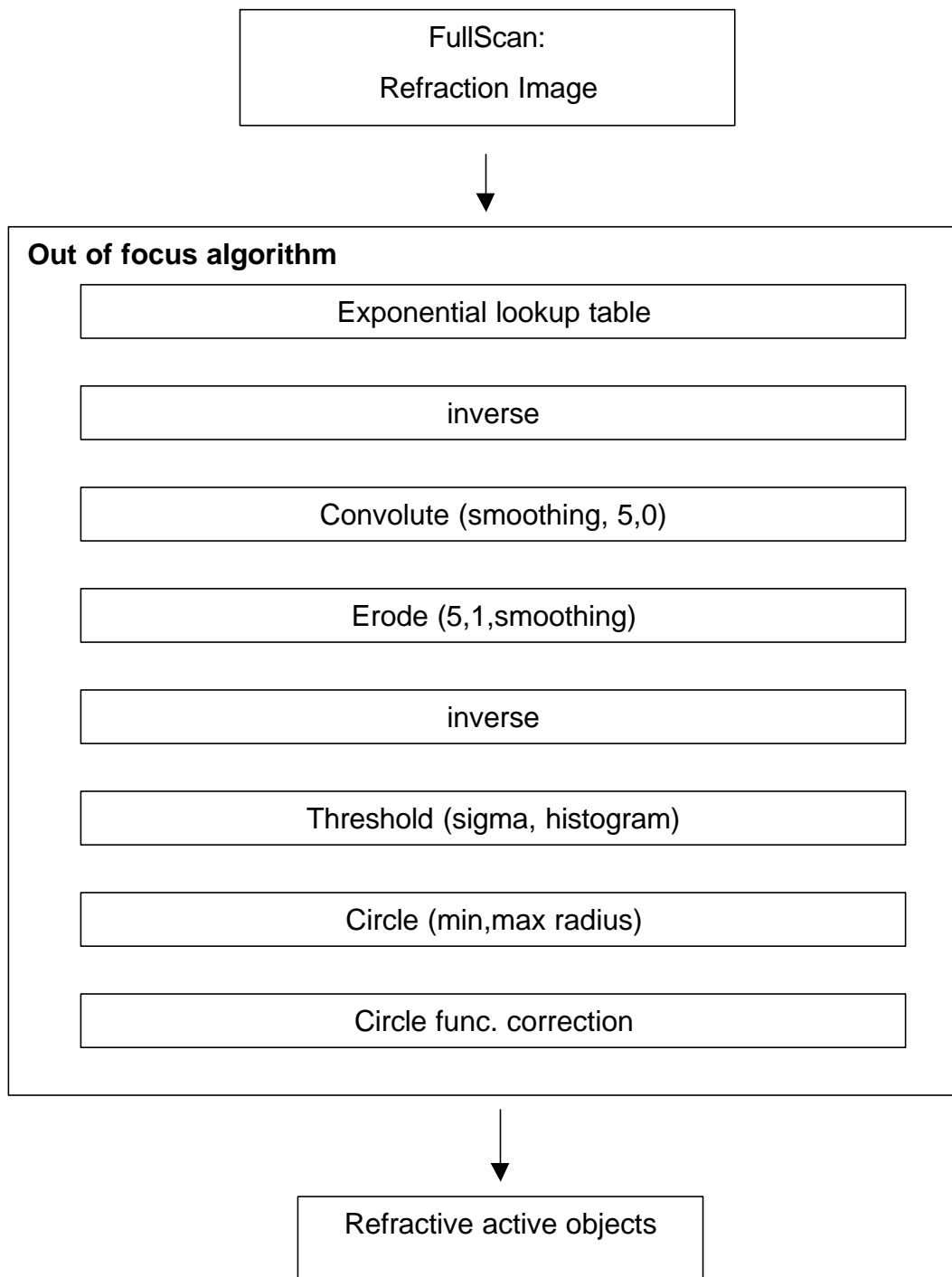
After the image is eroded it is inverted and the threshold is calculated to generate a binary image in which background and objects are separated by different values. The threshold calculation is based on the method described in chapter 4.3.2. As soon as all objects have been separated by the threshold function, the image is analyzed using the IMAQ circles function. This function separates overlapping circular particles. The circle function uses the Danielsson coefficient to reconstitute the form of a particle, provided that the particles are essentially circular. The particles are treated as a set of overlapping discs that are subsequently separated into separate discs. Therefore, it is possible to trace circles corresponding to each particle. Unfortunately the original IMAQ circle algorithm is error-prone, because some particles are detected as more than one circle. For this reason, the algorithm was extended with a correction function to eliminate circles counted more than once. The correction is based on the assumption that two separate objects must have a distance of at least half of their diameter before they can be counted as two separate objects. Therefore, the correction algorithm filters out all circles, whose center lies inside the radius of another circle (Labview source code see appendix Fig. 8-8).

1	1	1	1	1
1	1	1	1	1
1	1	0	1	1
1	1	1	1	1
1	1	1	1	1

1	1	1	1	1
1	1	1	1	1
1	1	1	1	1
1	1	1	1	1
1	1	1	1	1

**Fig. 4-5** Kernels Used for smoothing and erosion in the out-of-focus algorithm



**Fig. 4-6 Overview of the "out of focus algorithm" used in the program OLM for cell counting.**

#### 4.3.2. “Nearly-in-focus” algorithm

The image processing and analysis of the “nearly-in-focus” bright field image plane was the most difficult part of the analysis of all FullScan image planes, because of the isolation of low contrast structures from the background and the high demands on computing power.

In general, bright field images of mammalian cells are low in contrast when the cells are unstained. Thus, a new algorithm was developed combining two different approaches, which are normally used separately.

One part of the algorithm isolates the membrane structures of the cells, on the basis of their high contrast differences. The second part of the algorithm releases the inner cell structures from the background, on the basis of their different gray values in comparison to the average of all background pixels. In the subsequent step the isolated structures are added and processed further through a series of binary filters. Fig. 4-7 shows major steps of the algorithm and the images below the diagram illustrate the effects of some of the major image processing steps. The image series starts with the original image (1) that shows four cells in the center and two cells touching the border of the image. Image (2) shows the isolated membrane structures and image (3) depicts the isolated inner cell structures. Both images are merged and the result of the merging can be seen in image (4). In image (5), all holes in the objects have been filled, labeled and separated but any objects touching the border have not been removed yet.

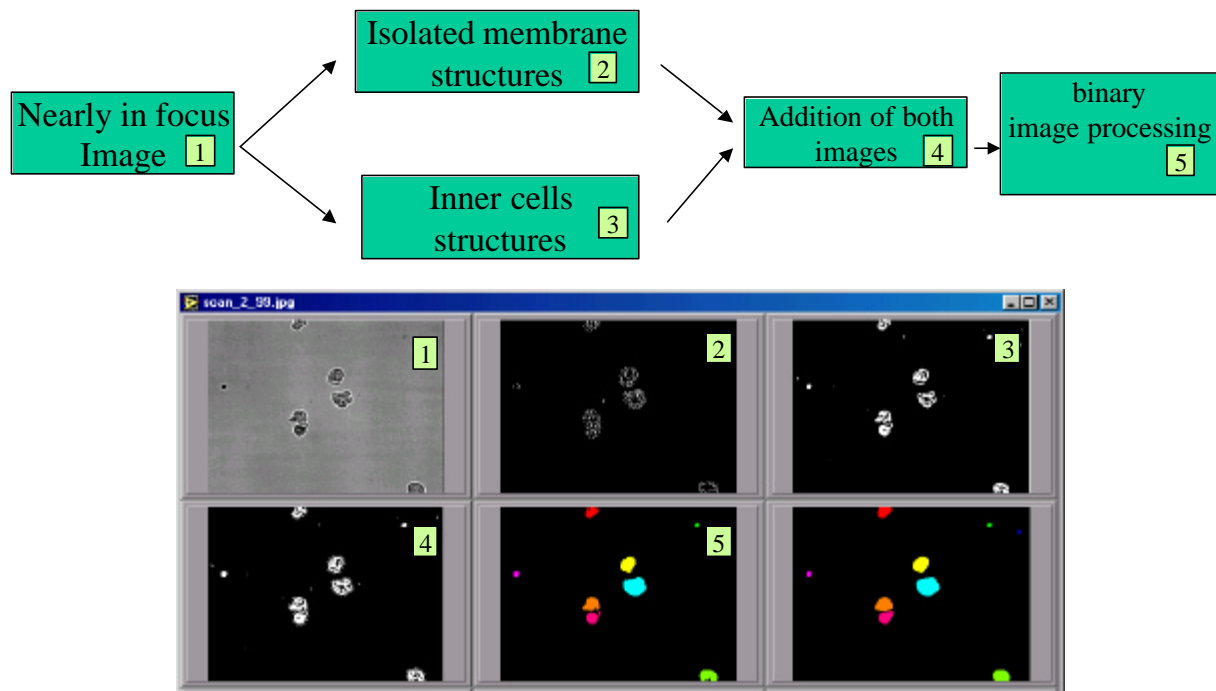


**Fig. 4-7 Principle of the morphological image analysis of one bright-field image plane of a FullScan.**

The “isolation of membrane structures” part of the “nearly in focus” algorithm starts with the IMAQ Nth-Order function, which also acts as a smoothing filter. The “Nth Orders” function orders, or classifies, the pixel values surrounding the pixel being processed. The data is placed into an array and the pixel being processed is set to the nth pixel value, the nth pixel being the ordered number. A 3x3 matrix was found to be the best array size in combination with the fourth order. After the filtration is finished a specialized edge detection method (IMAQ canny edge detection) is performed to isolate all cell membrane structures from the background.

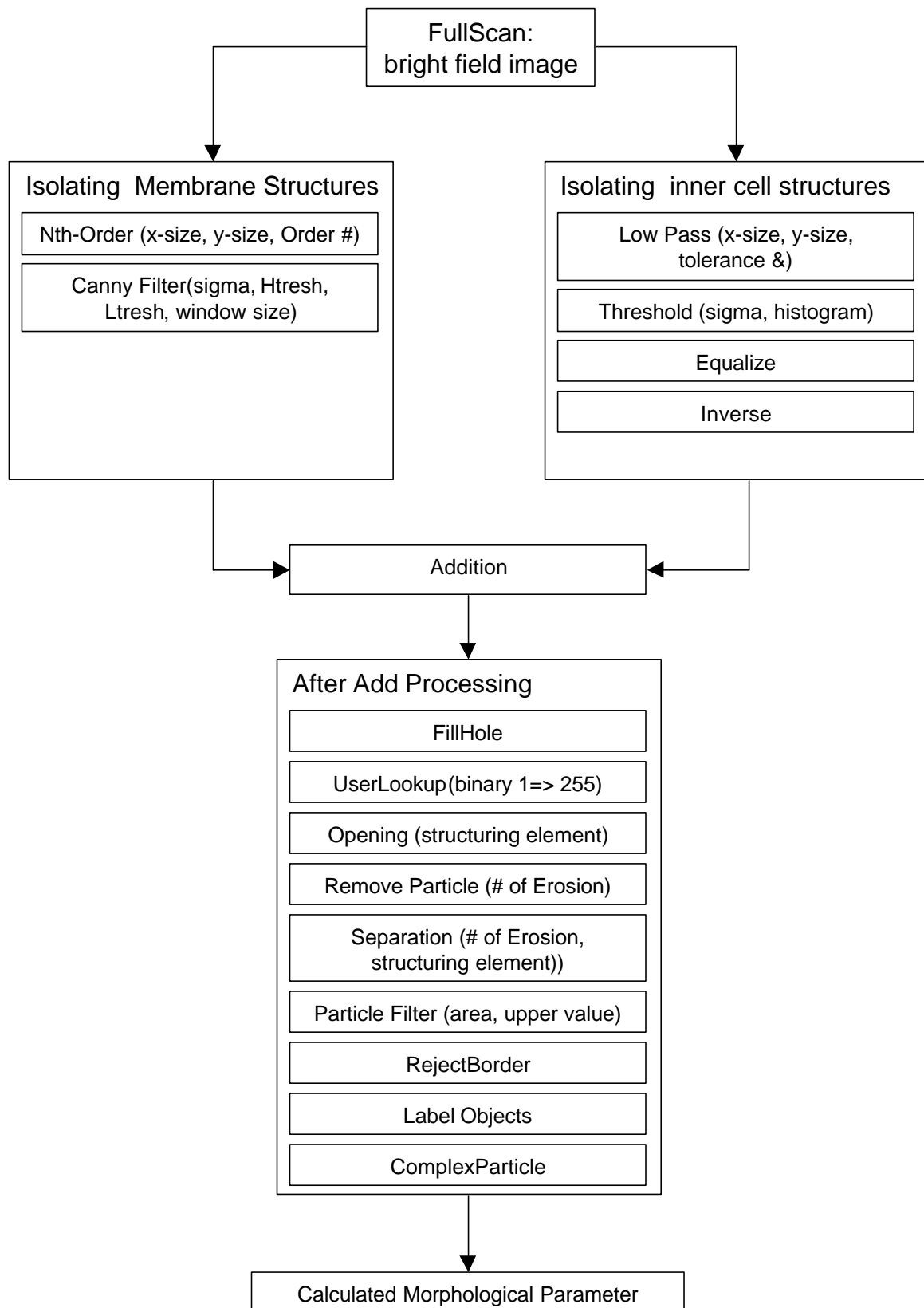


**Fig. 4-8 Structure of the developed “nearly in focus” algorithm to isolate morphological parameters describing objects isolated from bright-field images**

---

Parameters for the IMAQ CannyEdgeDetection:

**Sigma** is the sigma of the Gaussian smoothing filter that is applied to the image before the edge detection is done.

**H Thresh** (High Threshold) defines the upper percentage of pixel values in the image from which the seed or starting point of an edge segment is chosen. It takes values from 0 to 1.

**L Thresh** (Low Threshold) is multiplied by the H Thresh value to define a lower threshold for all the pixels in an edge segment.

**Window Size** defines the size of the Gaussian filter that is applied to the image. This size must be odd.

After isolation of the membrane structures the IMAQ CannyEdgeDetection transformed image is ready for the addition as shown in Fig. 4-7.

In the second in parallel running part of the “nearly in focus” algorithm, the image processing starts with a low pass filter to blur the image structures. The low pass filter calculates the inter-pixel variation between the pixel being processed and the pixels surrounding it. If the pixel being processed has a variation greater than a specified percentage, it is set to the average pixel value as calculated from the neighboring pixels. For used parameters see Fig. 4-10. After filtering, a specifically developed threshold-algorithm determines the threshold for building a binary image on the basis of an analysis of the histogram of the given image. On the assumption that the image contains more gray-levels, belonging to the background of the image, the main peak in the histogram represents the background peak. The algorithm calculates the mean value and the standard deviation. A sigma is defined which represents a factor multiplied with the standard deviation of the mean value. The calculated value defines the width in which the main peak is cut out of the histogram. By calculating the mean value and the factor sigma all gray-levels belonging to the background, can be cut out so only the object information of the image remains as shown in Fig. 4-9. The threshold function results in a binary image with the values 0 and 1. A subsequent equalizing function in combination with an image inversion converts all pixels with the value 1 into the value 255.

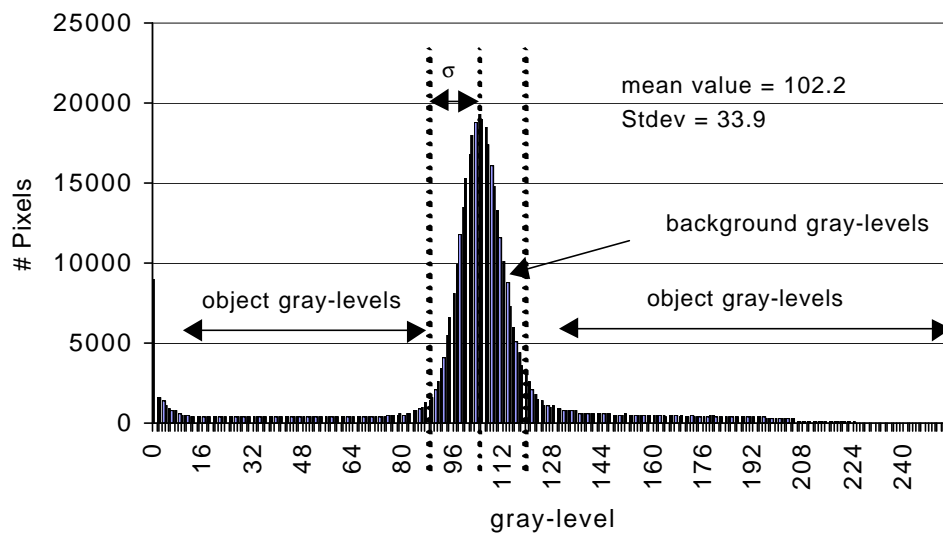


**Fig. 4-9** Histogram of a "nearly in focus" bright field image. All background levels are located around the mean value. The object values are located left and right of the background peak.

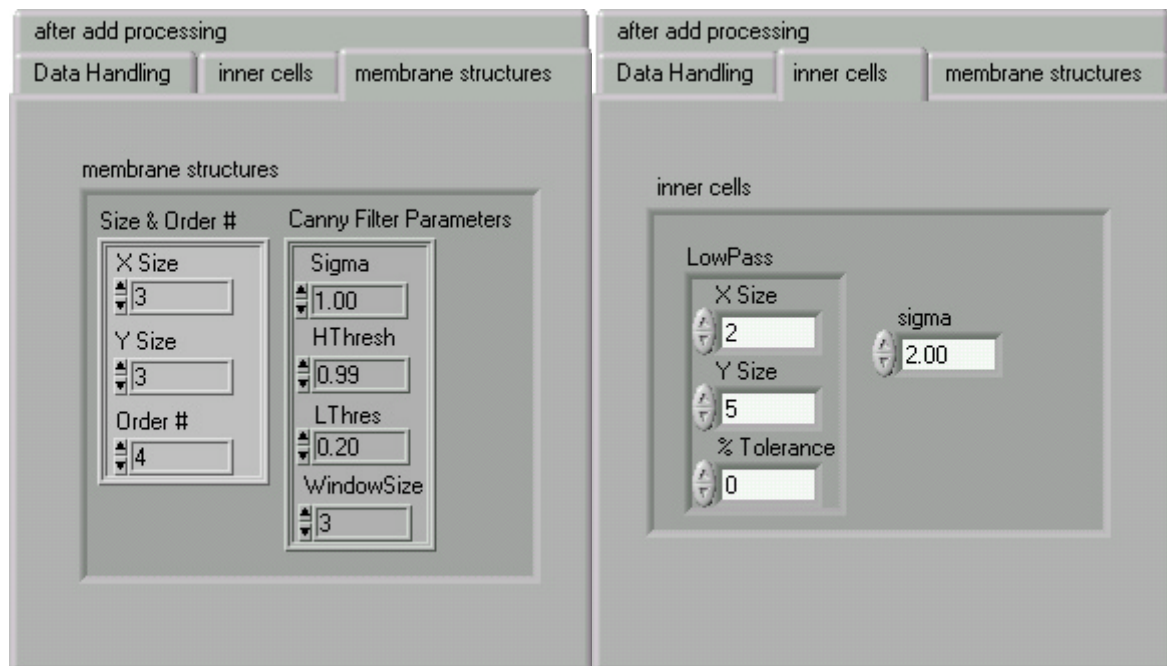


**Fig. 4-10** Default preferences of both algorithm parts: isolating "membrane structures" and isolating "inner cell structures"

After both image have been added several advanced IMAQ vision functions are used for further processing of the binary image. Firstly, the IMAQ Fillhole function is used for hole filling. The function results in a binary image with a value range between 0 and 1. For all

further processing it is necessary to convert the image into a binary form of 0 and 255, that is realized using a lookup-table. After correction, the binary image is treated with an opening function. The opening function is an erosion followed by a dilation. This function removes small particles and smooths boundaries. As structuring element a 3x3 matrix with the value 1 was used in all experiments. The following “IMAQ removeParticle” function eliminates or keeps particles resistant to a specified number of 3x3 erosions. The particles that are kept are exactly the same as those found in the original source image. Subsequently the IMAQ separation function is used to separate touching particles, particularly small isthmuses found between particles. It performs n erosions (n = Number of Erosion) and then reconstructs the final image based on the results of the erosion. If an existing isthmus is broken or removed during the erosion process, the particles are reconstructed without the isthmus. The reconstructed particles, however, have the same size as the initial particles except that they are separated. If no isthmus is broken during the erosion process, the particles are reconstructed as they were initially found. No change is made. A particle filter is then used to eliminate small objects from the image. The filter removes particles in an image according to their morphological measurements. In the following step all particles are removed that touch the border of the image. These particles might have been truncated during the digitization of the image, and their elimination will, therefore, be useful to avoid erroneous particle measurements and statistics. Finally, all particles are labeled and analyzed on the basis of their morphology by the IMAQ “complexParticle” function. All parameters that were used as default values are shown in Fig. 4-11.

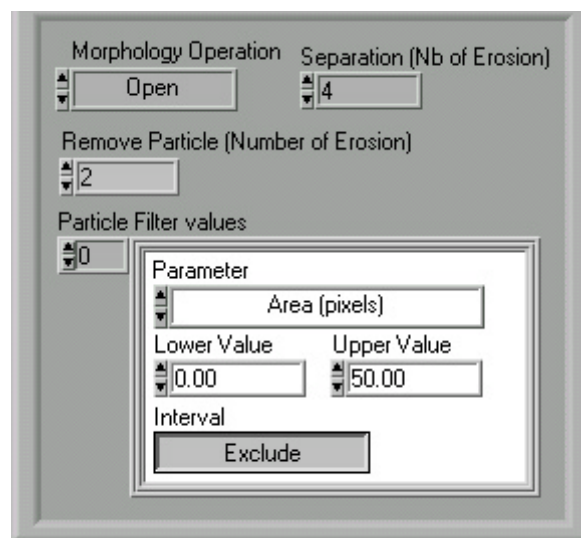


**Fig. 4-11 After Add Processing default values**

### 4.3.3. Morphological Parameters

The “nearly in focus” algorithm describes all particles found in the images by a large number of morphological parameters. The IMAQ function “complex Measure” calculates the coefficients of all detected particles and returns a set of measurements made from particles in a binary image. A selection of these parameters is stored in the morphology database.

**Tab. 4-2 Morphological parameters stored in the morphology database**

<b>Name</b>	<b>Description</b>
<b>Area (pixels)</b>	Surface area of particle in pixels
<b>Perimeter</b>	Length of outer contour of particle in user units
<b>Mean intercept perpendicular</b>	Mean length of the chords in an object perpendicular to its max intercept
<b>Ratio of equivalent ellipse axis</b>	Fraction of major axis to minor axis
<b>Ratio of equivalent rectangle sides</b>	Ratio of rectangle big side to rectangle small side
<b>Elongation factor</b>	Max intercept/mean perpendicular intercept
<b>Compactness factor</b>	Particle area/(breadth × width)
<b>Heywood circularity factor</b>	Particle perimeter/perimeter of circle having same area as particle
<b>Type Factor</b>	A complex factor relating the surface area to the moment of inertia
<b>Hydraulic Radius</b>	Particle area / particle perimeter
<b>Waddel disk diameter</b>	Diameter of the disk having the same area as the particle in user units

### 4.3.4. “In-focus” algorithm

For the calculation of the threshold, an automatic threshold function of the Labview IMAQ vision package was used. The best automatic threshold function was empirically determined by numerous test images and the Vision Builder Program from National Instruments. It turned out, that the metric method works best for solving the segmentation problem of an image in a particle region and a background region. After thresholding, the now binary images can be easily counted out with the IMAQ circles function. Ideally, every counted object corresponds to a stained cell nucleus. The entire algorithm for counting stained cell nuclei is shown in Fig. 4-12 in form of Labview source code.

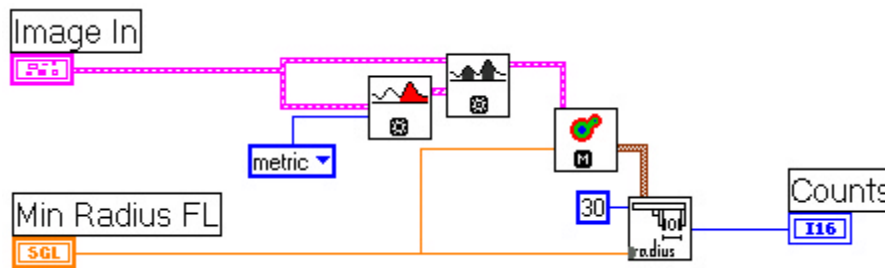


Fig. 4-12 Labview source code of the "in-focus" algorithm

**4.4. Overview of used algorithms and calculation formulas**

This chapter gives an overview about the used algorithm and subsequent calculations to obtain cell culture specific parameters as cell concentration and viability. Fig. 4-13 summarizes the different algorithms and the calculation formulas used.

For the calculation of absolute cell concentration a correction factor *c* was introduced on the basis of the flow-through chamber geometry and comparison with manually counted samples. To generate absolute concentrations all data must be multiplied with the correction factor.

**Correction factor *c*:**

$$c = n_{\text{images per plane}} \cdot f_{\text{chamber geometry factor}} \cdot s_{\text{scale factor}}$$

**Tab. 4-3 Parameters for the calculation of the correction factor *c***

$n_{\text{images per plane}}$	100	FullScan: 100 images per image plane
$f_{\text{chamber geometry factor}}$	$\frac{1}{1.2}$	Empirically determined on the basis of chamber geometry
$s_{\text{scale factor}}$	1000	$\mu\text{l} \rightarrow \text{ml}$

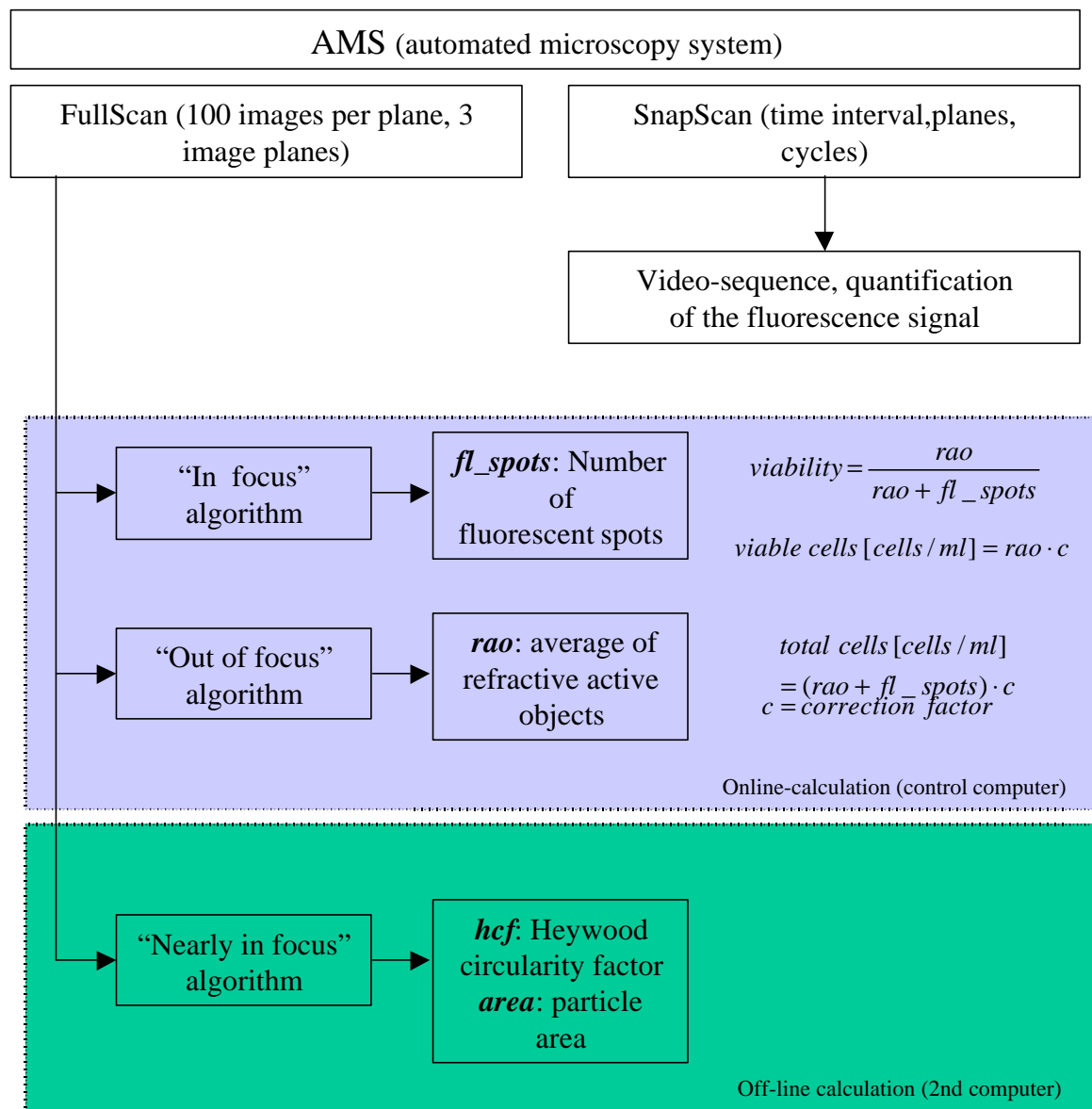


Fig. 4-13 Relation between used algorithms and subsequent calculations

#### 4.5. Autofocus Calibration Procedure

An autofocus routine is integrated into the developed system, which completely scans the mounted flow-chamber at the startup of the entire system. This procedure corrects adjustment failure, which can occur if the flow-through-chamber is not mounted rectangular onto the microscope stage in relation to the optical pathway of the microscope.

The algorithm scans the chamber at 100 positions in 50 image planes in z-direction around a previously given default value. At each of the 5000 scanned positions the focus function is calculated and the extremum of the function is saved in a matrix, which is stored in a preference file on disk. The saved matrix represents the 3D profile of the scanned flow-chamber. Thus, the preference file serves, as the basis for all FullScans or SnapScans executed later where a correct finding of the right focal plane is extraordinarily important.

In this case the used focus function was previously tested by Groen *et al.* as one of the best of 11 functions for bright-field microscopy [Groen *et al.*, 1985]. The autofocus function belongs to a group of focus functions which measures the image contrast by intensity variance or standard deviation [Price and Gough, 1994].

$$F_{focus} = \mathbf{s}^2 = \frac{1}{n(n-1)} \left( n \sum_{ij} g_{ij}^2 - \left( \sum_{ij} g_{ij} \right)^2 \right)$$

$n = i \cdot j$ ; Total number of pixels in the image  $g$

In the appendix, Fig. 8-4 shows the Labview source code of the translation of the autofocus formula above.

## 5. Results

The results chapter can be divided into two parts. The first part contains all results of testing different autofocus functions that were investigated during the development of the system. As a result of these experiments one of the tested functions was chosen and was integrated into the calibration procedure of the developed system. This autofocus function was then used for the calibration of the system in all following experiments.

All the subsequent results described in the second part were generated with the final system. This starts with a presentation of results of different SnapScans that describe morphology changes under defined conditions and is followed by the use of FullScans to describe the change of cells during cultivation in bioreactors.

### ***5.1. Comparison of different auto-focus functions***

Reliable autofocus is required to obtain accurate measurements of fluorescent stained cells from a system capable of scanning multiple microscope fields. Problems may have many causes, including mechanical instability of the microscope (gear slippage, settling between moving components in the stage), adjustment failures and irregularity of glass slide surfaces. In the case of the automated microscope used in the present work, a flow-through-chamber was firmly fixed onto the microscope stage, but it was extraordinarily difficult to center the plane of the chamber at exactly 90° to the optical path of the microscope. In addition, the chamber glass bottom was bent, because of tensions caused by the screws, which fixed the chamber glass bottom to the top of the chamber. Experience has shown that it is not possible to maintain focus simply by determining the best foci at two or four points on the flow-through-chamber and scanning along the line between them in three-dimensional space. Therefore, an autofocus system had to be introduced to reach a constant positioning in z-direction across the entire scanned microscope field. Hence, several autofocus functions were tested with regard to their ability to detect the sharpest focal plane and of the computer time needed for calculation.

On the right of Fig. 5-1 a selection of autofocus functions is shown that were previously reviewed by Price and Gough (1994) and were used in the present work as the basis for all performed autofocus experiments. The purpose of the work of Price and Gough was to test the suitability of these functions for both phasecontrast and fluorescence microscopy, whereas the developed AMS here works with bright-field and fluorescence images.

However, Groen *et al.* (1985) reported the functions F1, F2 and F5 in Fig. 5-1 to be the best of 11 functions tested also for bright-field microscopy. On the basis of these results, a selection of autofocus functions, published in a review of Price and Gough were used to test their capability for detecting the best focal plane as an extremum of the autofocus function. In their review Price and Gough subdivided the described autofocus functions into three separate groups based on different autofocus models:

The models are:

- 1. resolution model**
- 2. contrast model**
- 3. autocorrelation model**

Two functions of each group were chosen for the experiments. The first group contained the functions F1 and F2 based on the resolution model. In this model details blur as the image moves out of focus. Resolution can be measured by analyzing the Fourier frequency spectrum or by the application of gradient or high-pass filters that isolate the high frequencies. The magnitude of high frequencies or gradients can then be used as a measure of resolution, which is defined as a maximum at best focus [Pierce and Gough, 1994].

The second group contains two functions, which are based on the contrast model. In this approach the assumption is made that an image consists of light and dark regions, the light regions become darker and dark regions become lighter as the focal plane of the objective is moved farther from the focus. As examples for such functions the functions F5 and F6 were chosen. Function F5 measures the statistical variance of the intensity as a measure of contrast. F6 is the standard deviation of the intensity, or the square of F5.

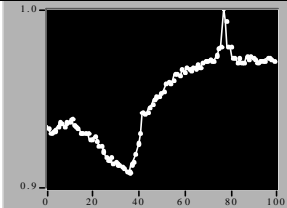
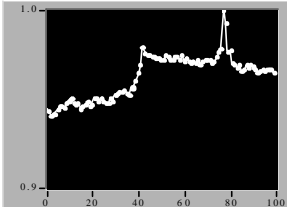
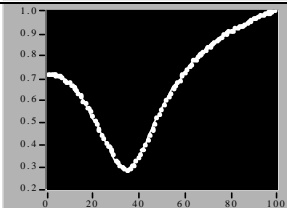
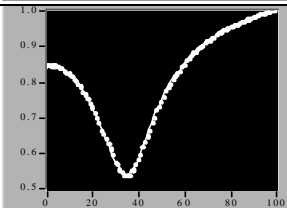
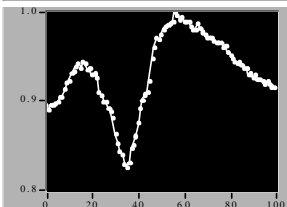
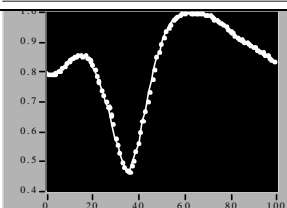
The third group comprises two functions, which are based on autocorrelation. The theory supporting this kind of autofocus function is discussed by Vollharth *et al.* and the reader is referred to these sources for details. The functions F9 and F10 were selected as examples [Vollharth *et al.*, 1988].

### 5.1.1. Evaluation of autofocus functions on bright-field images

Fig. 5-1 also shows results of the selected autofocus functions applied to a set of bright-field images taken from one position of the flow-through chamber at different image planes. At this position the microscope field was scanned in z-direction in regular increments of 1  $\mu\text{m}$ . The created stack of images was saved to disk and analyzed later with all focus functions of Fig. 5-1. As specimen a CHO suspension cell line was used.

All results of the focus functions in Fig. 5-1 show extrema close to 40  $\mu\text{m}$  but differed in signal quality. F1 and F4 are overlapped with noise and in contrary to all other functions F4 shows a local maximum at 40  $\mu\text{m}$ . Both functions (F1, F4) also show a strong peak near 80  $\mu\text{m}$ .

The two tested contrast model functions show a smooth course without any spikes or detectable noise. Function F9 and F10 are very similar but F9 is overlapped with some noise.

F(Z)	F(Z) serie: nek_1_XX	Calculation Time [s]	Function (Lit. [148])
F1		30	$F_1 = \sum_{ij} ([1 \ 0 \ -1] \otimes g_{ij})^2$
F4		30	$F_4 = \sum_{ij} \left( \begin{bmatrix} -1 & -2 & -1 \\ -2 & -12 & -2 \\ -1 & -2 & -1 \end{bmatrix} \otimes g_{ij} \right)^2$
F5		18	$F_5 = \frac{n \sum_{ij} g_{ij}^2 - \left( \sum_{ij} g_{ij} \right)^2}{n(n-1)}$
F6		40	$F_6 = \sqrt{F_5}$
F9		30	$F_9 = \sum_{i,j} g_{i,j}^2 - \sum_{i,j} g_{i,j} g_{i+1,j}$
F10		51	$F_{10} = \sum_{i,j} g_{i,j} g_{i+1,j} - \sum_{i,j} g_{i,j} g_{i+2,j}$

**Fig. 5-1** Plots with the results of the calculations of different focus functions (Pierce and Gough, 1994). A stack of 100 images taken from CHO cells in a regular distance of 1  $\mu\text{m}$  was used as the basis for all calculations.

### 5.1.2. Autofocus functions applied to bright field and fluorescence images sets

The next experiment was performed in the same way but DAPI stained hybridoma cells were used as specimens. A microscope field was selected containing normal, unstained cells and membrane permeable cells, which were stained with the dye. Two image sets were taken from this field, a bright field and a fluorescence image set, and all focus functions were calculated for both sets.

To test the ability of the focus functions to indicate the sharpest focal plane by an extremum also in images with a reduced resolution, the original image sets were scaled down in six steps from the original size of 512x512 pixel to a size of 8x8 pixel. All functions were computed with the original images and with reduced image sizes. Fig. 5-2 shows the results of all focus functions. Each colored line in the plot represents a reduction level, starting with the green one that shows the result of the focus function calculated with the original image set.

With regard to the detection of the sharpest focal image plane of the bright field image set, neither of the resolution model functions F1 and F4 can reliably detect the sharpest focal point.

Only function F5 and the two autocorrelation functions F9 and F10 are able to detect the sharpest focal point in both, the bright-field and the fluorescence image sets. However, only the function F5 gives a significant signal (minimum) even over a wide range of the reduced image sets. The autocorrelation function F10 achieves a minimum in the calculation of the sharpest focal point for the bright field image sets, but for the fluorescence images the function achieves a maximum in contrast to all the other functions, which achieve the same extremum for both image sets.

Fig. 5-3 shows that the needed calculation time is very similar for all functions. In case of the size-reduced image sets the calculation time decreases exponentially during the first three reduction steps, after that the calculation time is constantly low.

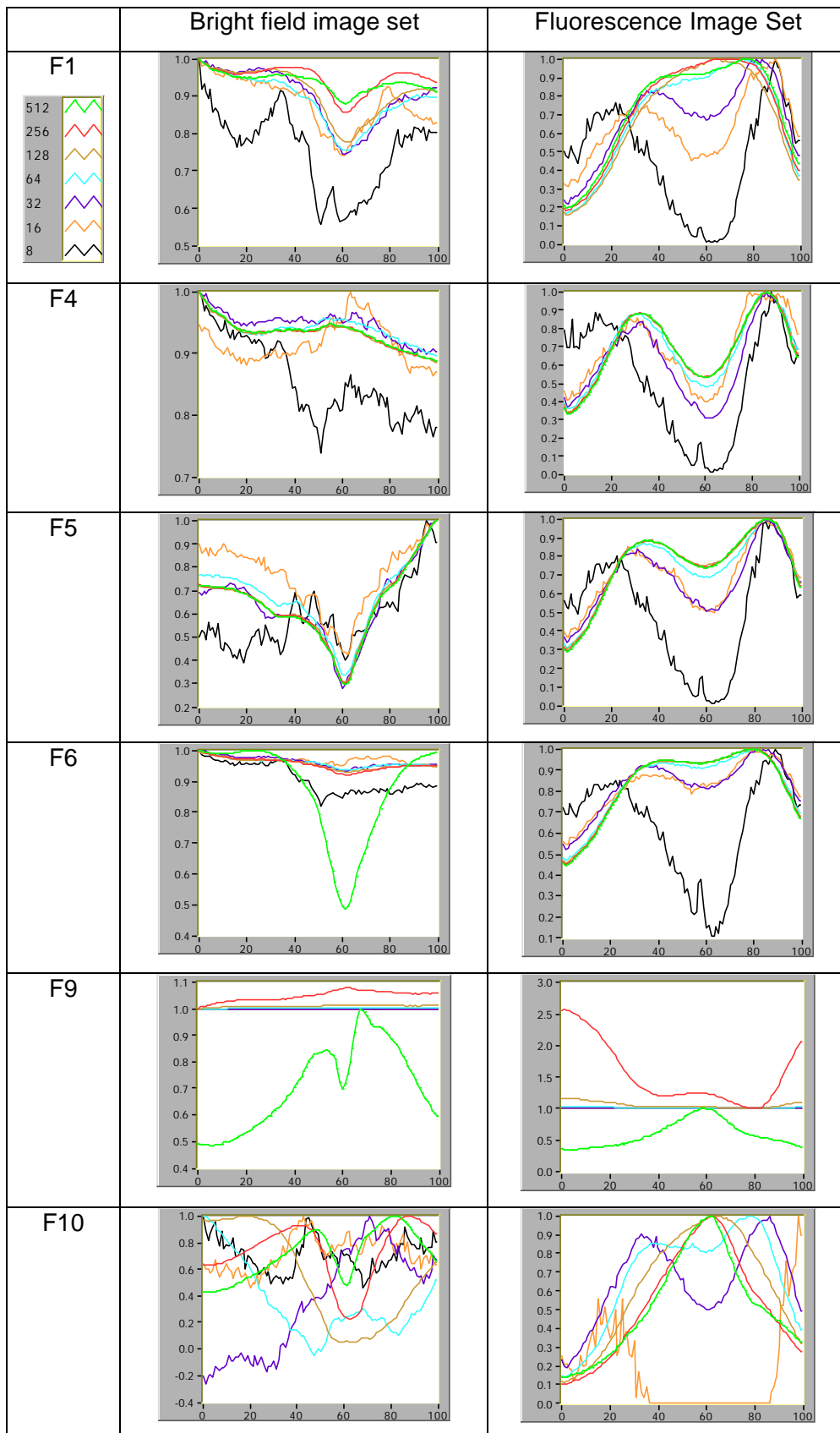


**Fig. 5-2 Autofocus functions of original and size-reduced images of hybridoma cells (bright-field, fluorescence images). X-axis: # image; Y-axis: function amplitude**

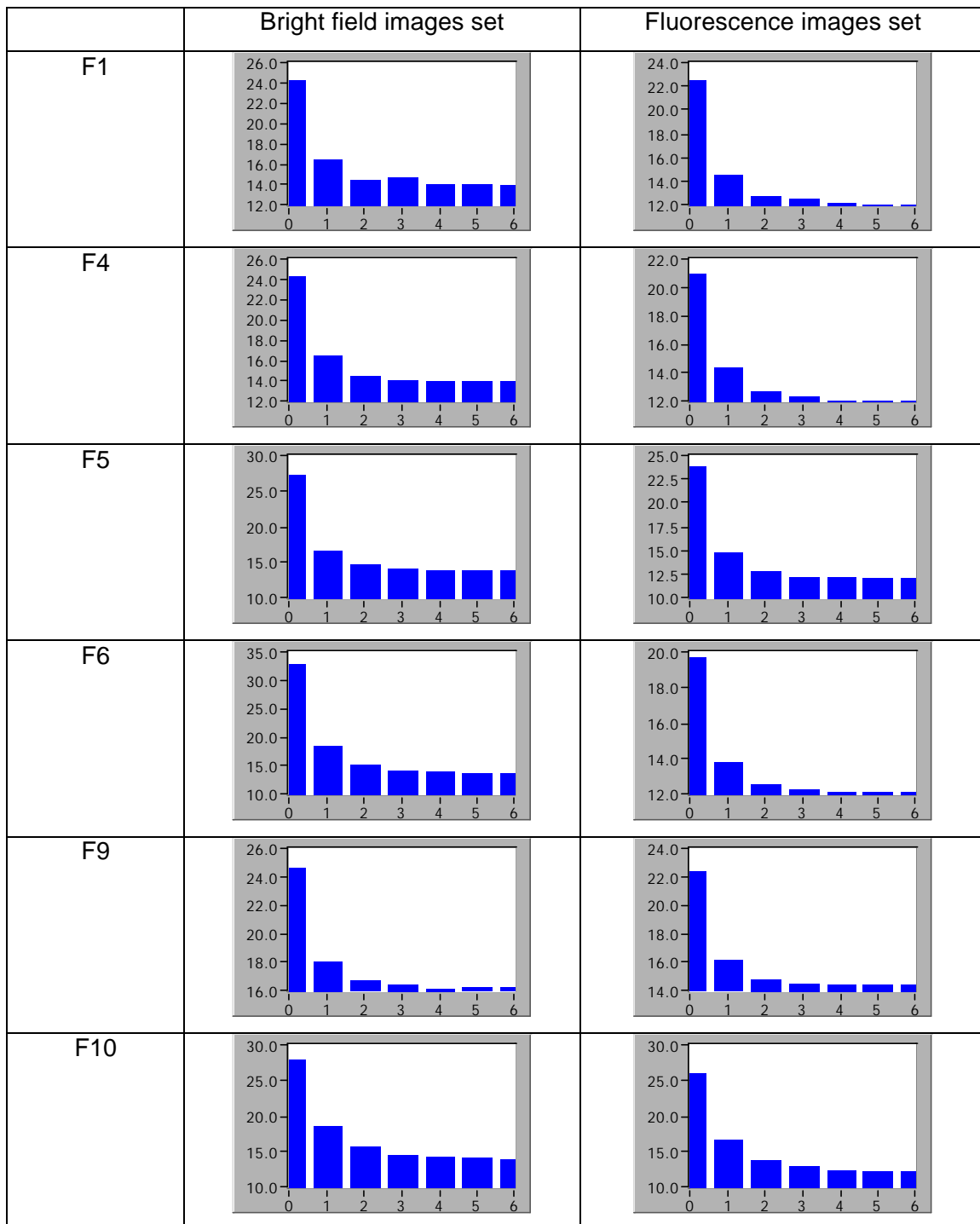


Fig. 5-3 Calculation time for original and reduced image sizes (bar # 0 = 512x512 pixel, 1=256x256; 2= 128x128; 3= 64x64; 4= 32x32; 5= 16x16; 6= 8x8).

### 5.1.3. Focus Functions and Microspheres

Another experiment was performed under the same conditions as described before but instead of living cells, fluorescent styrol beads or microspheres with a similar diameter to hybridoma or CHO cells ( $\sim 15 \mu\text{m}$ ) were used. Fig. 5-5 shows the results of this experiment. It can be seen that the results of the analyzed bright field image sets are not encouraging. All curves are strongly noise-vested and where a main extremum can be detected at all, the peaks are accompanied by side peaks of similar size (functions F5, F6 and F9). Only the contrast functions allow an evaluation of the sharpest focal plane, but in the case of the size reduced image sets, the detection of the sharpest focal plane in the bright field image sets does not fit very well, especially for function F6.

In contrast, the calculated focus functions of the fluorescence image sets show smooth curves with a strong unimodal minimum. Only the autocorrelation functions are non-uniform. Function F9 shows both, minima and maxima in dependence of the image size while F10 shows minima at different positions and a in regard of the size-reduced images only a small dynamic signal range.

### 5.1.4. Implemented autofocus calibration procedure

In the final developed system, the autofocus on the basis of the autofocus function F5 was implemented as a calibration procedure. This calibration procedure has to be executed after the start-up of the system for the first time, and in any case, after the flow-through chamber has been disassembled or the stage control unit has been switched off. A detailed description of the calibration procedure has been already given in chapter 4.5. An example of the 3D profile of the calibrated flow-through chamber demonstrates Fig. 5-4. This is generated automatically by the control software as soon as the calibration procedure is finished and serves as a control of the calibration.

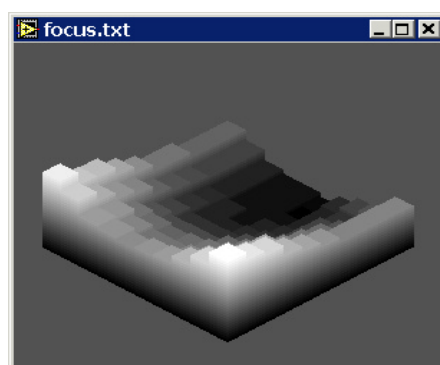


**Fig. 5-4 Schematic 3D-profile of the flow-through-chamber bottom**

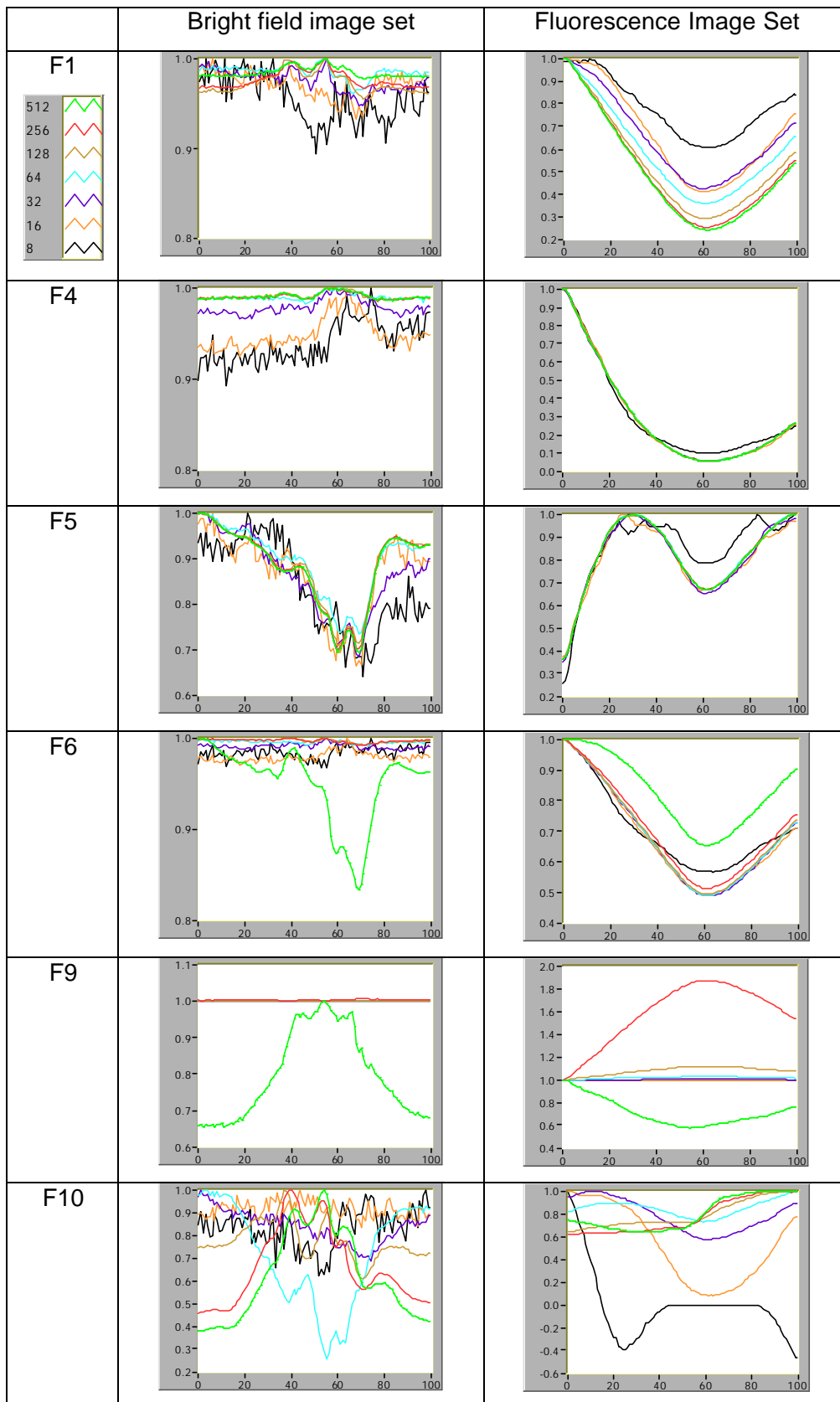


**Fig. 5-5 Autofocus functions of original and size-reduced images of microspheres particles (bright-field, fluorescence images). X-axis: # image; Y-axis: function amplitude**

---

## **5.2. Morphological Studies - SnapScans**

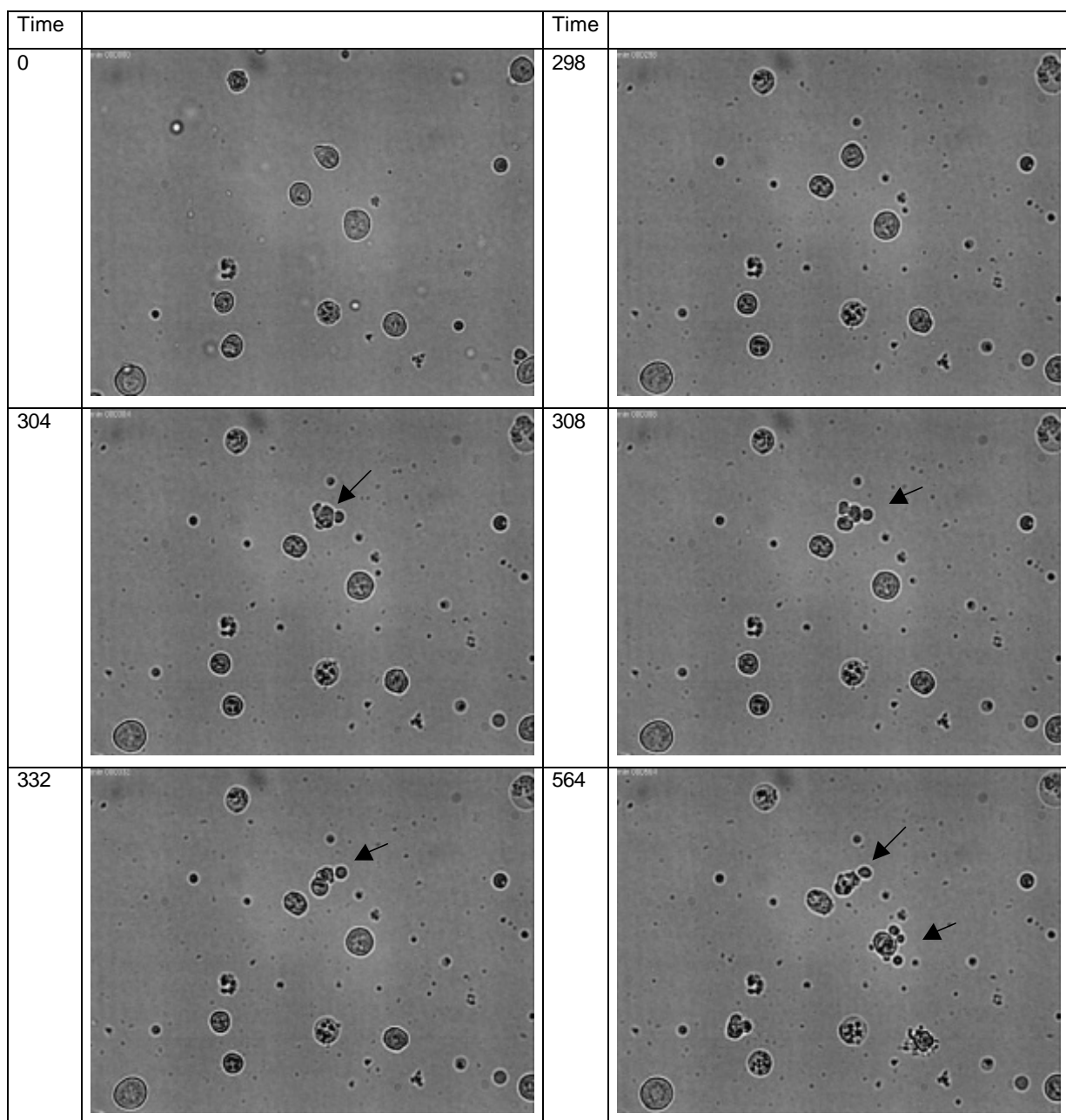
### 5.2.1. Bright Field Focal Plane SnapScan

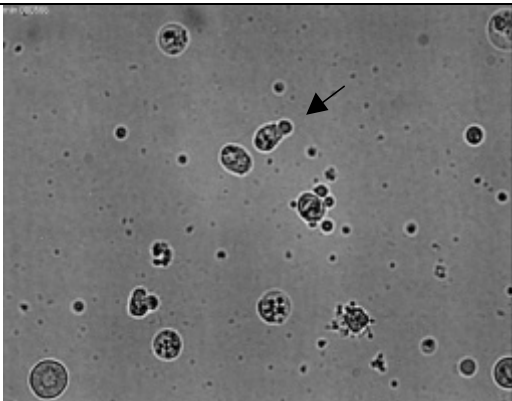
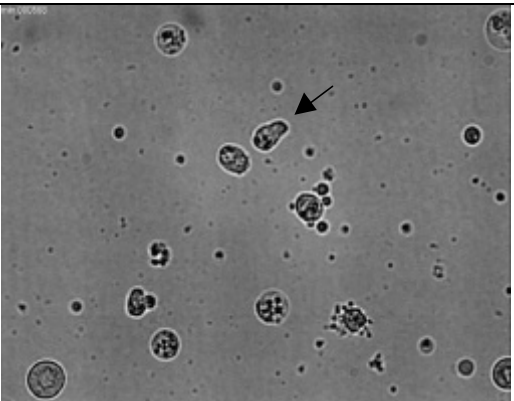
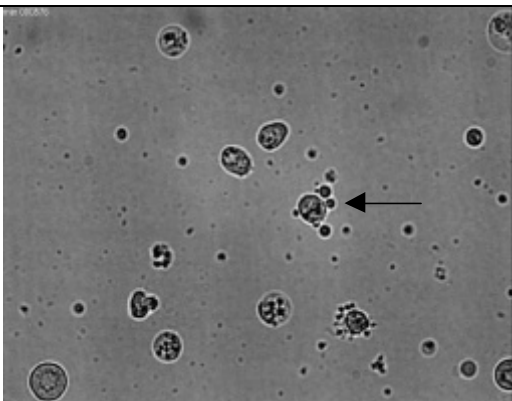
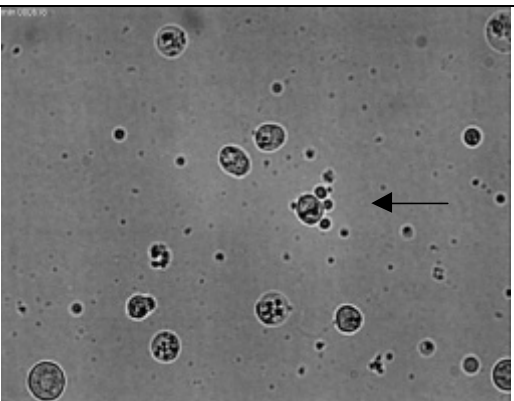
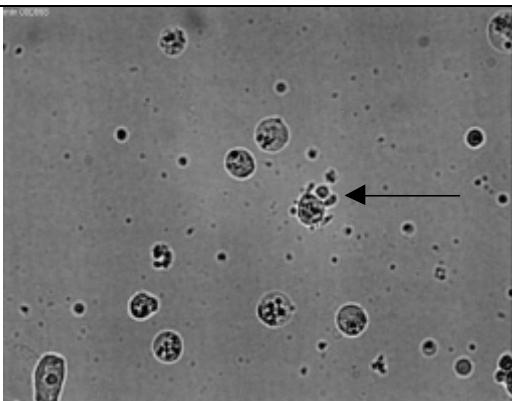
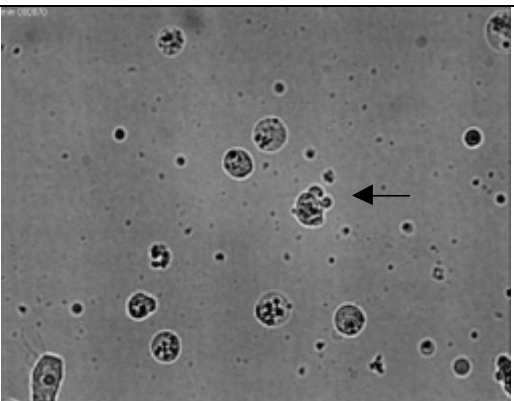
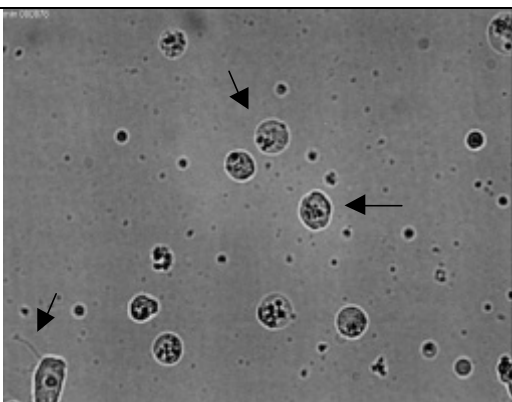
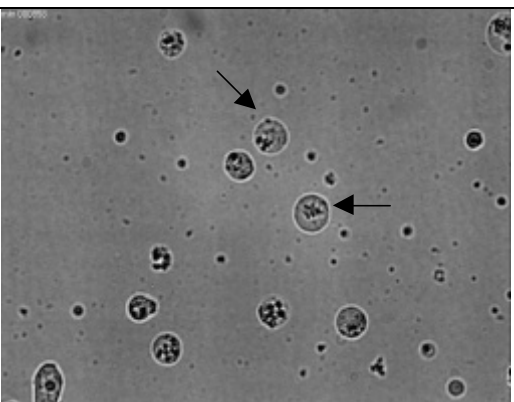
The automated microscope offers the opportunity to create time-resolved scans at one position of the flow-through chamber as previously described in chapter 4.2. These scans can be processed further to generate video-sequences with one or several focal planes lying on top of each other.

An example of a video sequence of only one focal plane (SnapScan single bright field plane mode), taken with the automated microscopy system, can be seen in Tab. 5-1. It shows images of a sample observed at one position in the flow-through chamber. In this example a hybridoma cell line was used that was cultivated in a small scale 10 L bioreactor. At the end of the exponential growth phase a sample was taken and loaded into the flow-through-chamber.

At the beginning of the sequence (0 min) all cells are spherical and of equal size. It has to be mentioned that the images shown can convey only an incomplete impression of the morphological changes, but the original video sequence proves that the membrane is full of motion and not stiff and motionless as it appears in the images at the beginning of the observation. For the first 298 min the phenomenon of highly flexible membrane structures could be observed in all cells, but after 304 min the first cell shows heavy distortions on its surface. A few minutes later the cell collapses and several new membrane covered vesicles arise (time span 304-308). Over the next 200 min all ejected vesicles are further attached to the remaining cell body, but after 564 min a fusion process starts during which all vesicles melt again to a new membrane covered spherical object with the same dimensions as the original cell. Moreover, the newly arisen membrane covered object has a structure and shape similar to the living mother cell more than 576 min before. It could be observed that all cells undergo this kind of morphological change.

**Tab. 5-1** Parts of a video sequence (SnapScan mode – only bright field focal plane) of Hybridoma SP2/0 cells observed in the flow-through chamber at a single position over 960 min. Time 0 min: Start of the video-sequence. Time 298 min: First cells show heavily membrane distortions. Time 304-308 min: First cell collapses, new vesicles arise. Time 332 min: Vesicles are further attached to the mother cell body. Time 564 min: refusion process begins, second cell starts with ejection of vesicles. Time 564-568 min: Four minutes after the Refusion Process began all vesicles were melted again with the mother cell body and an object of the same size and shape appears that looks similar to the original cell 618 min before.



Time		Time	
566		568	
576		618	
868		870	
878		958	

### 5.2.2. Two focal plane SnapScan

The overlay of several image planes and the presentation as an RGB color image allows the representation of more information in one image than it would be possible if only one image plane were observed. As an example a SnapScan is shown in which two focal planes at one position of the flow-through chamber were observed, the normal bright-field image plane and the fluorescent image plane.

To realize this kind of SnapScan the vis-light source was switched on and off, in between the changes of images planes and the shutter system that controls the uv-light path was only opened when necessary (see material and methods, 4.2.2). This technique prevents the observed specimen from any bleaching caused by too long exposure to uv-light. Both image sequences were stored on hard disk and after all images were taken they were further processed. During processing each image was used as source for a separate RGB channel of an 8-bit color image. The red color channel represents the bright field image plane whereas the green color channel was occupied by the images of the fluorescent image plane. The blue color channel was not used in this case. Also, a time index was added to each image and then all images were saved in a mutual RGB color image sequence. The sequence was converted into Microsoft Windows video format "avi" by a public domain program and can, therefore, be viewed easily with any conventional media player on any computer.

Tab. 5-2 shows the same Sp 2/0 hybridoma cells as they were used in the chapter 5.2.1. At the beginning of the video sequence the images of SnapScan in Tab. 5-2 show almost only spherical cells and some cell debris that are spread over the entire image visible as small dark particles. Only one small fluorescent object can be seen from the beginning, but it is too small for an entire cell and thus, based probably on a membrane-covered vesicle that includes DNA that results from a burst cell. As an example, an image of this is shown in Tab. 5-2 at  $t=85$  min after start of the sequence (the arrow marks the fluorescent object). At 140 min it can be seen that the dye was now able to penetrate the cell membranes of different cells and stains the dsDNA within the nucleus. Over the next 70 min the fluorescent signal increases and reaches a maximum ca. 260 min after the start of the SnapScan. After 264 min every cell is stained by the dye.

Of special interest in the present video sequence is the change of the morphology of one cell that is centered in the middle of images of the SnapScan (marked with an arrow at time 256 min). During the first 160 minutes this cell shows an active membrane which is highly flexible

and shows strong motion on its membrane surface. After 160 min the membrane becomes irregular, perturbations arise and several bulges appear and disappear on the membrane surface. After 195 min the flexibility of the membrane decreased abruptly and also any motion of the membrane stopped. DAPI slowly penetrated into the cell and the cell began to swell. In the following 40 minutes the fluorescence signal increased and reached a temporary maximum at 256 min. Two minutes later it can clearly be seen that the cytoplasmic membrane has collapsed and, at the same time, the fluorescence signal strongly increases again.

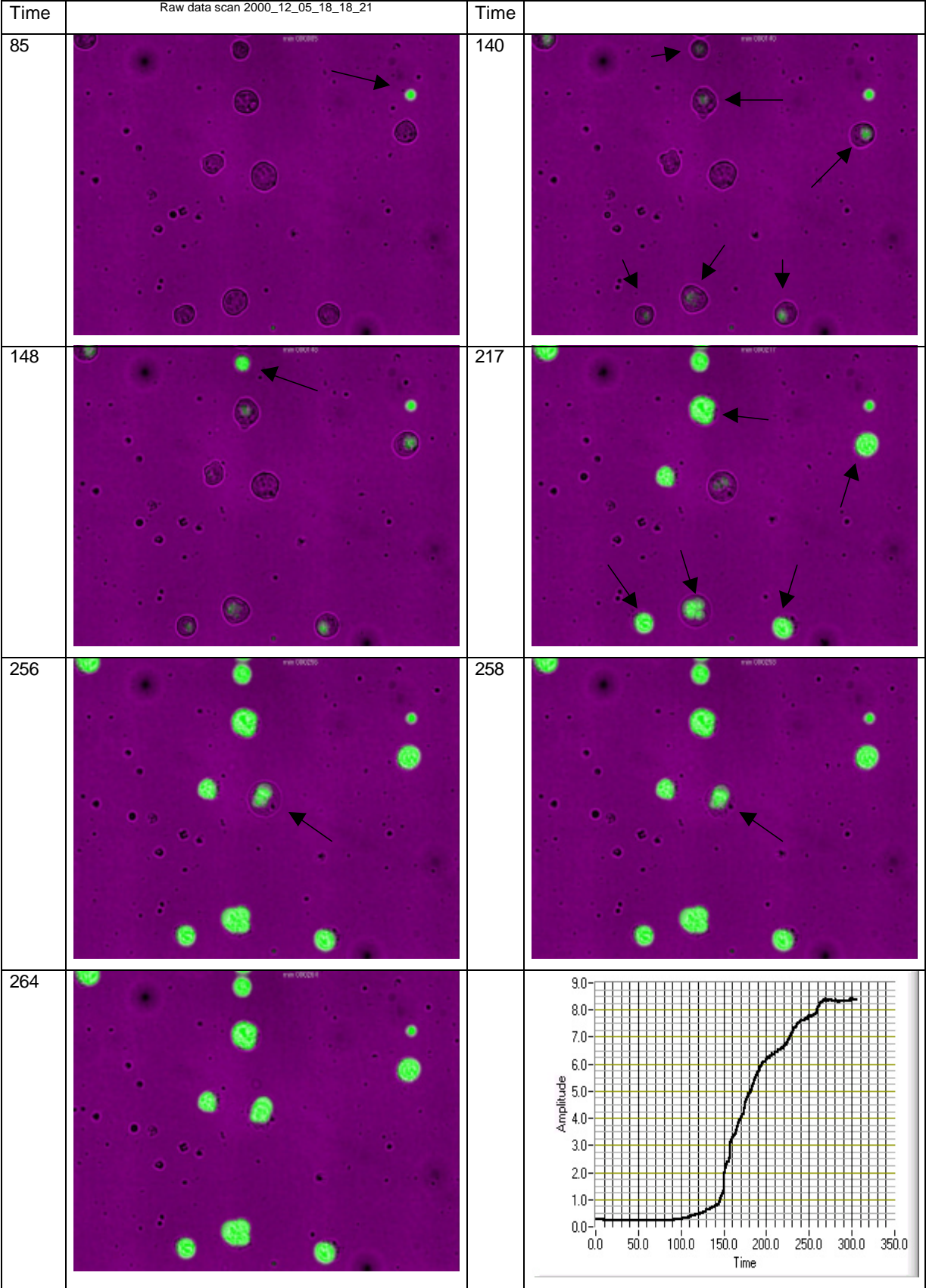
The video sequence shown is good evidence for the ability of DAPI to penetrate the cell membranes in an early phase but there is still a diffusion resistance present that does not disappear until the membrane collapses as can be shown in the video sequence.

Additionally to the qualitative evaluation of the video sequences a simple quantitative analysis of the fluorescent events was performed by calculating the average of all pixels of the images of the fluorescence image plane:

$$\text{amplitude} = \frac{1}{n} \sum_n G(n); G = \text{graylevel}, n = \text{number of pixels}$$

The quantitative representation gives a better insight into the dynamics of staining processes and also allows the comparison of different SnapScans simply by using diagrams. Tab. 5-2 contains, additionally to the images of the SnapScan, a diagram that shows the increase of the fluorescence signal over the time and, therefore, gives a valuable overview about the course of the signal. As also can be seen in the images and in the diagram the fluorescence signal increases drastically after 150 min and reaches a maximum at 260 min. The course of the fluorescence signal itself is approximately sigmoid, which corresponds to the result of a typical staining procedure. However, the course of the function is rough because of the few cells in the image, therefore, each single event in which the stain penetrates into a cell causes an irregularity. If there were more cells in the image the course of the function would be smoother because more staining processes would run in parallel, started at different times and more single staining events would be interlaced with others.

**Tab. 5-2 Selection of images from a two-focal-plane SnapScan of a Hybridoma SP 2/0 cell line. The images show two different focal planes, one bright-field illuminated and the second illuminated with uv-light.**



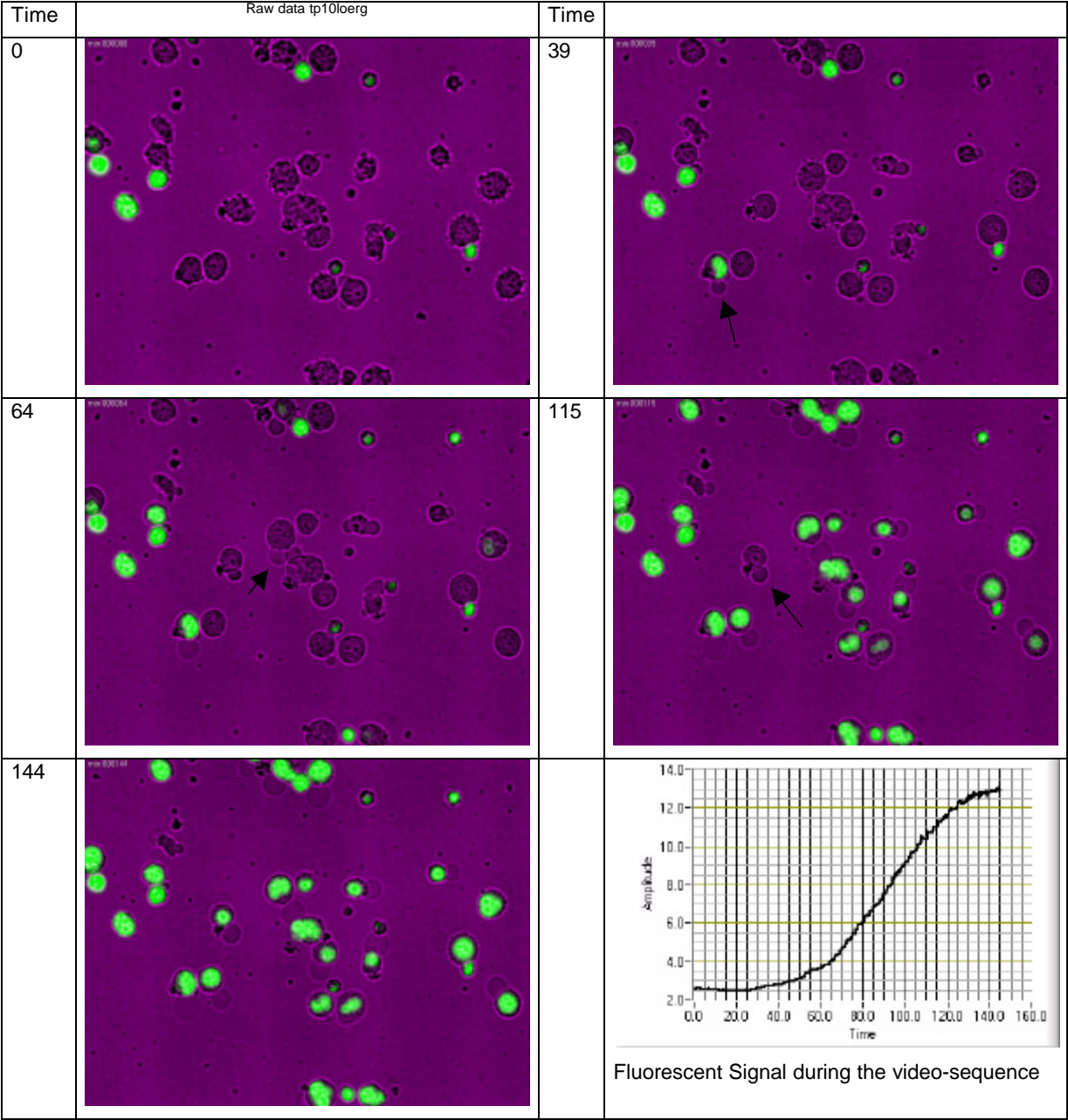
### 5.2.3. Blebbing and Dying of Cells – Two focal plane SnapScan

Another example of a staining process is shown in Tab. 5-3. In this case CHO cells taken from the stationary phase of a fed-batch bioreactor run were observed. Tab. 5-3 shows several images as examples of the SnapScan and also a diagram that should give an impression of the quantitative course of the increasing fluorescence during the SnapScan. It already becomes obvious at the start of the SnapScan that the morphology of the cells is rather different from those in the example with the SP 2/0 hybridoma cells shown before. The range of different cells shown here is far greater with regard to size and shape. The membrane of most of the cells is rough, distorted and covered with papillae and some cells were already stained completely by DAPI from the beginning

After 40 min the dye began to penetrate into the majority of the cells and 100 minutes later all cells had completely absorbed the fluorescence dye. During this uptake process the cells showed a change in their morphology. At the start of the SnapScan most cells showed papillae on their surface, but during the staining process exactly at the moment when the cytoplasm oozed out of the cell and formed a bleb, all papillae disappeared. Intact cells can be considered as incompressible drops of liquid covered with an elastic cell membrane. A positive pressure acts from inside the cell on the membrane that corresponds to the turgor pressure of the cell. It seems, that once a hole is formed in the membrane, the turgor pressure of the cells pushes the cytoplasm out and simultaneously the pressure decreases and the papillae collapse. The staining of the nucleus starts either in parallel or shortly after the bleb arises.

In comparison with the SnapScan of the Sp 2/0 hybridoma cells previously shown, the time interval until the majority of cells were stained is clearly shorter with the CHO cells used in this case.

**Tab. 5-3 A two-focal plane time-resolved SnapScan of dying CHO cells with strong blebbing effects over a time of 144 min. The diagram in the bottom left corner shows the course of the raising fluorescence signal over the time.**



### **5.3. Analysis of FullScans**

#### 5.3.1. Refractive activity and fluorescent events

While SnapScans were predominantly used to clarify more basic questions, FullScans were used for routine supervision of mammalian cells during cultivation.

Before examples of the cultivation of different mammalian cell lines are shown, some more basic results will be given in this chapter. A small part of an entire FullScan, an image set of three images is shown in Fig. 5-6. The images were taken from the first of 100 positions of a scanned flow-through chamber and show CHO-cells at the beginning of the production phase of a monoclonal antibody production. Additionally to the images, three 3D surface plots are shown that represent the same image information as the original images, but enable a quantification of the gray-levels and give a better insight into the distribution of pixels.

Each image plane shown in Fig. 5-6 contains mainly additional information for the characterization the physiological state of the cells, but some information in the images is also partially redundant. For example, most of the objects of the “nearly in focus” image can also be found as refractive active objects in the out-of-focus image. Merely, the capability of light refraction of the objects depends on their geometrical shape and their optical consistence. Fig. 5-7 serves as a very simplified model to explain the optical differences of an “intact” suspension cell and a physiologically and morphologically disordered cell. A normal spherical cell refracts light, as a thick lens would do. Entering light is refracted to a focal point, or more precisely, to a focal plane (catacaustic). If the focal plane of the microscope objective is focussed on this focal plane of the cells, all cells arise as bright shining spots. The brightness, size and shape of the spots are dependent on the three-dimensional structure, the state of the intracellular components and the membrane structure of the cells. Disordered cells that have a damaged membrane, have entered into the apoptotic pathway or have become necrotic, are not able to focus the entered light in the same way as spherical cells and generate a weaker signal (Fig. 5-7, cell on the right).

A redundancy exists between the out-of-focus image and the fluorescence image, because the weakest shining objects, in terms of refractive activity, can also be detected as fluorescent spots in the fluorescence image. A reciprocal relation seems to exist between the refractive activity of a detected object and the membrane permeability that is crucial for interaction of dye and DNA. The more diffuse the spots in the out-of-focus image plane

---

appear with darker gray-levels in the spot center, the more likely is it that the membrane of these objects has become permeable for the DNA dye DAPI. The arrows in the top right image of Fig. 1-1 point out all cells that show a weak refractive activity and also fluoresce.

The 3D plots in Fig. 5-6 show the entire dynamic range of each image plane. It can be seen that the “out of focus” image as well as the “nearly in focus image” has a strong plateau at around 100 of the 0 to 255 gray-level scale. These plateaus mainly consist of pixels belonging to the background. In contrast to this, the most significant pixels, containing the object information, lie in regions over and beneath the plateau (peaks in the plots). Hence it follows that any applied algorithm should be able to separate the object information from the background plateau. In contrast to both image planes in which the background planes lie in the middle of the gray-level range, the background plane of the fluorescence in-focus image plane is zero because only stained objects are able to fluoresce. This fact simplifies image analysis extraordinarily because every pixel with a value greater than zero is object information. Therefore, the entire dynamic range of the fluorescence images contains object information.

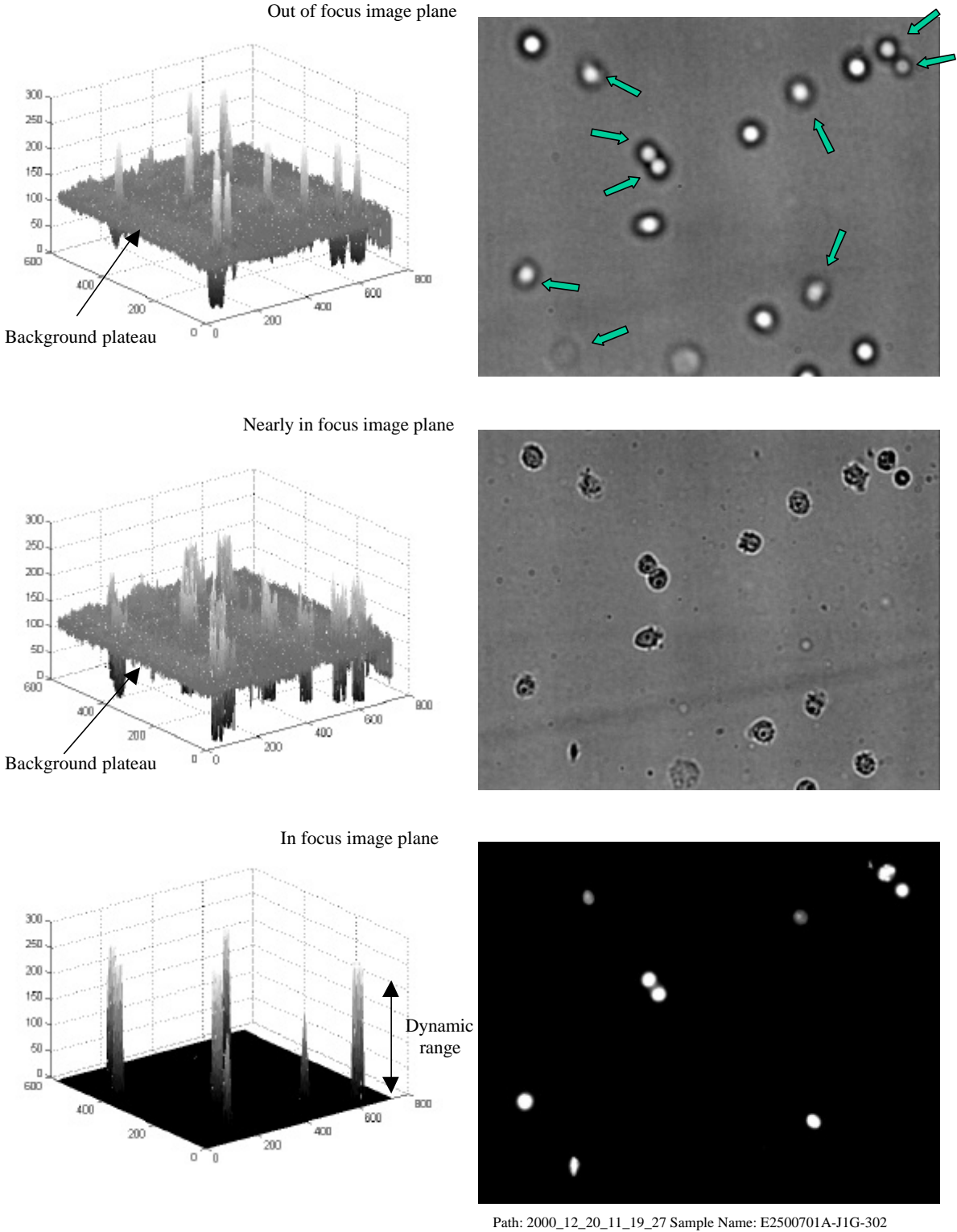


**Fig. 5-6 One of hundred Images of a FullScan: Each the of three images on the right shows one of the three image planes taken at the first position of a scanned flow-through chamber. The arrows in the out of focus image mark cells which also fluoresce.**

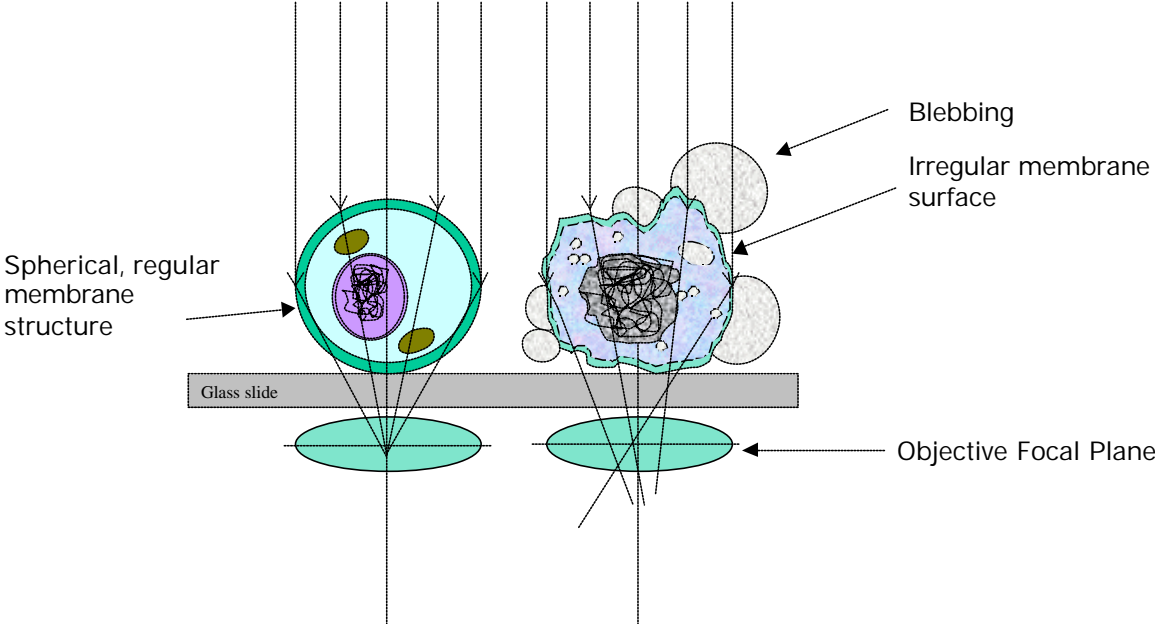


**Fig. 5-7 Light refraction of an intact cell (left) and disordered cell (right). The intact cell shows a regular membrane surface, which acts as thick lens, and focuses the light in one image plane. In the disordered cell the membrane is irregular resulting also in a irregular refraction of light.**

#### **5.4. Automated determination of cell number and viability in comparison with classical trypan-blue hemocytometer measurements**

To test the suitability of the developed AMS to describe changes of cell number and viability during mammalian cell culture the system was used for the observation of different CHO and hybridoma cells during biopharmaceutical production of antibodies and other complex glycoproteins. In all cultivations performed, the cell concentration were routinely determined by using a hemocytometer and the trypan-blue exclusion method. From each manually counted sample a FullScan was also taken and analyzed by the image processing algorithms described in chapter 4.3. For the determination of the cell number only two of the three image planes of a FullScan were analyzed, the “out of focus” and the “in focus” image plane. Additionally glucose, lactate concentrations and the product titer were determined. All Information was stored in databases as described in chapter 4.1.

##### **5.4.1. Fed-Batch CHO cultivation**

As a first example a comparison of the results of two fed-batch CHO cultivations is shown in Fig. 5-8, both carried out in two 10L bioreactors. Both reactor runs were started as batch cultivations for 3 days and filled up afterwards with media to their end volume. During the production phase both reactors were fed three times with a concentrated feed solution that contained glucose and a selection of essential nutrients, lipids and amino acids.

Fig. 5-8(a) shows the number of viable cells of both runs determined by the trypan blue exclusion method, and the number of refractive active objects counted automatically by analyzing the “out of focus” image plane of the FullScans taken. In addition to the cell concentration the product titers of both reactor runs are also shown in Fig. 5-8(a).

It can be seen that it is possible with both methods (manual and automatic) to describe the changes of the cell number during cultivation, and that the number of refractive active objects is comparable to the number of viable cells determined by hand. However, in the comparison of both runs it can also be seen that the number of refractive active objects of reactor 2 fits the manual counted results of the same run much better than in case of reactor run 1. Here the number of refractive active objects is lower than the manually counted cells.

Generally the results are comparable and both give similar results in describing the course of both cultivations, but there are differences in the absolute cell numbers especially in reactor run 1.

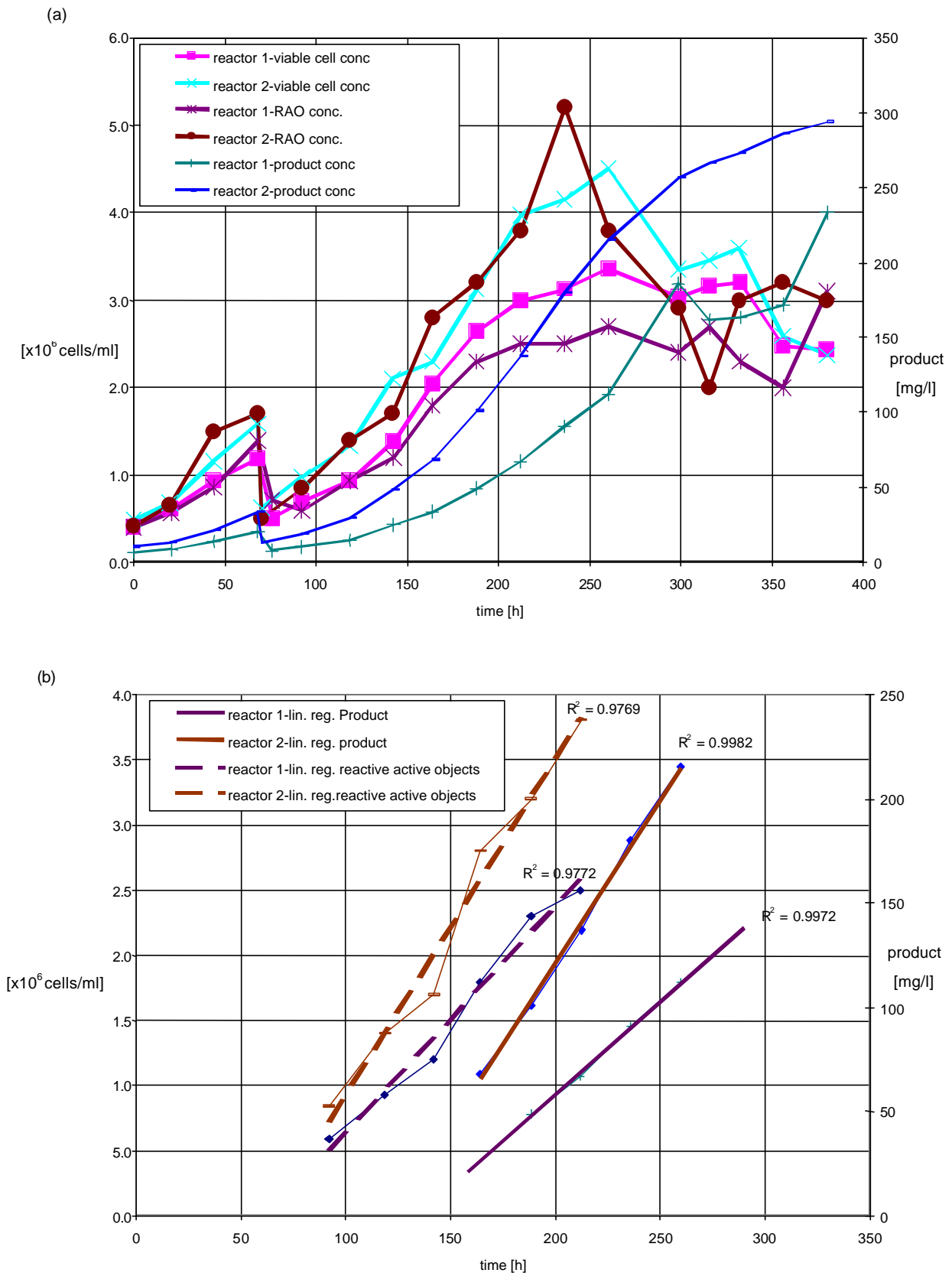


**Fig. 5-8 Two CHO cultivation bioreactor runs: Comparison of measurements of viable cells manually counted by using the trypan-blue exclusion method and automated determination of the number of refractiveactive objects**

During cultivation in batch or fed-batch mode the growth of cells only follows a first order reaction during the first four to five days as long as no limitation occurs. The most cultivations carried out in this work and several cultivations that can be looked up in various publications show an almost linear growth phase which followed the exponential growth phase of a batch or fed-batch cultivation [Barnes, Bentley and Dickson, 2001], [Sauer *et al.*, 2000], [Zanghi, Fussenegger and Bailey, 1999], [Seifert and Phillips, 1999], [Dutton, Scharer and Moo-Young, 1998], [Kenn and Rapson, 1995]. In Fig. 5-9 the theoretical course of a mammalian batch or fed-batch cultivation is shown. At the beginning of the cultivation the cells have to overcome the difficulties of adaption to the reactor conditions but when the cells enter the exponential growth phase that can be simply described by a first order reaction. However, in the subsequent course of the cultivation when nutrients are exhausted or toxic byproducts are accumulated growth is slowed down. The cells leave the exponential growth phase and it seems for a short period of time as if the growth becomes linear while the kinetics change and the inhibitory terms increase. After a transition phase the cells enter the stationary phase and growth stops.

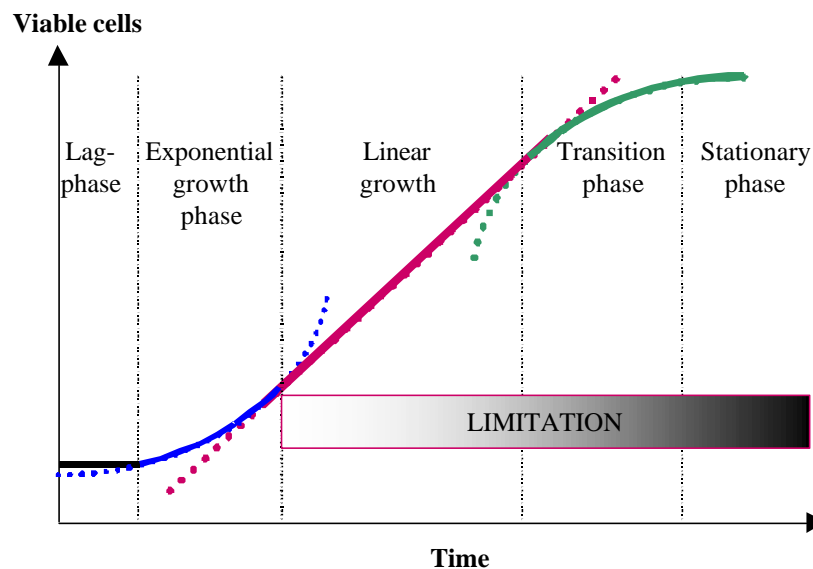


**Fig. 5-9 Model of the course of the viable cell concentration during the first phases of a batch or fed-batch cultivation: Only at the beginning of the cultivation after a lag-phase cells grow exponentially, after limitation, the growth kinetic changes and can now be approximated by a straight line. With exhausting of nutrients or accumulation of toxic byproducts growth stops and the culture enters the stationary phase. Dotted lines symbolize when a simple first order growth or die kinetics cannot fit the further course of the growth function.**

Fig. 5-8(b) shows the almost linear part of Fig. 5-8(a) magnified with trend lines showing the gradients of the growth function. It also shows product formation around the turning point of the curves when the culture is running into limitation and growth kinetics change. It can be seen that the gradients of the growth and the gradient of product formation for reactor 2 and very similar for reactor 1 during the change of the growth kinetic are equal.

#### 5.4.2. Fed-Batch cultivation with temperature shift

In a second example, the course of a biopharmaceutical production with CHO cells producing a monoclonal antibody was performed. Fig. 5-10 shows again the results of two parallel bioreactor cultivations as in the example before. The first graph of Fig. 5-10(a) shows both the manually counted hemocytometer results of both bioreactors during the cultivation and the results of the FullScan analysis of the automated microscopy system. For FullScan analysis only the results of the “out of focus” refraction image plane and the fluorescence image plane were evaluated. The diagrams Fig. 5-10(b) and Fig. 5-10(c) give additional information about the process, e.g. glucose consumption, accumulation of lactate, titer of the antibody and the temperature of the fermentation broth during cultivation. The process was carried out as fed-batch cultivation in which a production over several steps with increasing reactor volumes was simulated in only a single 10 L bioreactor. Over the first 150 h of the cultivation the CHO culture passed through three exponential growth phases. After each a part of the fermentation broth was drained off and a volume of 2 L was retained. After 150 h the actual production phase began. Two days after entering the production phase, a feed solution was given and the cultivation temperature was shifted down from 37°C to 33 °C.

It could be seen that during the three simulated volume expansion steps before the beginning of the production phase the manually hemocytometer results were very similar to the cell counts generated by the AMS. However, the automatically generated results were generally a bit lower than the cell counts determined by hand. Over the first two days of the production phase, the results of both cultivations regarding the automated analysis were equal but after the third day of the production phase (marked by the dashed vertical line in the diagrams) the results started to differ. In contrast, the manually determined cell concentrations of both reactor runs were equal during the entire exponential growth phase. Only when the stationary phase was reached, did the manual counting results differed from each other.

If an operator had only known the manually counted results he would have assumed that both reactor runs in the exponential growth phase of the production period were equal and

he would also expect that the product titer of both runs might be similar at the end of the cultivation.

The dotted lines in Fig. 5-10(a) symbolize this and show the gradients of growth determined during the production phase. It emphasizes the fact that the manually determined gradients are equal, but the automatic determination results in two significantly different gradients.

In contrast to the automatically determined results, the manually counted cell numbers do not fit to any of the other results e.g. the product titer and the lactate accumulation shown in the diagrams Fig. 5-10(b) and Fig. 5-10(c). These results show that both runs are completely different. Although the manual counts of both reactor runs were equal, the course of product formation during cultivation was not, as it would have been expected if only the manual counts had been considered. The estimation of an equal product titer at the end of the cultivation failed because reactor 2 reached only half of the titer of reactor 1.

In contrast to the manually counted cell numbers, the automatically generated cell counts lead to the supposition that the behavior of both runs were completely different after the third day of the production period was reached. This could be confirmed by the course of the titer formation as well by the lactate accumulation. So only the automatically measured cell counts give a hint that both reactor runs were not equal in the exponential growth phase of the production period.

In Fig. 5-11(a) the different cell counting measurements and the product titer are shown. As in the example before, trend lines of the gradient were added to point out the similarity of gradients of the cell growth and the product formation. The gradients of the number of refractive active objects and the product titer, of the same reactor run, are very similar Fig. 5-11(b). This phenomenon could be observed in numerous cultivations in which the growth was measured by determination of the number of refractive active objects with the automated microscope (data not shown). Thus, a determination of gradient of the number of refractive active objects offers the possibility to estimate the maximal product titer, already during the exponential growth phase.

Furthermore, the number of refractive active objects reflects the downshift of the temperature after 190 hours and points out a change of the growth kinetics, while the manually determined results do not reflect this event. Therefore, two different gradients can be seen during the production phase of the cells.

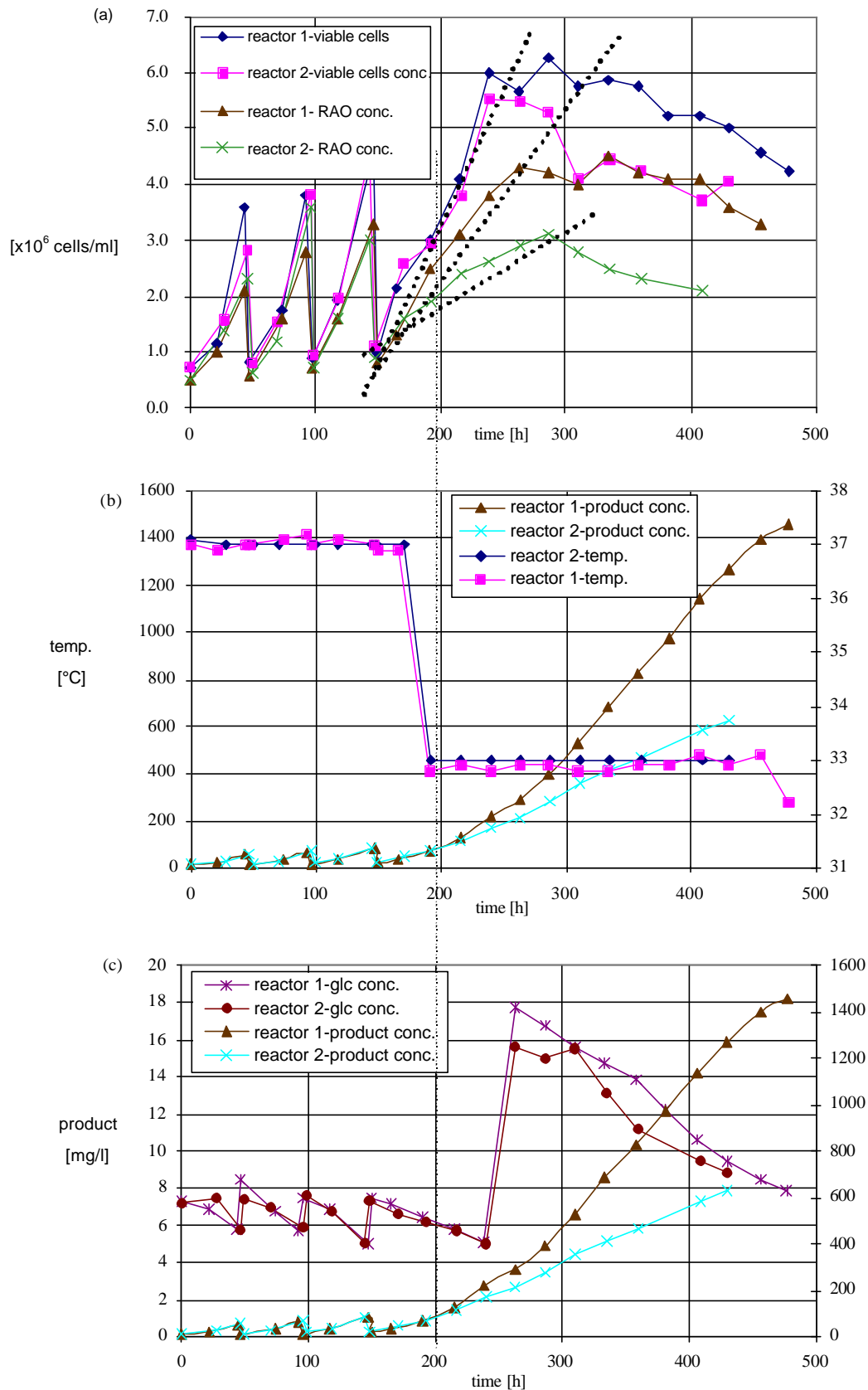


**Fig. 5-10 Comparison of cell number, glucose and product concentration of two CHO cells 10 L bioreactor cultivations.**

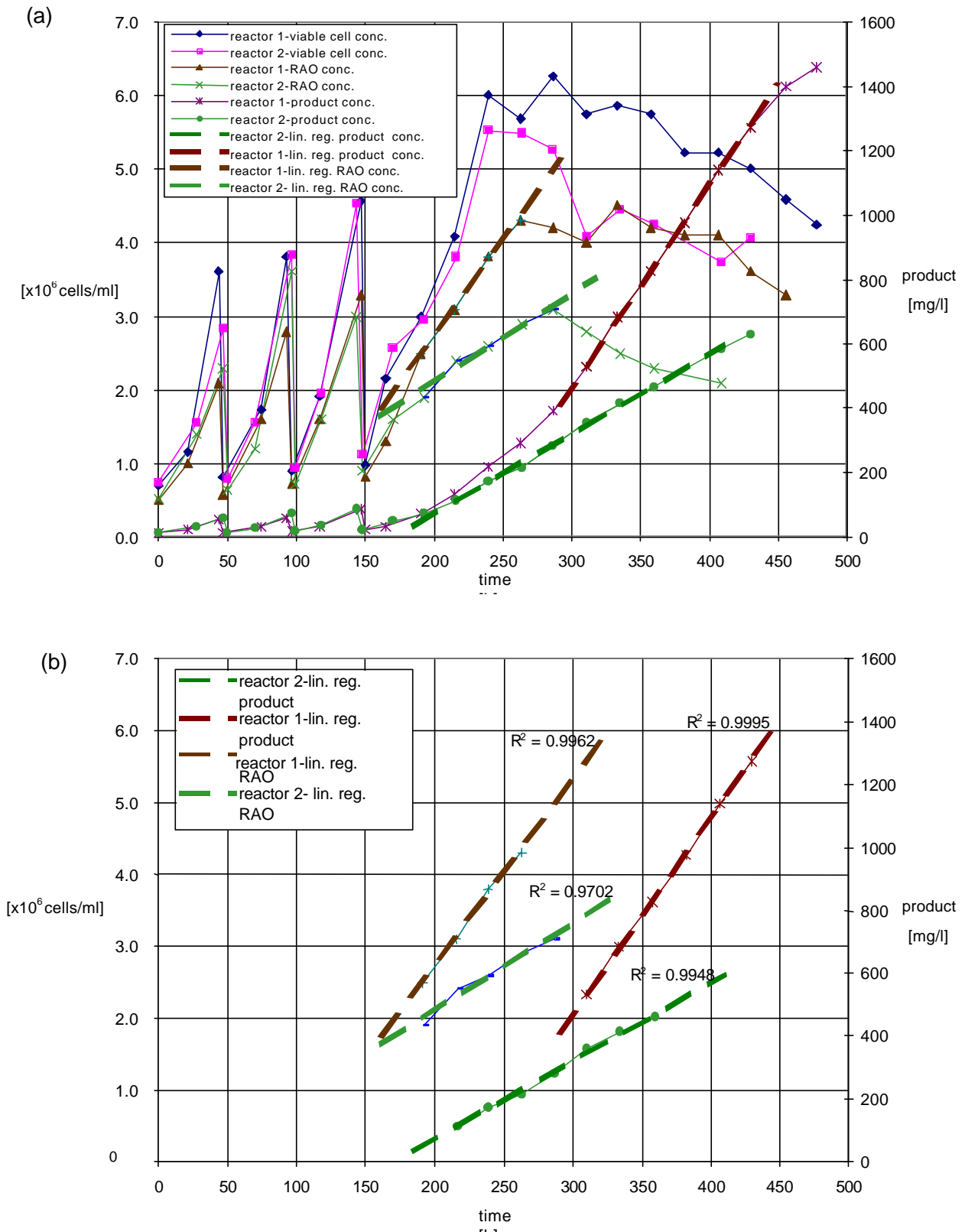


**Fig. 5-11 Comparison of gradients (number refractive active objects & product) during exponential growth phase of the two CHO bioreactor cultivations described in Fig. 5-10.**

### 5.4.3. Fed-Batch Hybridoma cultivation

The hybridoma cultivation described here serves as an example to demonstrate the high conformity in the number of viable cells and the number of refractive active objects Fig. 5-12(a). Moreover, it shows some of the difficulties a human observer can have, when he has to distinguish between viable cells, cell debris and dead cells. It also shows that it is possible to calculate the total cell number by addition of the number of refractive active objects and the counted fluorescent events of the fluorescence image plane and that this function correlates with the total cell number determined by hand. In contrast to the CHO cultivations shown before, it was not possible in this case to determine a correct slope of the viable cell concentration by determining a transition phase or defining a point of inflexion. Because of the short growth phase with too few data points a reliable calculation of the slope was impossible. Surprisingly, a similarity exists between the slope of the automatically determined total cell number and the slope of product formation during the transition from the exponential growth to the limitation phase Fig. 5-12(c).

The viability determined by both methods is also shown in Fig. 5-12(b) and looks to be very similar, but the automatically based one is more sensitive because of the better capability of the “in focus” algorithm to detect dead cells. This can be explained with a higher contrast of the used fluorescence dye that increases the sensitivity of the detection.

During the course of the cultivation copious amounts of cell debris were generated and interfered with the cell counting. As an example for that, an original bright field image of a FullScan taken 120h after the start of cultivation gives an impression of the different objects in the cultivation broth and the difficulty to distinguish between them (Fig. 5-13(a)). Because of the dense structure of some of the objects a differentiation between viable and dead cells by the trypan blue exclusion method can be extremely difficult and thus this staining procedure is often not sufficient. Thus it can be very difficult to assign the individual objects to different classes by hand. Fig. 5-13(b) shows an overlay of the bright-field image in Fig. 5-13(a) with the refraction image belonging to it. The additional information of the refraction image allows an identification of the refractive active objects and subsequently a determination of the number of viable cells using the “out of focus” algorithm. The result of the image analysis is shown in Fig. 5-14(a). With only the bright field image plane and a manual trypan blue staining that deteriorates in dense cell structures, an error-free determination of the number of viable cells would be almost impossible. The exceptional performance of the automatic determination can be seen in Fig. 5-14(b). The bright field image, the analyzed refraction image and the fluorescence image are laid on top of each

other. The out of focus algorithm has detected 16 refractive active objects as viable cells. The size of diameter of the circles that marks the separated objects also serves as measurement of the strength of refraction of each individual object. It can be seen that most objects identified by the algorithm are viable cells not penetrated by DAPI. Only four objects that fluoresce were counted as viable cells. In these objects the refraction was still too strong, so these objects were counted twice, once as viable cells and once as dead or fluorescent cells.

The objects #14 and #15 in Fig. 5-14(c) show the capability of the “out of focus” algorithm to also separate objects lying very close together. All objects that are refractively active, focus the light on circular spots that appear smaller in size than the original objects and therefore, can be easily separated by the algorithm.

#### 5.4.4. Conclusion

All three cultivations observed show that it is possible with the developed AMS to describe the course of a cultivation in the same way as using a hemocytometer and the manual trypan blue exclusion method. In comparison with manual counts the automatic determination has several advantages: it is more precise, more reliable and allows additional features e.g. a morphological analysis of the samples. It can be shown that the AMS is able to differentiate between different growth phases of fed-batch cultivations after downshift of the temperature, which is often missed by manual observations (see chapter 5.4.2). In addition the detection of viability is more sensitive, which can be explained by the higher contrast of the fluorescence images.

All results that have been shown in this chapter are based on the analysis of only two of the three image planes of a FullScan. The potential of a morphological analysis of the third image plane has not been utilized so far, but would allow the isolation of enormously more cell population specific parameters that could never be achieved manually (see chapter 5.6).

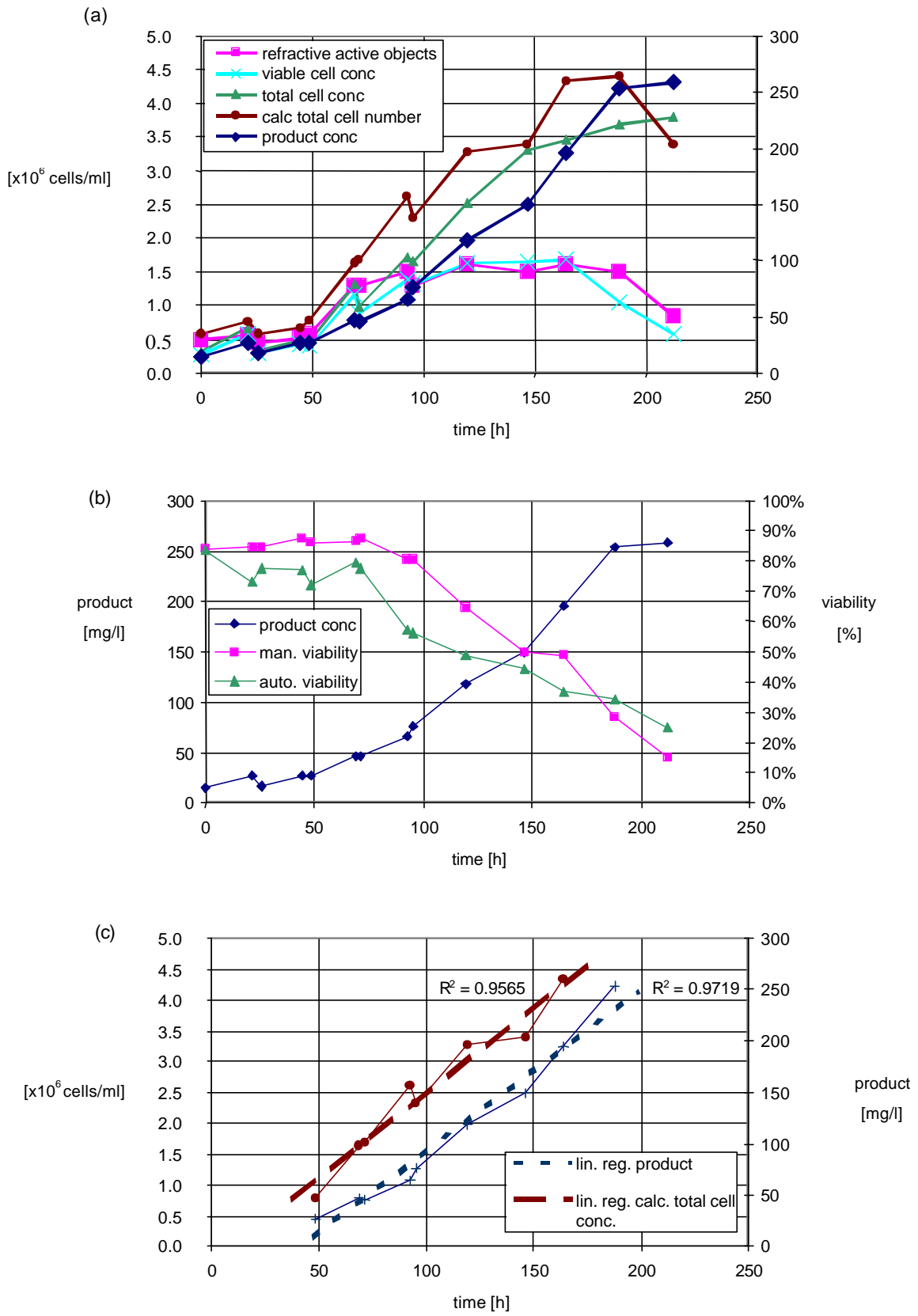
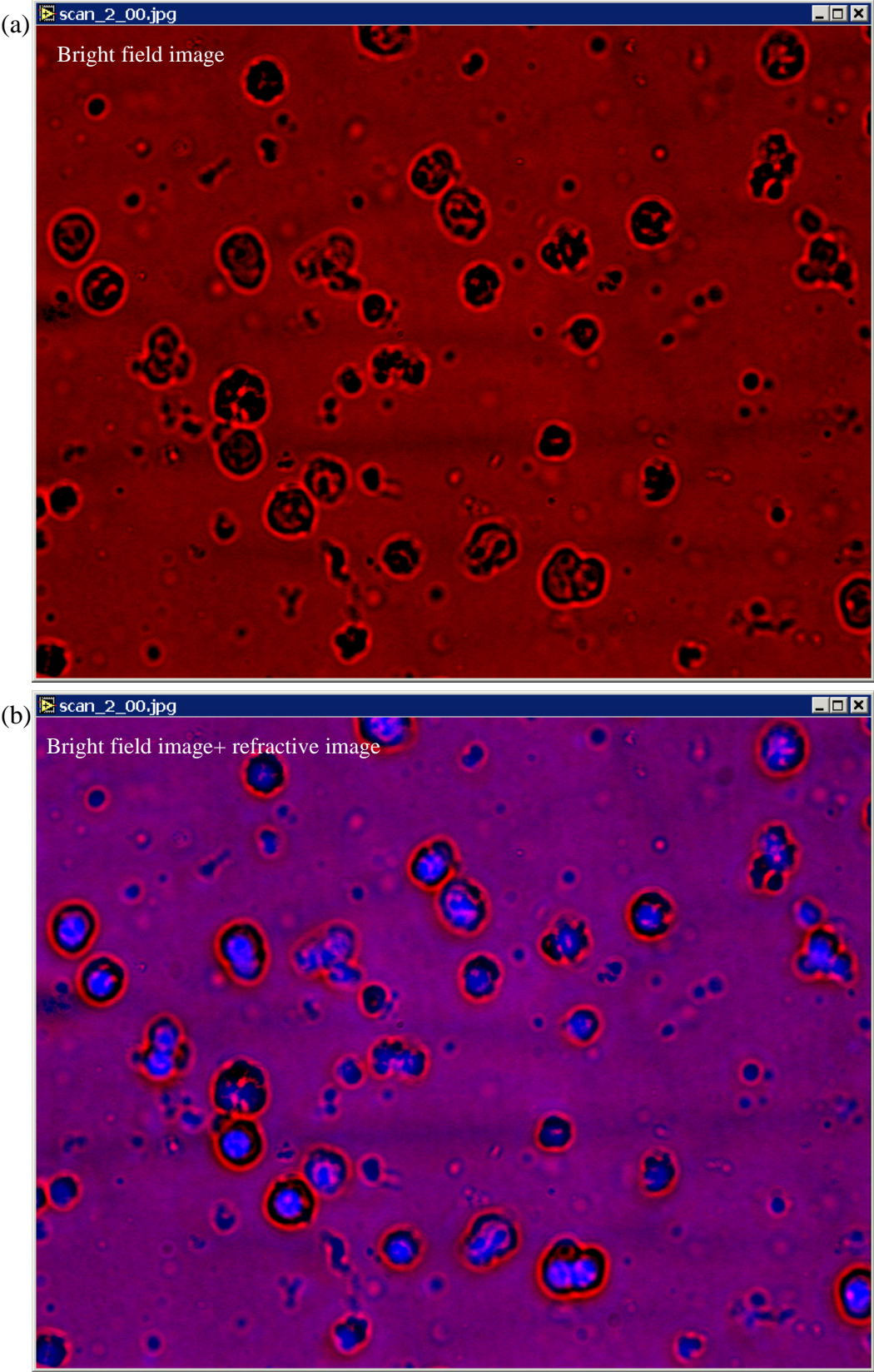


**Fig. 5-12 Comparison of manually determined total cell numbers and calculated total cell numbers based on addition of refractive active objects and fluorescent events.**



2001\_01\_28\_13\_26\_31

**Fig. 5-13 Part of a FullScan of the hybridoma cell cultivation: original bright field image and bright field image overlaid with refraction image**

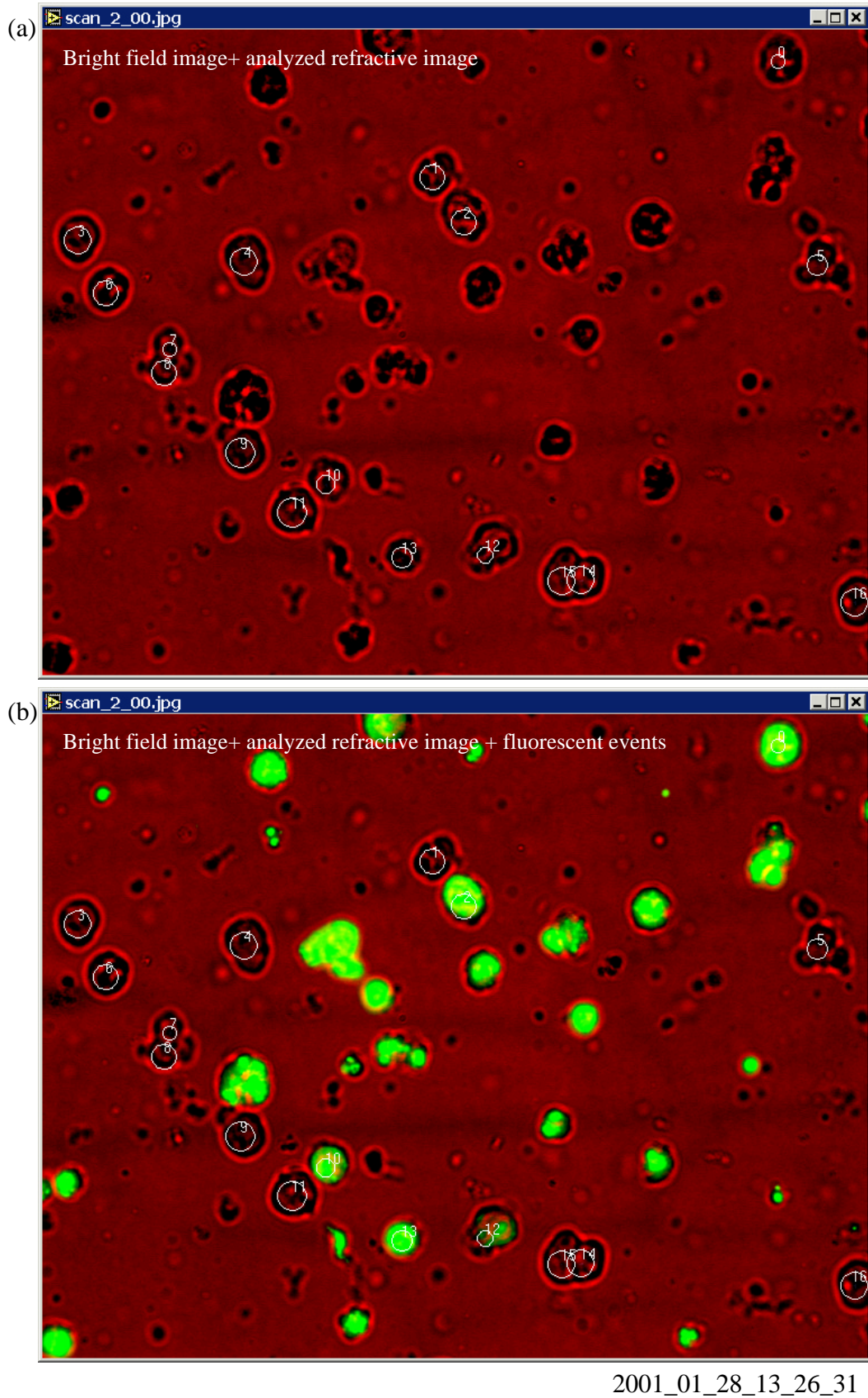


**Fig. 5-14 Results of analysis: (a) Bright field image overlaid with the analysis of the refractive image and additionally overlaid with the fluorescence image (b)**

### 5.5. Linearity of FullScan measurements

To test the linearity of the microscopy system and to determine the range of concentration, in which the system works reliably, the system was tested with different cell concentrations. For the test Sp2/0 hybridoma cells were chosen but the same results were also obtained with a CHO cell line (data not shown). The cells were first concentrated by centrifugation and then diluted in several steps. Each dilution step was measured three times by the AMS.

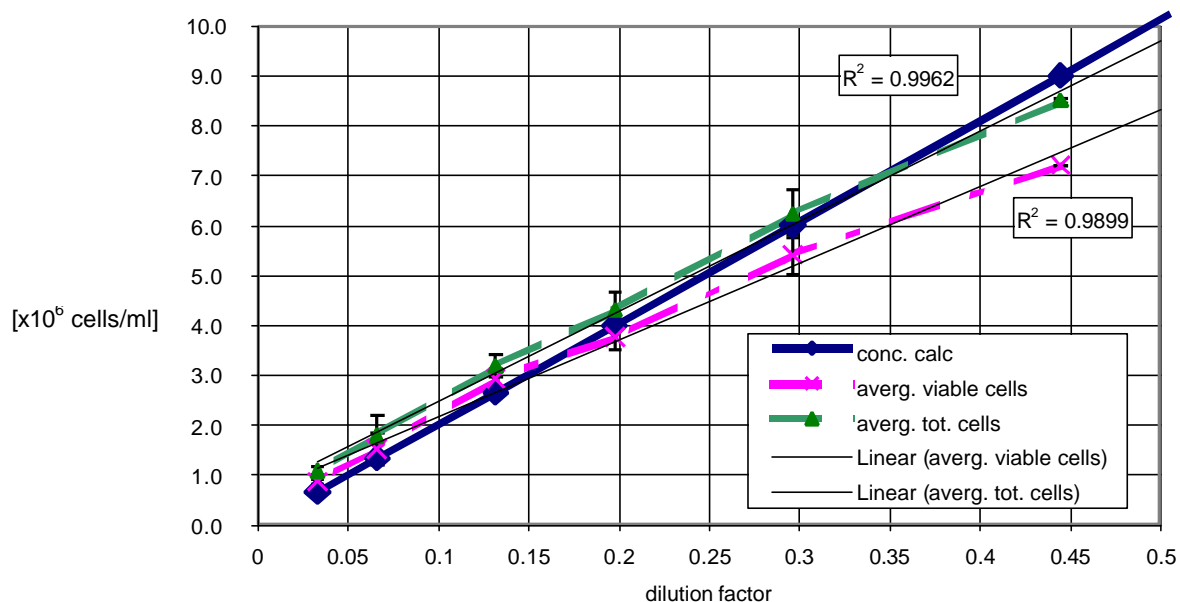
The cells were cultivated in a bioreactor up to a concentration of  $1 \cdot 10^6$  cells/ml. After sampling, the cells were concentrated tenfold by centrifugation, and then diluted in several steps to a concentration down of  $5 \cdot 10^5$  cells/ml. Three FullScans were taken of each dilution step to ensure a better statistical certainty and to assess the statistical error.

Fig. 5-15 shows the results of the experiment. The solid curve in the diagram represents the calculated concentration levels starting at a concentration of  $9 \cdot 10^6$  cells/ml. The levels were calculated on the basis of a hemocytometer cell counting before the centrifugation step had been performed, assuming linear concentration and dilution steps. The dashed-dotted curve shows the results of the automatic cell counting generated by analysis of only the “out-of focus” image planes (each data-point represents the average of three FullScan analyses). The algorithm that has been described in chapter 4.3.1 counts refractive active objects only, which gives similar results as when using the trypan-blue exclusion method to determine viable cells. The dashed curve in the diagram shows the automatically measured total cell number generated by addition of the number of automatically counted viable cells and the counted fluorescent events in the in-focus planes of the FullScan, analyzed as described in chapter 4.3.4.

In comparison of all curves it can be seen that both curves measured with the AMS are slightly crooked. This does not appear in the curves that are based on only one hemocytometer measurement. At higher concentrations the counting results measured with the system are not completely linear although the total cell number generated by the system still fits very well to the calculated concentration levels. Because of smaller contrast differences, it is more difficult for the “out of focus” image plane analyzing algorithm to isolate object structures, especially at high cell densities. Therefore, it is possible that the “out of focus” algorithm underestimates the cell concentration more than the fluorescent events counting “in-focus” algorithm. Thus, at higher cell concentrations the difference of the calculated concentrations resulting from the sum of both measurements is smaller. Besides, the viability decreased over the time because of the length of the experiment. Triple

[ $\times 10^6$  cells/ml]

measurements of each concentration level took 50 min, bringing the time for the entire experiment to a total of more than five hours during which the cells were kept in a suboptimal environment.



**Fig. 5-15 Linearity of measurements at different concentration steps**

The database strategy employed offers the possibility to describe the relationship between manual and automatic viable cell concentration counts, independent of experiment the counts were based on. Fig. 5-16 shows the results of more than 200 analyzed FullScans in comparison with the manually counted viable cells. The data are based on 16 different experiments with two different CHO cell lines and one hybridoma cell line.

The results of both methods are very similar over the whole range of concentrations and the relation between automatic and manual cell counts is linear (see dotted line). However, there are also automatic measurements that deviate from the manually determined cell counts. These differences could be due to failures in either the manual or automatic counting, or could be based on the measuring of completely other effects that differ from those that are determined by a manual hemocytometer counting. During the course of the work it has been shown that an automatic counting with the developed system is more accurate than a manually determination of total and viable cell concentration. Moreover, the determination of refractive active objects as viable cells, describes the course of cell cultivation better than a hemocytometer determination could do.

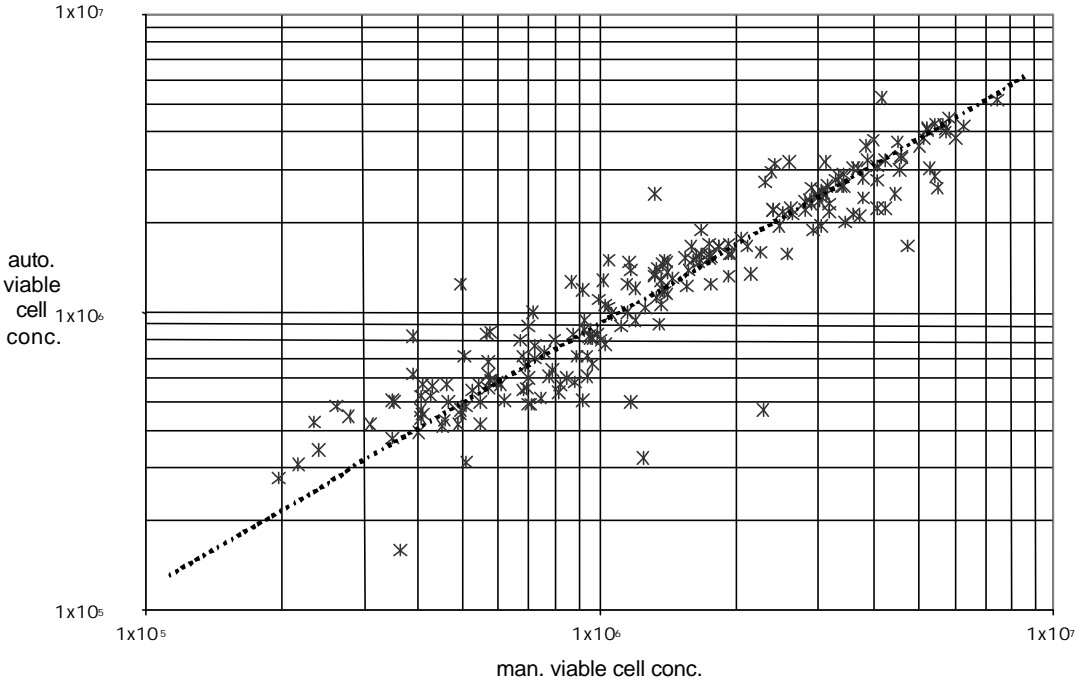


**Fig. 5-16 Comparison of results from more than 200 automatic cell count measurements of more than 10 separate cell cultivations with different mammalian cells (CHO, Hybridoma) lines in comparison with manual cell countings**

## 5.6. Quantified Morphological Changes

Besides the analysis of both “out of focus” and “in focus” image planes, the analysis of the “nearly in focus” image plane of a FullScan allows also a morphological description of the investigated samples. As mentioned in chapter 4.3.3 the algorithm used calculates a large number of morphological parameters and saves all of these parameters in a database. For evaluation of these large amounts of different data a software-tool was developed that allows a fast comparison of these data. The core of the developed tool is a fast graphical visualization surface that allows a data visualization either as bar-graph plots, if only one single parameter needs to be shown, or as a scalable x,y-plot viewer that allows a flexible choice of different parameters of each axis.

A comparison of the data stored in the database has shown that the particle perimeter and its area are two suitable parameters to describe the shape of the investigated object and to quantify its circularity. In a x,y plot with the area as abscissa and the perimeter as ordinate, both parameters result in a diagram in which all data points lie on or over a curve that is proportional to the root of the area. All circular objects lie exactly on the curve as a function of the area only, because the perimeter of a circular object is proportional to the radius squared.

### 5.6.1. Heywood circularity factor

To spread the data points generated by the perimeter and area described before, the perimeter was replaced by the Heywood circularity factor. In contrast to the perimeter, the use of the Heywood circularity factor allows a better separation of data-point cluster and moreover the entire diagram area can be used.

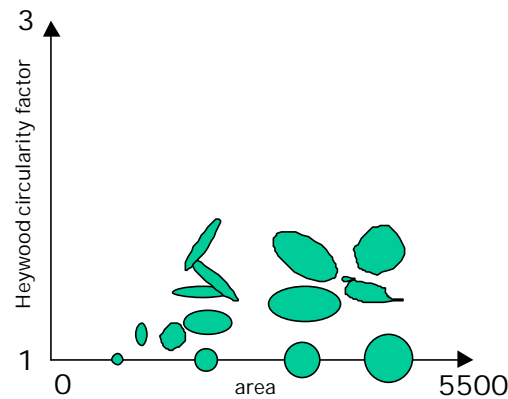
#### Definition of the Heywood circularity factor:

The Heywood circularity factor is the ratio of an object perimeter to the perimeter of a circle with the same area. It is defined as

$$\frac{\text{particle perimeter}}{\text{perimeter of circle with same area as particle}} = \frac{\text{particle perimeter}}{2\sqrt{\mathbf{p}} \cdot \text{particle area}}$$

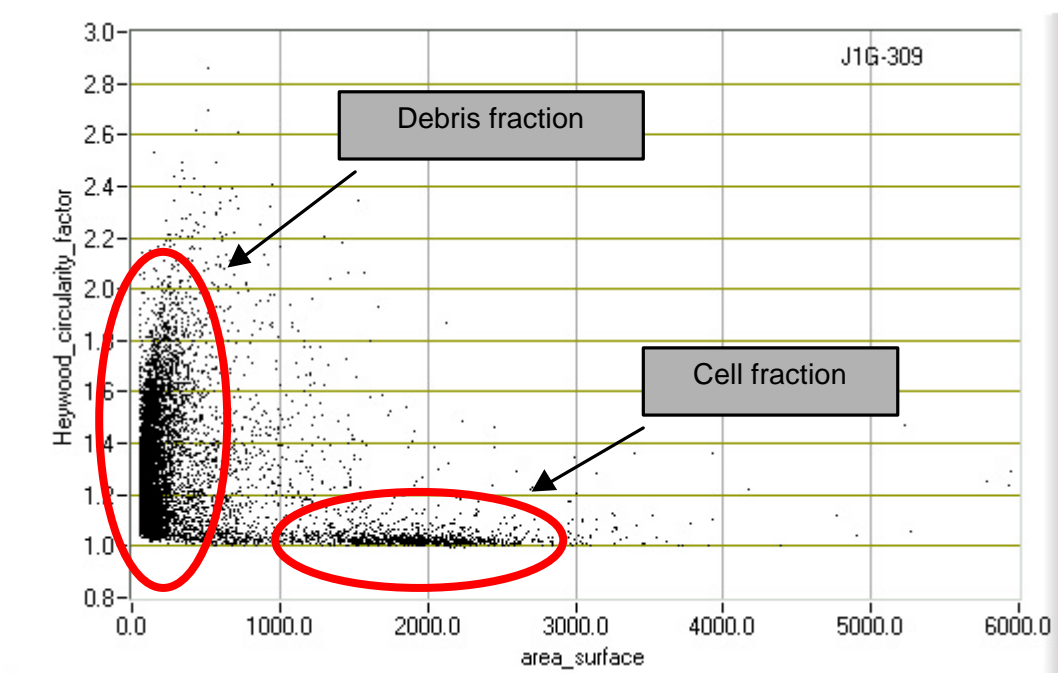
As an example Fig. 5-17 shows some circular, ellipsoid and irregular shaped objects and their position in a Heywood-circularity diagram. Circular objects have a Heywood factor of

one and lie on the horizontal axis in the diagram. All objects with other shapes have a bigger Heywood circularity factor and their position depends on their area and shape.



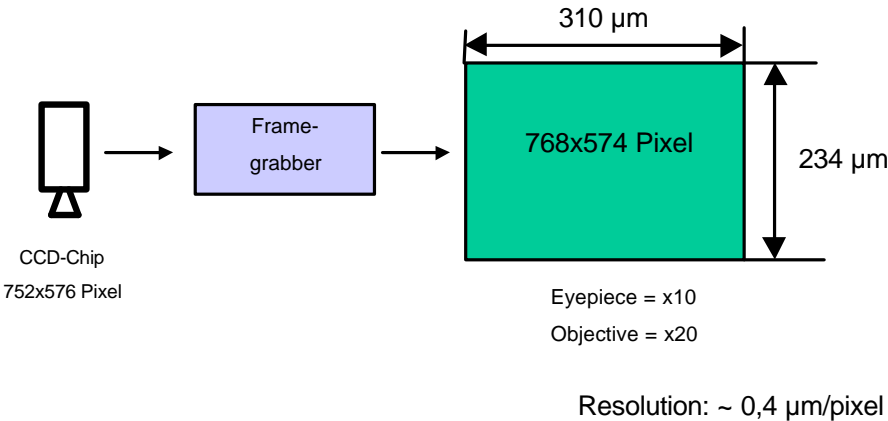
**Fig. 5-17 Influence of different sizes and shapes on the Heywood-circularity factor: Spherical particles have a Heywood circularity-factor of 1 and thus their position is only dependent of the particle size (area).**

Fig. 5-18 shows an example of a typical Heywood circularity diagram that contains two major particle clusters or fractions, a cell fraction and a debris fraction. Circular or slightly ellipsoid cells generate data points near the horizontal x-axis with a Heywood circularity factor close to one. All other objects generate data points further away from this cluster or in the second cluster that contains all small, irregular shaped objects.



**Fig. 5-18 Heywood circularity diagram with debris and cell fraction**

The unit of the parameter area-surface in Fig. 5-18 is the pixel. The geometry and resolution of the used video-microscopy by given magnification (x20) amounts ca. 0,4µm/pixel that allows the calculation of the diameter of circular objects Fig. 5-19.



**Fig. 5-19 Geometry and Resolution of the used video-microscopy (magnification x20)**

### 5.6.2. Morphological changes during production

It is well known that the morphology of cells in suspension changes during a cultivation process. The system developed here can be used for counting cells, to determine the viability and also for isolating morphological parameters generated by analysis of FullScans taken during cultivation processes. In this chapter the changes of the Heywood circularity factor as a function of the object area will be shown using the same cultivation that has been described previously in chapter 5.4. As mentioned before, the CHO cultivation was a simulation of a production process with three volume expanding steps followed by a production phase. The cultivation was performed as a parallel experiment in two similar bioreactors.

Fig. 5-20 and Fig. 5-21 show the results of the experiment with Heywood circularity plots added at important points of the cultivation course. The underlying diagrams in Fig. 5-20 and Fig. 5-21 show the course of the concentration of the viable cells and the product titer of both reactors and are the same as in Fig. 5-10. Fig. 5-20 shows four Heywood circularity diagrams from the beginning of the production phase, and Fig. 5-21 shows six Heywood circularity diagrams from the stationary phase.

At the beginning of the production phase ( $t=150\text{h}$ ), the Heywood circularity diagrams of both cultivations are very similar. Since the cell concentration was low in both bioreactors at the beginning of the production phase, the number of objects in the analyzed “nearly in focus” image plane was also low and therefore, the number of data points in the two Heywood circularity diagrams must also be low.

Approximately 40 hours later ( $t=190\text{ h}$ ) the distribution of morphological objects is still very similar, but in comparison to the diagrams at 150 h the density of data points is clearly higher because of an exponential cell growth. Two days later, ( $t= 248\text{ h}$ ), at the end of the exponential growth phase, the Heywood circularity factor diagrams start to differ from each other because a third cluster appears in the Heywood circularity diagram of reactor 2 between the debris fraction and the majority of cells (marked with an arrow).

Over the following measurements ( $t= 260\text{ h}$  and  $t= 320\text{ h}$ ) the third cluster increased further and was present until the end of the cultivation of bioreactor 2 was finished. In comparison, none of the Heywood circularity diagrams of bioreactor 1 shows this third cluster.

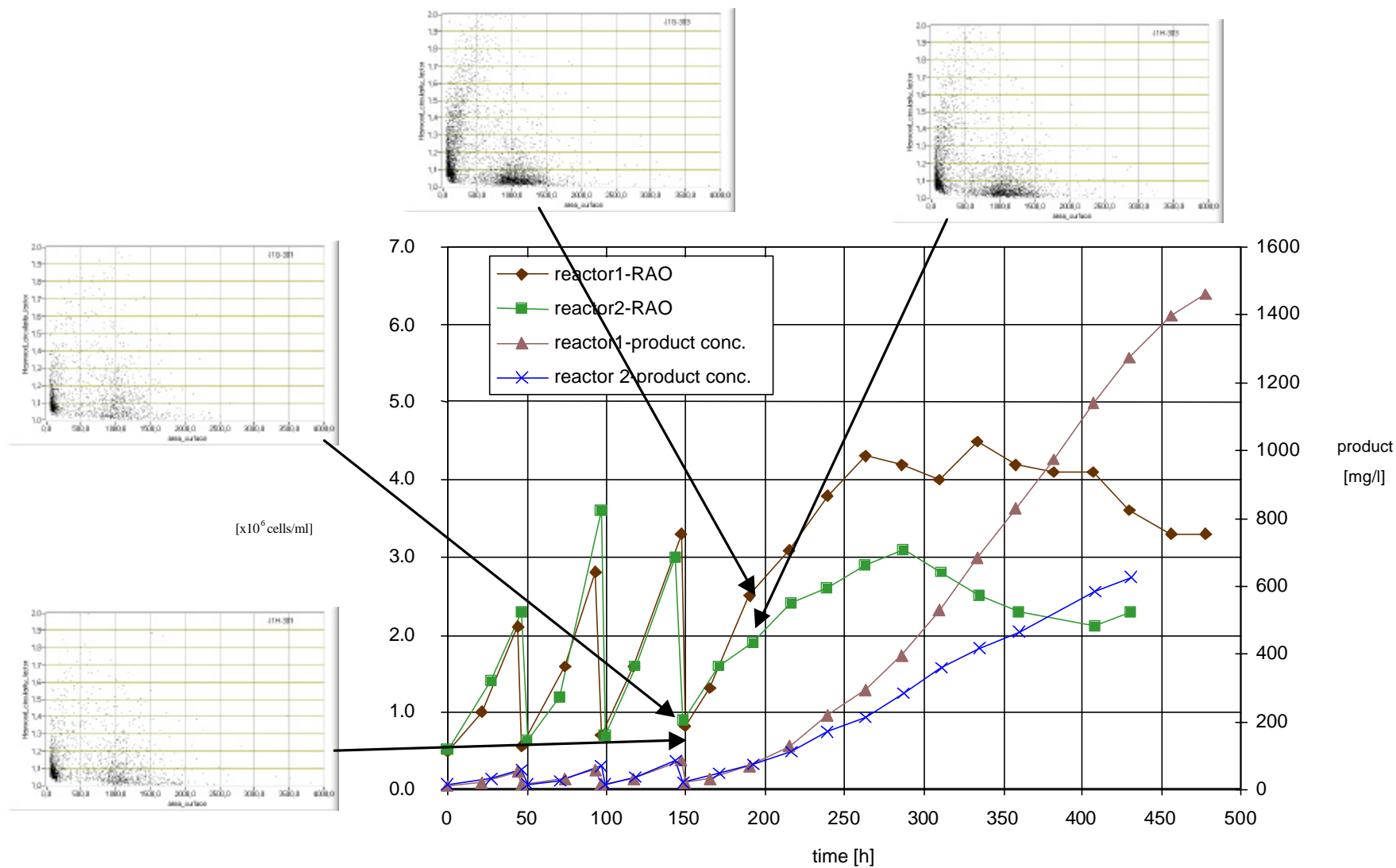


Fig. 5-20 CHO cultivation: Morphological analysis shown as heywood-circularity diagram at the beginning of the production phase

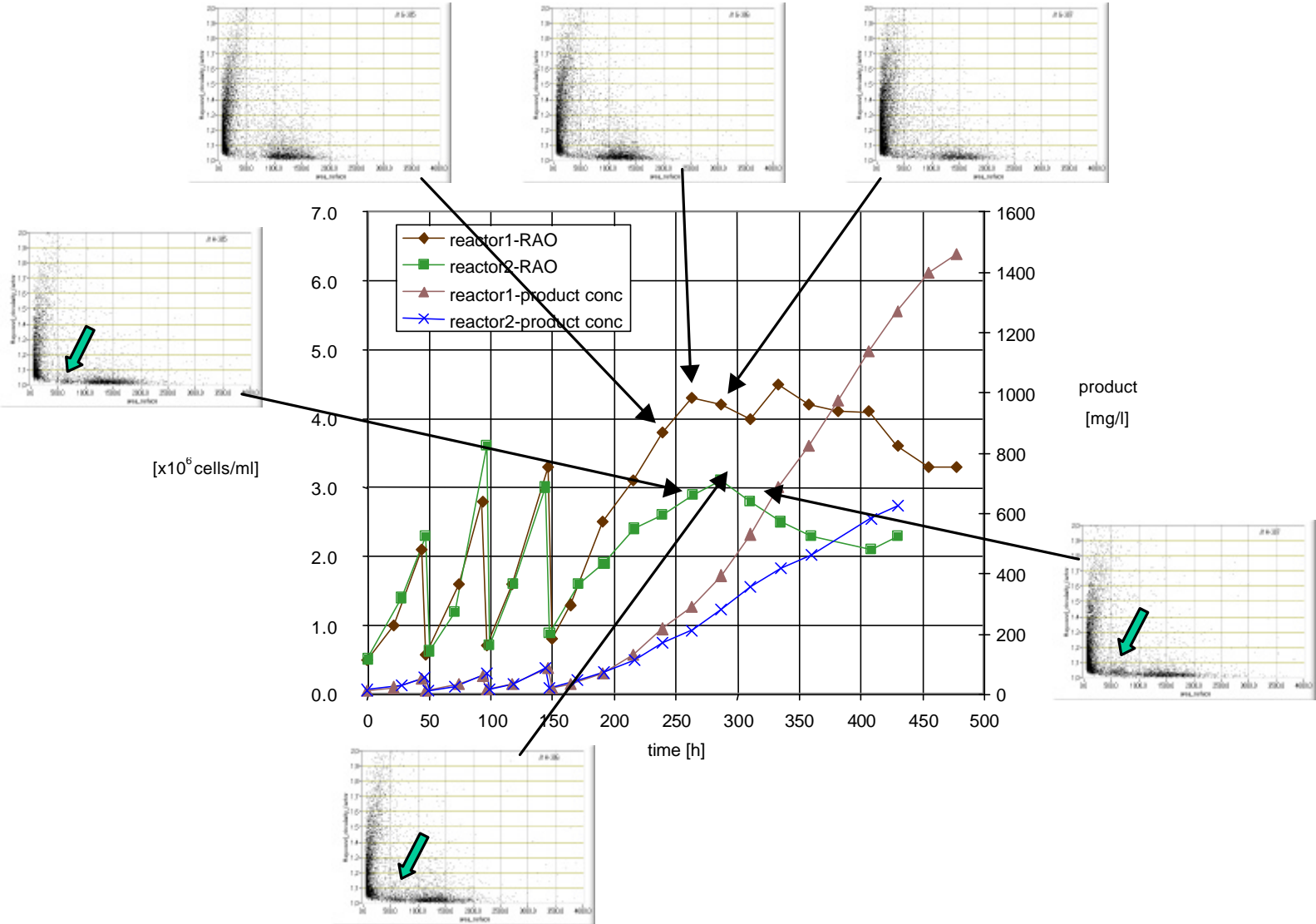


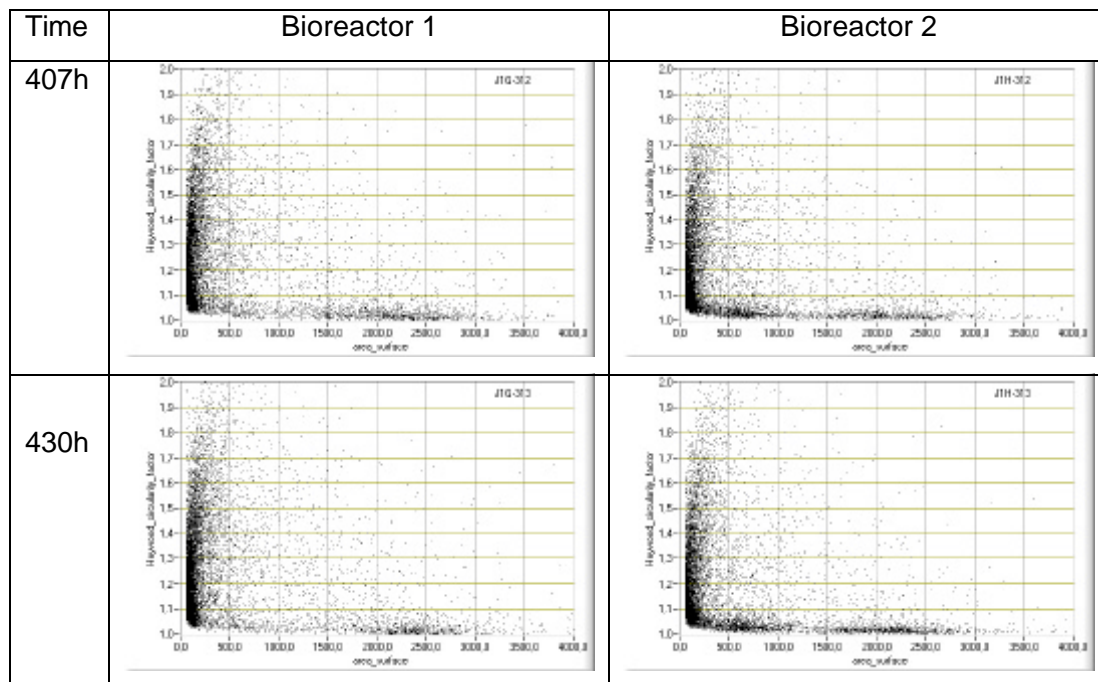
Fig. 5-21 CHO cultivation: Morphological analysis shown as Heywood-circularity diagram during the stationary phase

Fig. 5-22 shows four Heywood circularity diagrams from the end of the production phase at 407 h and 430 h respectively. Again, only the diagrams of bioreactor 2 show the third cluster with a density maximum at around 750 pixel units. In contrast, the Heywood diagrams of bioreactor 1 show at this point only a broad but weak distribution over a range of 1500 to 2700 pixel units.

On the basis of the geometry and resolution of the observation field, the mean diameter of the objects of the third cluster can be estimated by the following formula:

$$\overline{diameter} = \sqrt{\frac{4 \cdot area\_surface}{p}} \cdot resolution = \sqrt{\frac{4 \cdot 750\,pixel}{p}} \cdot 0,4\,mm / pixel \approx 12\,mm$$

During the exponential growth phase and at the beginning of the stationary growth phase the average of the normal cell cluster in the Heywood circularity factor diagram was in the range between 1250 and 1500 pixel, which results in a diameter of the cells between 16 $\mu$ m and 17 $\mu$ m.



**Fig. 5-22 Heywood-circularity diagrams at the end of the stationary phase of the CHO cultivation**

### ***5.7. Morphological changes by induced apoptosis***

To test the capability of the system to detect apoptotic cells on the basis of their morphology, two samples of CHO cells were taken from the mid exponential growth phase of a bioreactor cultivation and cultivated further in two t-flasks in the presence and absence of actinomycin D. Actinomycin D is a well-known inducer of apoptosis that intercalates with DNA, inhibits the transcription of DNA into RNA, and prevents DNA replication. Actinomycin D was used at a concentration of 2  $\mu\text{g}$  per  $1 \times 10^6$  cells in this experiment.

Both t-flasks were observed with the AMS. Several FullScans were taken during a cultivation period of 25 hours and subsequently all three image planes of the FullScans were analyzed. The data of the analyzed FullScans were presented as the number of refraction active objects (Fig. 5-23(a)), as the viability of the cells (Fig. 5-23(b)) and as Heywood-circularity diagrams that describe the morphology of the observed cells Tab. 5-4.

Fig. 5-23 shows the number of refractive active cells and the viability, determined by the automated microscopy system, during the cultivation in the presence of actinomycin D and of a control culture. The amount of refractive active cells was determined by the same method that has been previously described in chapter 4.3.1 and 5.3.1. At the time  $t=0$  h both cultures started with the same viability and cell density. Over the next 12 hours it can be seen that the viability of the actinomycin D induced culture decreased continually whereas the number of refraction active objects decreased only slightly during the first eight hours and then stayed almost constant. After 24 hours, the control culture without actinomycin D still showed a viability of over 80%, whereas the viability of the apoptosis induced cell culture had fallen to approximately 40% at the end of the experiment.

The changes in morphology are shown in Tab. 5-4. The table consists of Heywood circularity diagrams that represent different morphological changes of the apoptosis induced cultivation and the control culture with regard to the size and shape of the cells. At the time  $t=0$  h both Heywood circularity diagrams show two clusters of objects, a debris fraction between 0 and 200 area units, and the fraction that contains the cells in a range between 800 and 1400 units. The centers of both cell population fractions from both cultivations (control, apoptosis induced) were very similar with values around 1000 area units. After 3h the cell cluster of the apoptosis induced cells disintegrates and a loosely connected cluster with a wide range of different Heywood circularity factors arises, while the cell cluster of the control culture appears almost unchanged (Tab. 5-4 D2, K2).

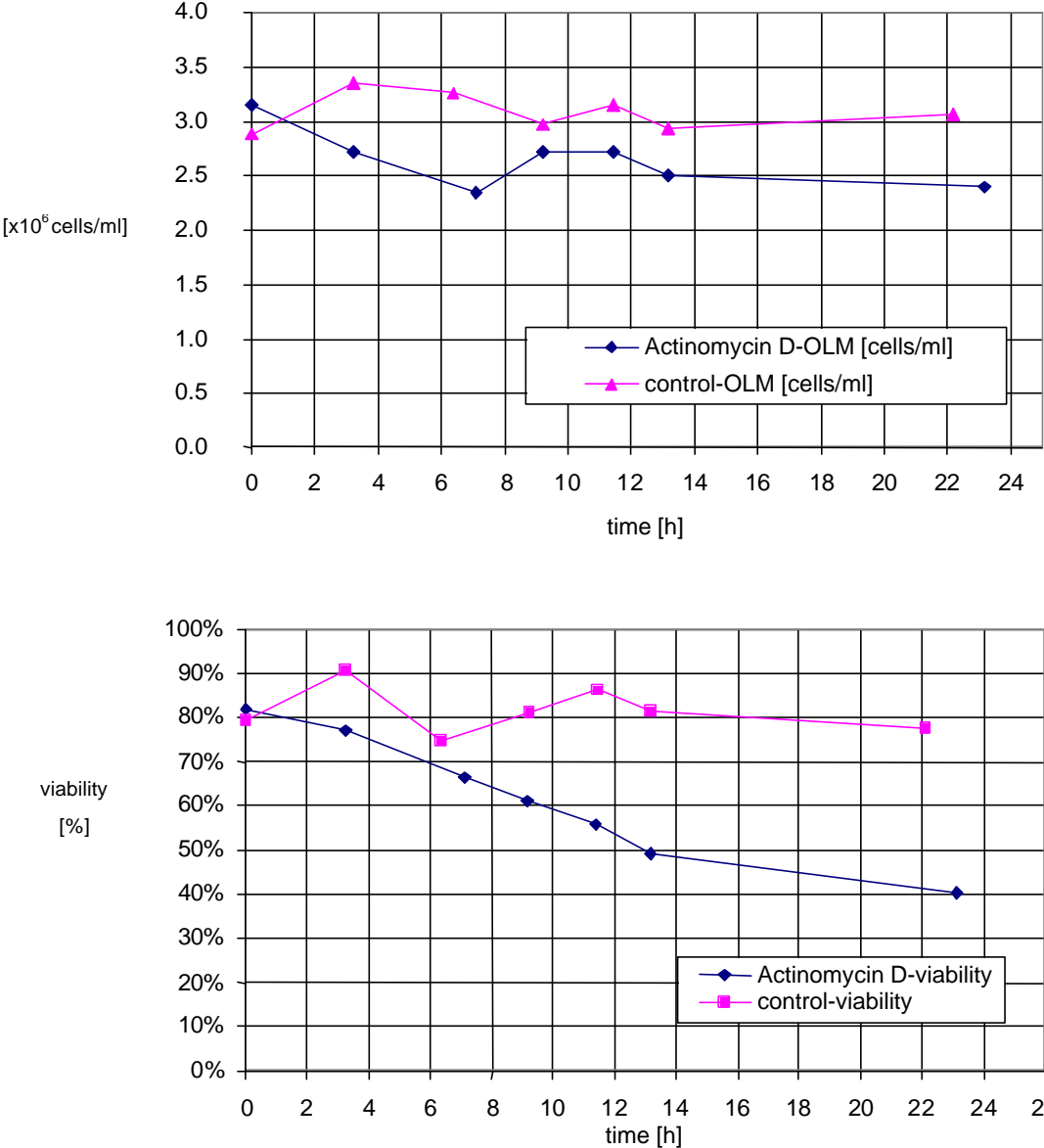
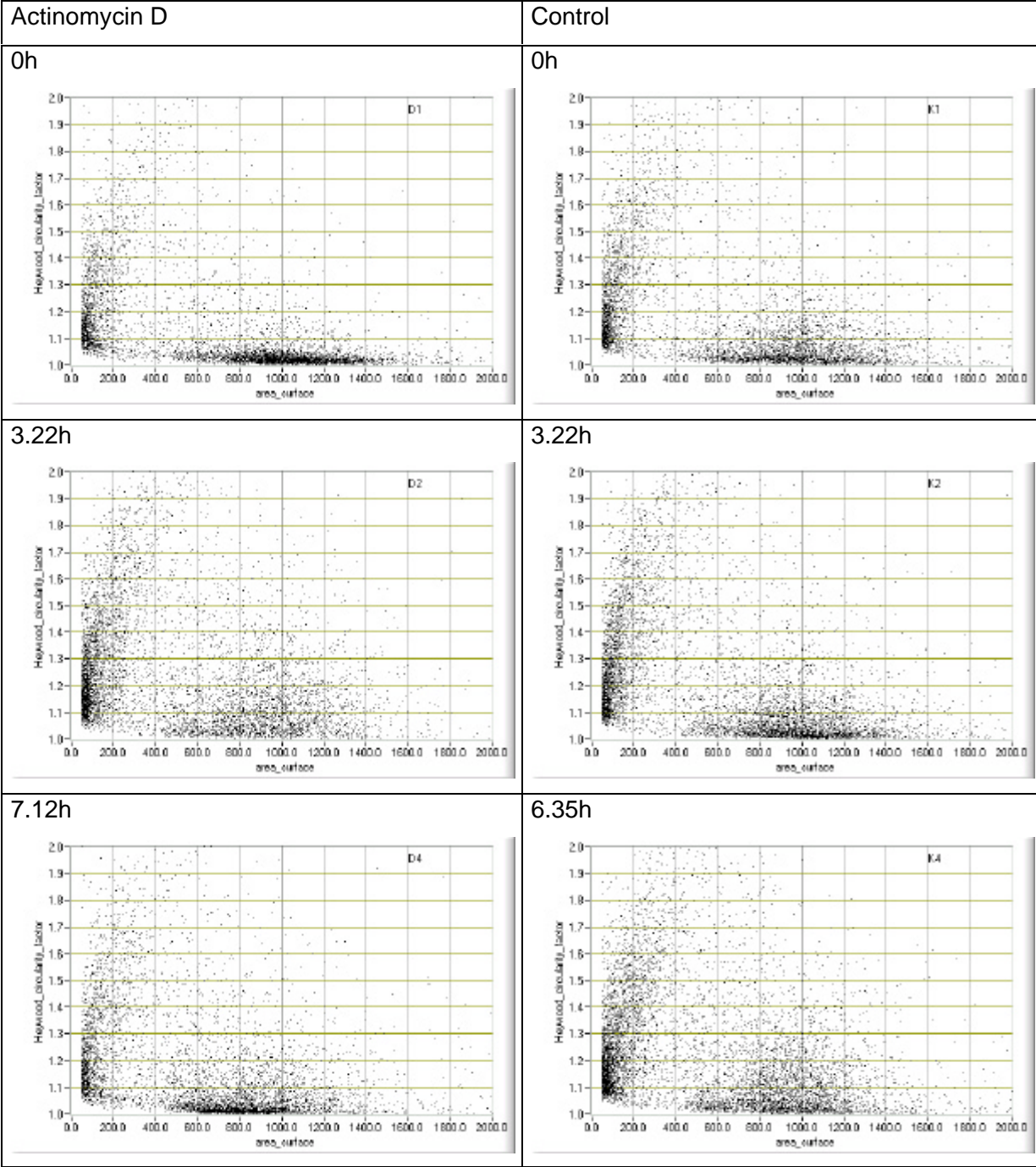


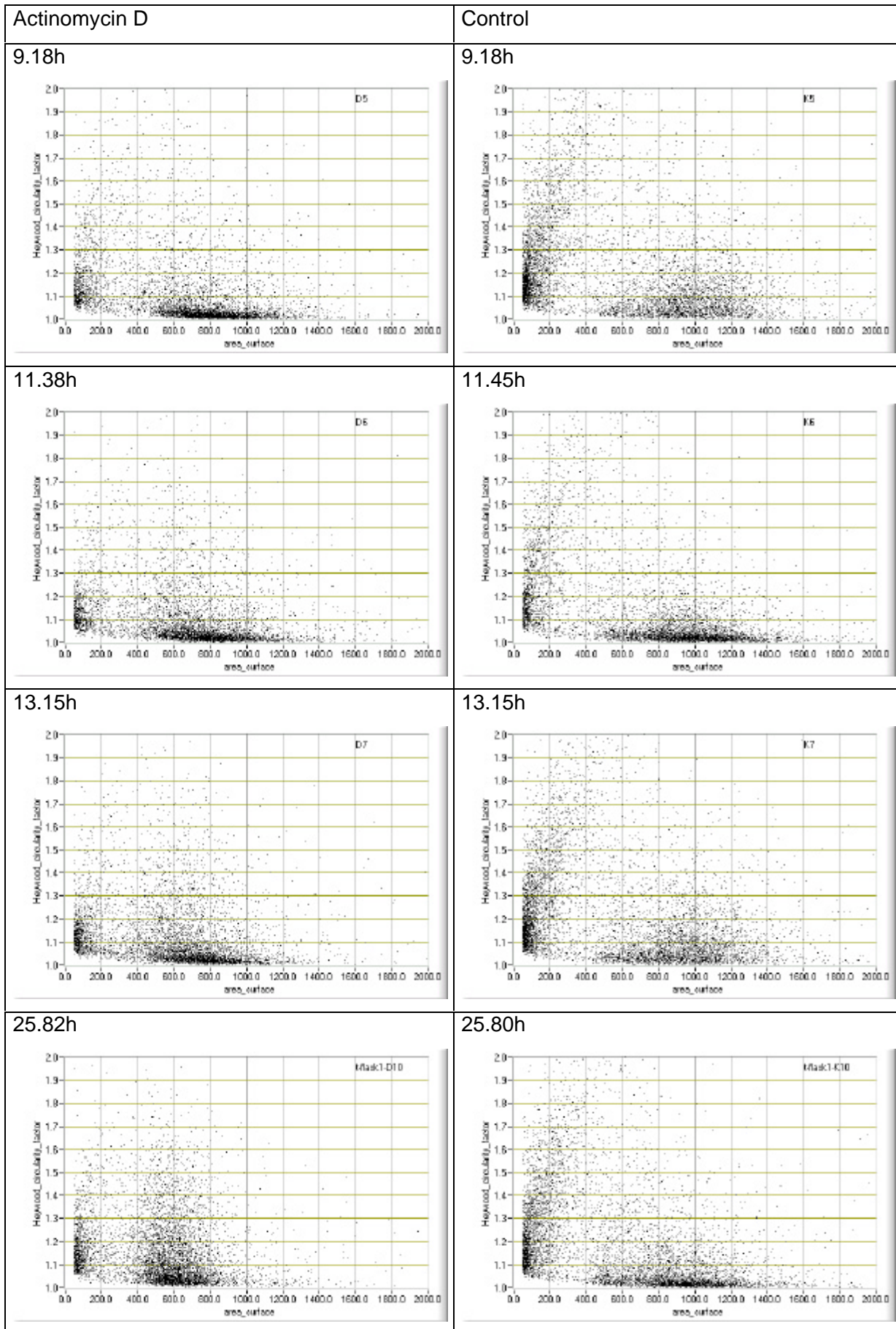
**Fig. 5-23 Hybridoma Cell Line apoptosis induced by Actinomycin: Conc. of refractive active cells and viability of two t-flask experiments (control, Actinomycin D), measured with the automatic microscopy system**

Seven hours after the experiment was started the Heywood circularity diagram of the apoptosis induced culture again shows a distinct cell cluster, but now the cluster has shifted down from formerly 1000 to 800 area units (D4). The center of the cell cluster of the control culture is still located at 1000 area units but the cluster also shows a more loose shape (K4). This phenomenon of a change in shape and density of the cell cluster of the control culture can be observed several times during the entire cultivation period. However, the center of the control cell cluster is in all cases located at around 1000 area units.

In contrast to the cluster of the control culture, the apoptosis induced cells show a significant shift of the center of the cluster down to 800 units, already a few hours after the beginning of the observation. During the course of the experiment the center of the cluster remains in this position but at the end of the experiment the cluster became more concentrated around the 800 area units mark and was no longer spread across a large range as at the beginning of the t-flask cultivation.

**Tab. 5-4 Heywood circularity diagrams calculated on the basis of taken FullScans at different times during a CHO cultivation in presence of the apoptosis inducer actinomycin D and in a control cultivation without inducer.**





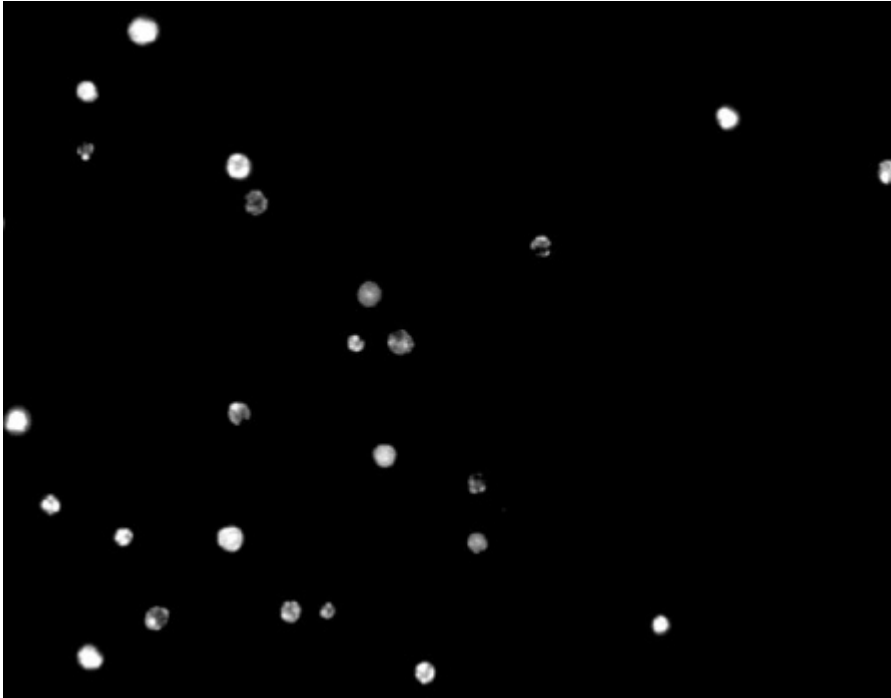
---

The appearance of apoptotic cells after induction with actinomycin D can also be looked at in purely qualitative way if the fluorescence image plane only is considered. Fig. 5-24 shows two images of two FullScans from both t-flask experiments. Both images were taken 11 hours after start of the experiment.

Fig. 5-24(a) represents one of one hundred images of the fluorescence images plane and should serve here as an example representing all other images of this plane. The image shows the typical morphology of apoptotic cells. J. Cohen (1993) describes in his review these morphological changes within the nucleus as follows: In general the nucleus shrinks and its chromatin becomes very dense, collapsing into patches, then into crescents in tight apposition to the nuclear envelope, and finally in many cells into one or several dense spheres. All morphologies described by Cohen can also be found in the image shown [Cohen, 1993].

In contrast to Fig. 5-24(a), Fig. 5-24(b) shows the stained DNA within the nuclei of the cells of the control culture that was not incubated in the presence of actinomycin D.. Several nuclei are also stained with DAPI but the morphology is completely different compared to the apoptotic nuclei. Most of the nuclei are spherical and of homogenous brightness. Only a few nuclei are irregularly shaped and only one nucleus shows a lower diffused brightness distribution which is typical for a necrotic cell death and suggests that the cell died accidentally and not because of nutrient depletion.

- (a) Time 11.38 h with Actinomycin D incubated cells



2001\_01\_30\_19\_16\_29, Scan\_3\_09, 11.3h, t-flask1-D6

- (b) Time 11.45h control culture



2001\_01\_30\_19\_42\_42, Scan\_3\_09, 11.4h, t-flask1-K6

**Fig. 5-24 Morphology of cell nuclei of two hybridoma t-flask cell cultivations: (a) incubated with Actinomycin D; (b) control. Analysis of the fluorescence image plane**

## 5.8. Error estimation of the used algorithms

### 5.8.1. “out of focus” and “in focus” algorithms

The two developed algorithms for analyzing images of the “out of focus” and “in focus” plane are relatively error insensitive. The high differences in contrast of the two observed image planes allow an easy threshold calculation and a simple separation of objects and background. The extension of the circle function, used in the “out of focus” algorithm, accompanied by a correction procedure ensures a separation even of closely packed cells. As with any other commercially available particle counters, the developed system also reacts sensitively to cell clumps, because the system is mainly designed for the observation of single suspension cells. However, the system can still cope with small cell clumps of 3 to 5 cells. The observation of the refractive active objects in the “out of focus” image plane is a major advantage in regard of counting cells in clumps. The refraction of cells and the focusing of the refracted light in the “out of focus” image plane as bright shining spots allows an easy separation of cells even of cells in clumps. As long as the clumps are not too large, i.e. without complex multilayers, each cell in the clump generates a separate spot since the spot brightness is relatively independent from the horizontal and vertical position of a cell within a small clump (see Fig. 5-25).

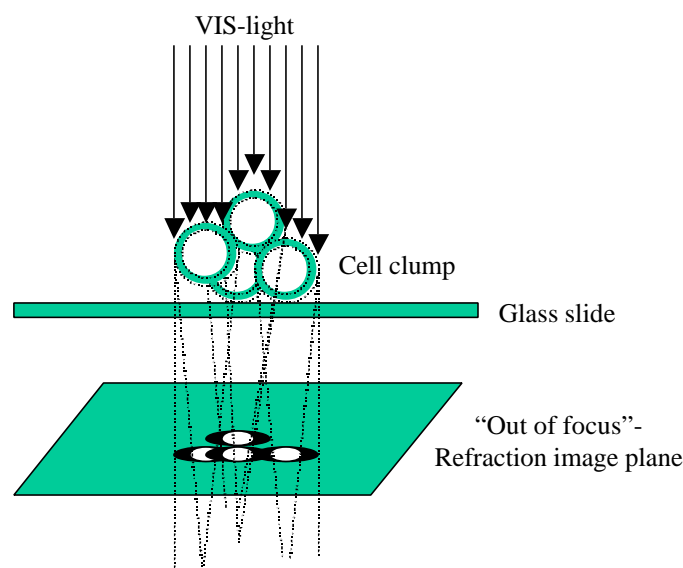


**Fig. 5-25 Simplified model of light refraction by a cell clump of four cells: Clump generates four separated bright shining spots with circular dark margins.**

### 5.8.2. “nearly in focus” algorithm

The following chapter gives a brief overview about errors that can occur during the morphological analysis of FullScans. Despite of careful design of the “nearly in focus” algorithm, it cannot completely be ruled out that the algorithm makes mistakes while analyzing “nearly in focus” images.

Common errors of the used “nearly in focus” image analysis algorithms are:

- Over-segmentation
- Insufficient separation
- Border problems

The main problem of the “nearly in focus” algorithm is over segmentation, i.e. means that the algorithm is unable to isolate the entire structure of a cell from the background. As a result the algorithm creates several truncated objects instead of a single cell. Fig. 5-26 shows an example of an over-segmented image. In comparison with the original image (also given in Fig. 5-26) the algorithm was not able to isolate several of the cells completely from the background. Instead, the algorithm created a lot of small objects, which were later identified as cell debris. The problem of over-segmentation can be overcome at least partially by modifying the filter parameters of the algorithm (parameter for isolating membrane structures or inner cell structures) in combination with increased or decreased illumination of the microscopic bright field images. Far more effective would probably be the integration of another algorithm, for example the “watershed”-algorithm of P. Soille (1998). This algorithm has been proven to work in very different applications like segmentation of X-ray body images, three dimensional segmentation of bone structures in CT images or segmentation of the cortical surface from MR images [Malpica *et al.*, 1997], [Rettmann, Xiao and Prince, 2000], [Boehm *et al.*, 1999], [Yi, Hyun-Sang and Ra, 1999], [Umesh and Chaudhuri, 2000]. An over-segmentation can be prevented by using a marker based variant of this algorithm. The algorithm has not been integrated into the current software version because the algorithm was not implemented in the actual version of the used image processing library by National Instruments. An manual implementation of the watershed-algorithm has not been carried out because of the complexity of programming.

A second problem that occurs when using the “nearly in focus” algorithm is “insufficient segmentation”. An example of “insufficient segmentation” is also shown in Fig. 5-26 (white arrow). In this case the algorithm was unable to separate two cells and counted them as one. Again this problem could overcome with the use of the “watershed”-algorithm.

The removal of particles that touch the border creates a third problem. The likelihood to touch the border is bigger for large than for small objects. Hence, the algorithm more often removes large objects than small objects, which leads to a further over-estimation of small objects.

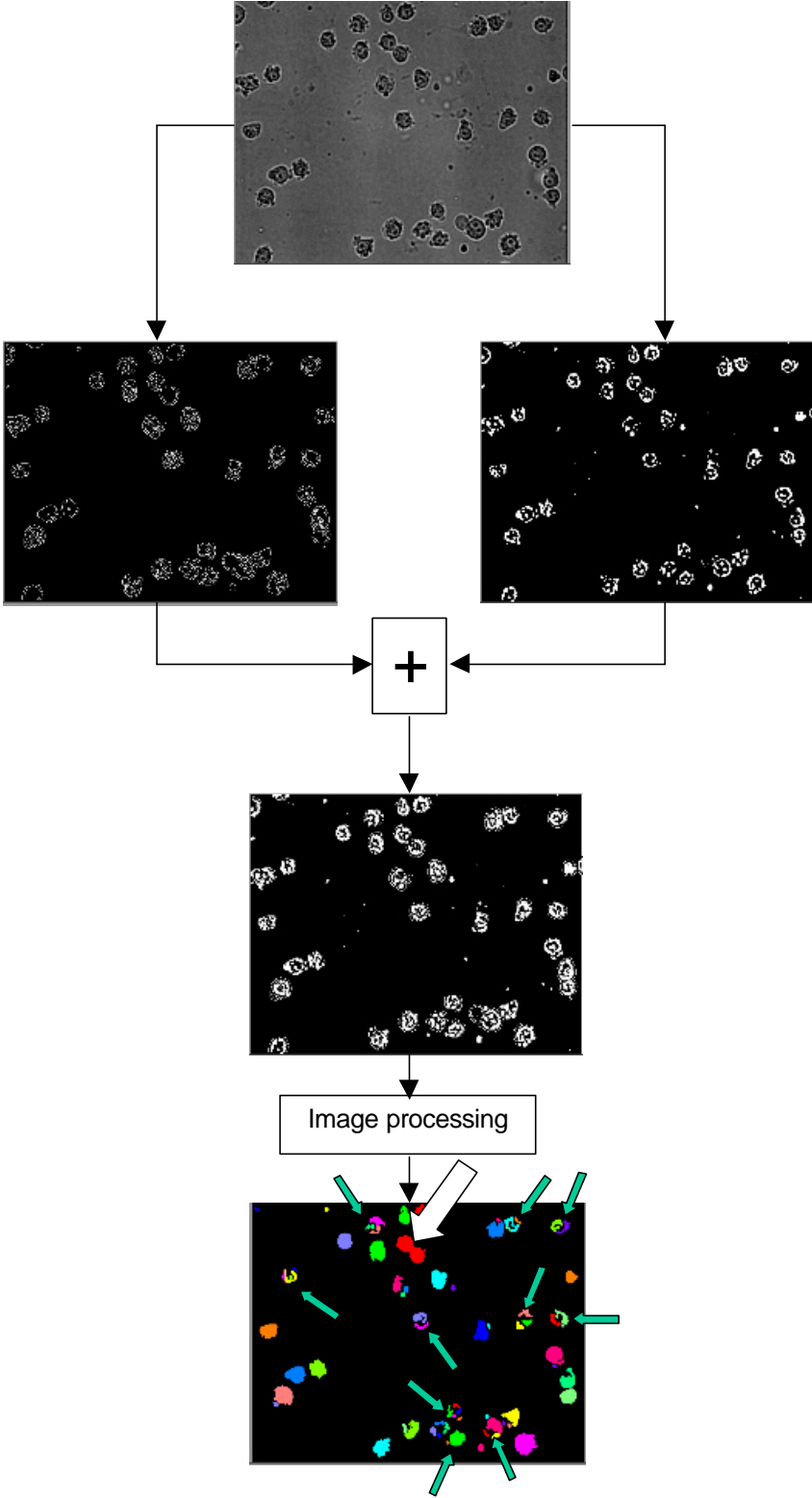


**Fig. 5-26 Over-segmentation and insufficient segmentation of cells: Example shows original image and the major steps of the image processing. Small arrows in the final image mark the cells, which were over-segmented and split in several small particles. The white arrow shows two cells that could not be separated by the algorithm and were counted as one.**

## 6. Discussion

With the system described here an analytical tool has been designed that combines capabilities and techniques of different systems, which are normally used separately. The implementation of two different scanning strategies presents the possibility to answer a wide range of different questions with only one device. Time resolved scans allow the investigation of cells under defined anoxic conditions over a long time period. The choice of at least two scan planes e.g. the common bright field image plane and the fluorescence image plane and the subsequent overlay of these planes, allows a better and deeper insight into the changes of cell morphology than it would be possible with a single bright field image. The generation of time-lapse video sequences allows the observation of the dynamics of dying cells. A quantification of the fluorescence signal gives an insight into the dynamic staining process, which would be impossible when only static images were analyzed. As well it can provide the observer with additional information about the kinetics of the penetration of the dye into the cells. Finally, the dynamics of staining can be compared between different SnapScans.

### ***6.1. Speed of the implemented autofocus***

In chapter 5.1 different autofocus functions were investigated and it has been shown that the autofocus function F5 was the most suitable to find the best focal point. Function F5 can detect the best focal point when using bright field images, fluorescence images of cells or fluorescent microspheres. In all cases the function F5 produces a clear extremum at the position of the sharpest point and, in comparison with all other functions, function F5 was the most reliable one. On the basis of this results a standard calibration procedure was integrated in the control software. This calibration procedure can easily be executed during start-up the system or whenever a new calibration of the system is necessary, e.g. for cleaning of the flow-through chamber or shut-down of the entire system.

The use of microspheres from Molecular Probes (see 3.2.4) guarantees a more accurate calibration than mammalian cells because microspheres are very homogenous in size and shape and their optical properties are very similar. Based on determination of the 3D profile, as described in chapter 5.1.4, the distances between the fluorescence focal plane defined by the profile and the other two planes of a FullScan (“nearly in focus”, “out of focus”) have to be determined empirically.

The biggest limitation of the investigated autofocus functions is speed. An implementation of an online autofocus that can find the focus on-line at each position while a FullScan is executed is impossible because of the following limitations of the developed system:

The calculation time of all tested autofocus functions is too long for an implementation of an on-line autofocus at each position. The use of size reduced images to increase the calculation speed is not feasible because of a loss in accuracy in detecting the extremum of the focus function.

Moreover, the mechanical z-axis servo drive of the microscope is not suitable to endure the mechanical stress of a focusing at every position during a scan.

For the developed system with the two scan modes FullScan and SnapScan the current autofocus procedure is sufficient and the reduced mechanical stress prolongs the life-span of the system. Only in case of further development, e.g. the use of microtiter plates instead of the flow-through chamber, will a more advanced autofocus procedure be necessary.

### ***6.2. FullScans - basis for the determination of an extended viability***

In the experiments of chapter 5.3 it has been shown that the course of mammalian production processes in regard of cell number and viability can be described more accurately by the recording of a FullScan and the subsequent analysis of all three image planes of the taken FullScans than it can be manually done. The introduction of three scanned image planes instead of only one, as in case of manual determination of cell number and viability using the trypan blue exclusion method, can accomplish a far higher degree of information. The observation of cells "out of focus" allows getting information about the three-dimensional structure of the cells that cannot be obtained when a normal bright-field image near of the sharpest focal plane is analyzed manually. The ability of cells to refract light is directly dependent on their cell volume, shape and size. The simple model of Fig. 5-7 (chapter 5.3) should emphasize that. Only when a cell is covered with a intact cytoplasm membrane, showing smooth surface without any blebs or cracks, the cell can hold sufficient active cell volume to refract light. However, the existence of active cell volume is absolutely necessary for all metabolic activities of the cell and also for any product forming. Only if a certain amount of active cell volume exists, including all cell components, is the cell able to refract light in the quantity that a bright spot of focused light is being generated in the chosen out-of focus image plane. Thus, a direct relation exists between the spot size in the "out of focus" plane and the active cell volume. In conclusion, the "out of focus" image plane contains information about the three dimensional structure of cells that cannot be described by any other image plane.

The developed “out of focus” algorithm works as a filter that filters out all objects which generate only weak spot signals. If the filter threshold is chosen correctly the algorithm counts only cells with a sufficient active cell volume. The experiments show that the counts of refractive-active objects correlate very well with the number of viable cells determined by the trypan-blue exclusion method. However, in contrast to the manual method, the automatic method is much more stable. In the stationary phase of batch or fed-batch cultivations it often comes to an over-estimation of viable cells by using the trypan blue exclusion method, because well formed viable cells and flat cell bodies that lost large amounts of their cytosol can be look very similar. The bright field image plane chosen manually only contain information about the cells on the basis of absorption, diffraction and scattering, which are not sufficient to describe the 3D structure of a cell. The observer often cannot distinguish between a normal shaped cell and a densely packed cell ghost, because both objects absorb light in a similar way and generate very similar images. Without the “out of focus” plane the observer gets no further information about the three-dimensional structure of the object, although this information is necessary to make the right decision whether a cell is viable or not. A staining with trypan-blue is often not sufficient, because of the weak contrast differences between stained and unstained cells. Apoptotic cells in particular are highly condensed and contain dense intracellular structures, which strongly absorb light. To make a decision whether these cells additionally contain trypan-blue that penetrated the cell membrane is very difficult. In contrast, the use of DAPI as fluorescence marker allows a very simple detection of cells being penetrated by the stain and simplifies the decision, whether a cell is damaged or not, because the fluorescence signal cannot does not interfere with dense cell structures.

The SnapScan shown in chapter 5.2.1 should serve as an example for another phenomenon that can falsify the manually counted number of viable cells. As shown in this video sequence cells at the end of their life cycle burst and eject membrane covered vesicles, which can stay attached to the remaining cell body. After a period of time these vesicles melt again in a fusion process with the old cell body. The newly arisen object looks like a normal cell but contains only the residue of the formerly living cell. In this case, the “out of focus” plane shows a weaker shining spot because of the decreased refraction index of the cell due to the loss of cell components during the burst and fusion process. When only the bright field image plane was manually observed, a human observer could often not distinguish between a dead or viable cell. The observer even could count these objects as dividing cells, which leads to a completely wrong assessment of the status of the culture.

### **6.3. Comparison of automated cell counts and product titer**

In several fed-batch cultivations performed during the test phase of the AMS it has been shown that it is often possible to determine the slope of a linear phase that appears when viable cells change their growth kinetics from exponential growth to limited growth. In several cultivations these slopes fitted well to the slopes that were determined by analyzing the product formation in the same way as the course of the viable cell concentration. The two CHO cultivations of chapter 5.4 support this assumption. The slope determined at the point of inflexion combined with the maximal cell concentration allows a rough estimation of the product titer at the end of the cultivation. However, not all cultivations allow the determination of a slope during the transition from exponential growth to the stationary phase, especially in batch and not optimized fed-batch cultivations with a short growth phase. The hybridoma cultivation shown in chapter 5.4.3 is such an example. For this example it is very unusual that the slope of the total cell number can be correlated with the slope of product formation. It still will need further experiments to determine if this relation is accidental or not.

Generally it can be said that the counting of refractive active objects correlates with the viable cell number of a culture. Furthermore, the number of refractive active objects is related with the three-dimensional structure of the objects and depicts the spatial volume of the cells, which is a prerequisite for any product formation. Thus, the number of refractive active objects is a better basis to estimate product formation than the cell number, because the latter represents the three-dimensional state of an object very incomplete.

Following the assumption that product formation is non-growth associated which has been reported for several mammalian cell cultivations in the literature [Dutton *et al.*, 1998], [Seifert and Phillips, 1999] production can be described by this equation:

$$P = \mathbf{b} \int x_v dt \quad (1)$$

Again, the calculation of the cumulative cell hours on the basis of the number of refractive active objects gives more reliable results because of the inclusion of the spatial condition of the cells.

### **6.4. Direct detection of apoptosis**

The early detection of apoptosis by a single parameter such as the DNA distribution in the nuclei of the cells is not possible with present system, because the used fluorescence dye DAPI only penetrates the cells in the late developmental phase when the cell membrane became permeable. Also the direct detectable DNA distribution in the nucleus is not always significant for apoptosis. Moreover, the system itself is limited in the dynamic range of the used video camera. The insufficient dynamic range leads to the problem that the camera

cannot simultaneously detect weak fluorescent objects, e.g. necrotic nuclei and parallel strongly shining objects like apoptotic bodies or condensed DNA in the nucleus. If the sensitivity of the camera is adjusted to detect bright shining objects correctly, the sensitivity is too low for the detection of weaker shining objects. On the other hand, the camera detects the weaker shining objects correctly but then the CCD chip is saturated with the bright shining objects and all details will be lost. Thus, at present, the system can only detect apoptotic cells by multiparameter analysis including the fluorescence distribution and morphology changes like shrinkage or blebbing.

Besides it is disputable whether a direct determination of apoptosis or necrosis in stirred bioreactors is necessary at all. The major application of the AMS is the routinely control of bioreactor cultivations, especially fed-batch processes in the biopharmaceutical industry. Generally these production processes are designed to maximize the product titer and must guarantee a constant product quality. In these processes apoptosis is the main problem because of a depletion of nutrients or the excretion of toxic byproducts during the progress of the cultivation. With the possibility of recording FullScans the system can control the run of a cultivation by observing several parameters and can recognize changes early. Necrotic cells occur only when cells have been injured by strong mechanical or chemical stress, which has to be prevented from the beginning. Because of the high sensitivity of fluorescence dyes used for the determination of the viability, cell damaging processes, which lead to necrotic cells can be detected very fast.

## **6.5. Applications for SnapScans**

### **6.5.1. Morphological changes under defined conditions**

The easy use of SnapScans allows the study of morphological changes under defined conditions over a long period of time. Moreover, the subsequent generation of video-sequences allows an observation of the dynamic of morphological changes that can otherwise only be hardly achieved. The quantification of the fluorescence gives additional information and allows a quantitative comparison of different SnapScans.

### **6.5.2. Test of stability - Clone selection**

As an application of SnapScans it is conceivable that SnapScans can be used for a systematic clone selection in regard of finding the best clone for large-scale production. As Al-Rubeai (1997) wrote, the selection of clones by exposing the cells to, e.g. anoxic conditions is a possibility to select more robust cell clones for large-scale biopharmaceutical productions. The finding of high-producer clones is normally a very time-consuming task and

often there is no guarantee that the clone, selected on the basis of microtiter-plate and t-flask experiments, is also the best clone for production in large scale stirred bioreactors. Especially during large-scale cultivations it can occur that the dissolved oxygen falls short of the minimal limit [Varley and Birch, 1999]. Hence, a testing of the ability of the clone to cope with anoxic condition is very useful.

The conditions during a running SnapScan are equivalent to that described by Al-Rubeai. After the cells are loaded into the flow-through chamber a supply with oxygen is not possible anymore. When the remaining dissolved oxygen is exhausted the conditions in the chamber are, therefore, completely anoxic. Moreover, sparging of the sample in advance with nitrogen can accelerate the attainment of anoxic conditions, so that the sample is complete free of oxygen, before a SnapScan will be started. Therefore,, SnapScans could be a fast method to test different clones for their suitability to culture in large-scale bioreactors. The fluorescent profiles over the time of different cell clones (see example in Tab. 5-3) can be easily compared. The clone with the slowest increasing fluorescence signal is the most resistant clone to anoxic conditions.

Another idea for using SnapScans as a helpful tool for selecting the best clone is the use of fluorescent proteins. Proteins, e.g. GFP can be used as markers to quantify the strength of expression. The use of these fluorescent proteins in combination with the AMS can present new and fast possibilities to screen for producer cells with a strong expression-rate.

### **6.6. System robustness and overall performance**

More than 700 FullScans and several SnapScans have been taken during the present work. The system is currently used routinely for the observation of cultivations of mammalian cells at the Biotechnology Development Department of the Novartis Pharma AG, Switzerland. During the entire development and evaluation phase only one syringe module had to be replaced. However, absolutely necessary for a continuous operation is a periodical maintenance of the staining system and the microscope. The short lifespan of only 100 hours of the used Osram HBO mercury arc lamp makes a regular exchange of the lamp necessary, which causes a subsequent calibration of the system. Exchanging the lamp and calibrating the system are the only two maintenance operations that must be carried out regularly. None of the other components need any maintenance. During a permanent operation only the CIP-solution, pure water, 70% ethanol and the dye must be refilled when empty. The system was constructed in a way that it can work semi-sterile which means after a measurement cycle all cell or media residues will be removed by the CIP-solution. Additionally, the sample-tube and

the syringe S1 are purged with 70% ethanol that prevent the system from any bacterial or fungal contamination during long operation interruptions.

The developed database and raw data storage concept have been proven to be sufficient to handle the large amounts of data generated by the system. The 700 performed measurements have occupied more than 5 GB so far, the morphology database has a size of more than 380 MB and the number of images has exceeded the limit of 210.000 files.

### ***6.7. Comparison of the developed system with commercially available variants***

It is certain that the importance of image processing will increase over the next years but up to now only one system based on optical observation of mammalian cells in combination with subsequent image processing and analysis is commercially available. The CEDEX® system of Innovatis, Bielefeld, Germany performs the trypan-blue exclusion method automatically but instead of the system presented here, the CEDEX system can only generate some very simple morphological parameters because of the very low resolution of the recorded images.

A comparison of both systems is shown in Fig. 6-1. The advantage of the, system developed in the present work, is massive image and data recording, processing and the analysis with enhanced resolution. The images shown in Fig. 6-1 give an impression of the differences in resolution between the two systems and explain why a reliable analysis of cell morphologies is only possible with the AMS. The CEDEX system cannot show any details of the cells because of the low resolution of the taken images. A differentiation between stained and unstained cells can be made, but because of the small dynamic range of the used 8 bit video system, the results based on the evaluation of only one image plane is error-prone. In opposite, the AMS makes further image planes available containing partially redundant information and, therefore, offers the possibility to complete and correct investigated results. Moreover the AMS takes 300 images of 3 different images planes in a higher resolution with more details compared to maximal 32 images taken by the CEDEX system. The only disadvantage is a longer measurement time, but the system is still in experimental state and no optimization of speed of the algorithms or speed of cleaning procedures has been carried out so far.

The system has been well tested in more than 700 measurements and generates more reliable and deeper insights in the morphology of mammalian cells than any other system or even a human observer. The development of the two measurement principles FullScans and

SnapScans allows a routinely observation of samples directly coming from the bioreactor. It also allows the study of morphological changes during defined conditions in the flow-through chamber. The generation of video sequences allows time-lapse observation of processes that takes usually hours in a few seconds.

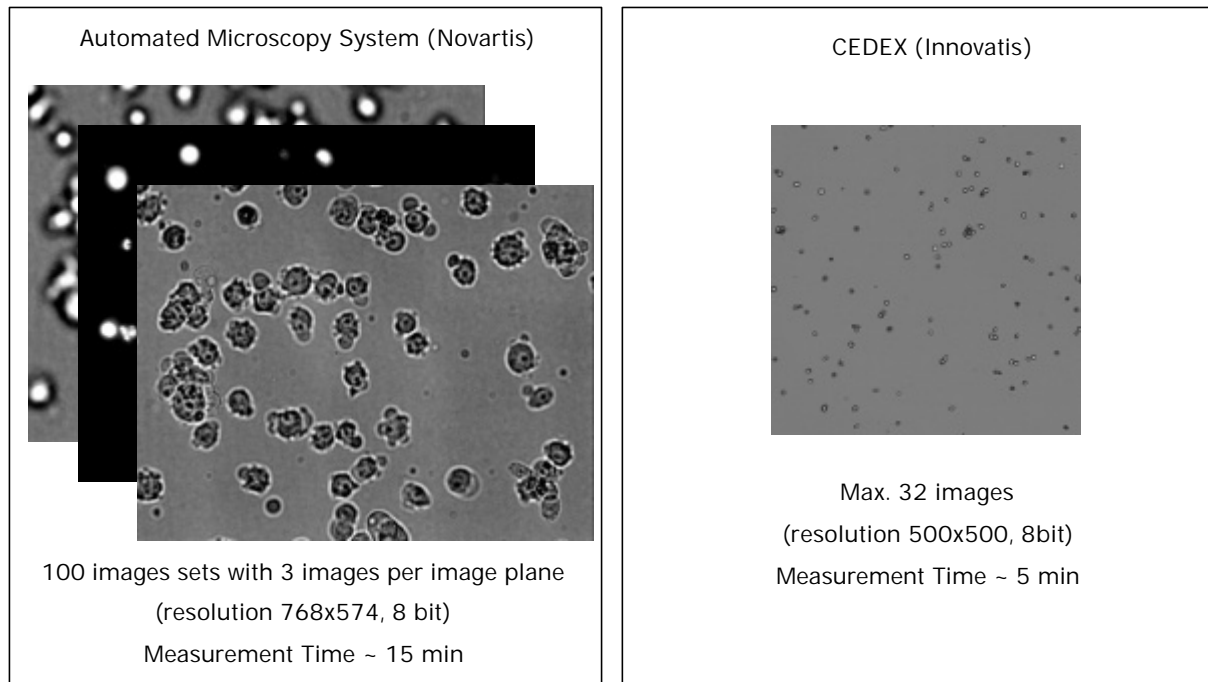


**Fig. 6-1 Comparison of the automated microscopy system with the only commercially available system (CEDEX, Innovatis, Bielefeld, Germany) based on optical observation, image processing and analysis.**

## **6.8. Suggestions for future work – An Outlook**

The presented optical system for monitoring mammalian cell cultivations is the first step in a future development of a microscopy system that can be used for a broad range of different applications. The combination of a flow-through chamber with devices for liquid-handling and a computer has been shown several times before [Maruhashi, Murakami and Baba, 1994], [Tucker *et al.*, 1994], [Thomas and Paul, 1996;] but only the combination of non-expensive hardware and highly sophisticated software makes a fast development of efficient image processing and analysis algorithms even possible, without strong expert know-how. In this chapter an outlook will be given of possible future developments and applications of the AMS.

### **6.8.1. Improvement of the image analysis of fluorescent spots**

So far the fluorescent spots are predominately analyzed by the developed “in focus” algorithm. Furthermore, a possibility exists to evaluate the intensity of fluorescent spots, the average and the standard deviation of the spot. The standard deviation is a measure for the irregularity of the gray levels within the spot and can be used for characterizing the DNA distribution to distinguish between apoptotic and necrotic nuclei. First attempts have been made to extend the “nearly in focus” in a way that the algorithm can cope with images of the fluorescent image plane. This would allow an improved analysis of even the morphology of fluorescent spots.

### **6.8.2. Fast adaption of new staining procedures**

The developed script language allows a flexible and easy programming of the AMS and a fast adaption of the existing scripts. From the start of the project attention was paid to create a system that can be adapted to new staining procedures. DAPI the DNA stain used in the project was only a model dye that can be replaced by any other appropriate fluorescent dye. DAPI was used because of much experience with this type of dye, its stability at room temperature and its easy handling. However, in future the detection possibilities of the system can be easily expanded by using other fluorescent dye [van Adrichem, 1997]. Some examples of useful dyes and their applications are given below:

**Tab. 6-1 For future staining procedures useful dyes**

Dye	Application	Principle
Annexin V conjugates	Apoptosis detection	In normal viable cells, phosphatidylserine (PS) is located on the cytoplasmic surface of the cell membrane. However, in apoptotic cells, PS is translocated from the inner to the outer leaflet of the plasma membrane, thus exposing PS to the external cellular environment. The human vascular anticoagulant, annexin V, is a 35-26 kD phospholipid-binding protein that has a high affinity for PS. Annexin labeled with a fluorophore can identify apoptotic cells by binding to PS exposed on the outer leaflet.
Fluorescein diacetate	Viability /cytotoxicity	Enzymatic decomposition; formed by intracellular hydrolysis
Antibody conjugates	Specific antigen detection	Detection of fluorescence labeled antibodies

### 6.8.3. Multi-color staining with different fluorochromes

An obvious extension of the present system is the exchange of the current 256 gray-scale video camera with a 8bit color RGB video camera. This would enable the system to detect different colored fluorescence dyes and would also allow the detection of several fluorescence events in parallel. Two examples of multicolor staining with three different fluorescence dyes are shown in Fig. 6-2. The use of three different fluorochromes (DAPI, propidium iodide, and acridine orange) results not only in three distinct colors but also allows numerous combinations of different colors because of the overlapping of single stains.

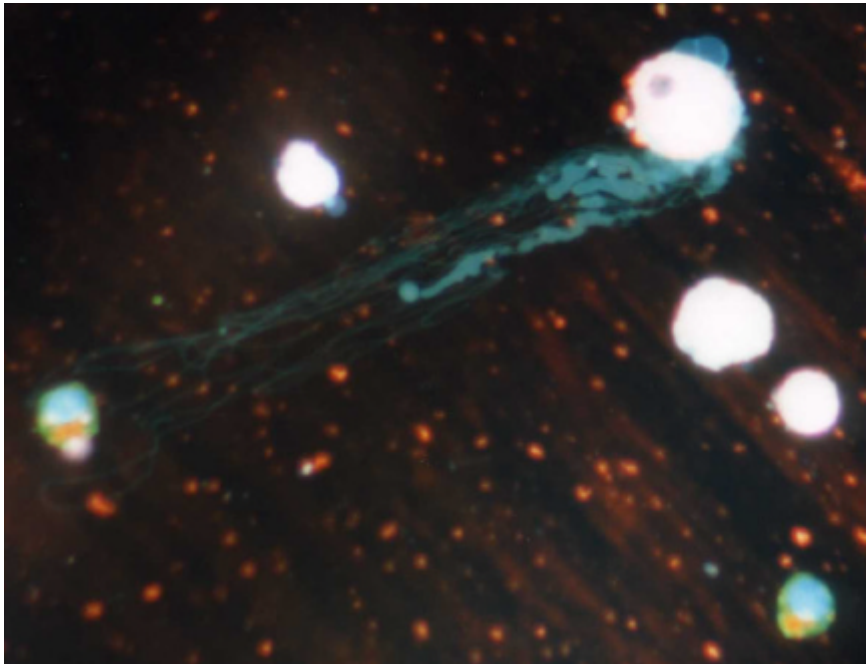
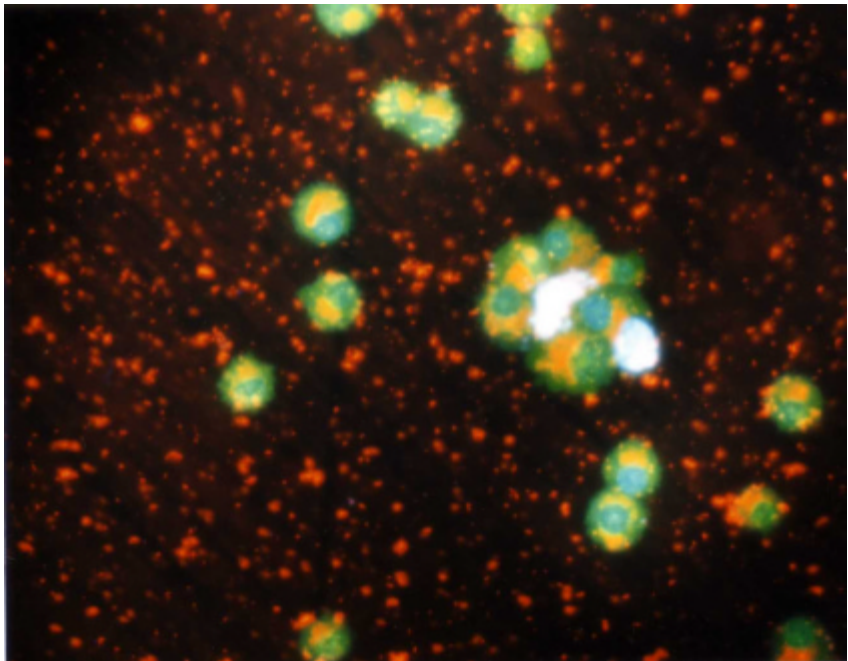


**Fig. 6-2 Two multicolor images generated with three different fluorescence dyes: acridine orange, propidium iodide, and DAPI; cell line: CHO cells; 40x objective**

#### 6.8.4. Scanning of microtiter-plates

A future extension of the system will be the development of a procedure for scanning microtiter plates instead of scanning a flow-through chamber. An important application for an automatic microplate scanner that can count cells by analysis of the bright field image plane and can estimate the viability by counting refractive active objects, is the observation of clone finding experiments which stand at the beginning of every commercial biopharmaceutical process with mammalian cells. Normally, after transfection of mammalian cells a tiring and tedious search begins with manual screening of large numbers of microtiter plates to find the best growing clone. An automated system could help here in this early production phase to relieve lab-staff from a large part of the manual work and to increase the throughput. The system could scan microtiter plates automatically, note down the position of the cells and find the cells again in the next observation cycle to determine the growth rate in each well. The observation of both image planes ("out of focus" and "nearly in focus" image plane) allows a simple cell number detection and a non-invasive determination of viability by evaluation the number of refractive active objects.

Using microtiter plates and working non-invasively does not allow the use of additional fluorescence dyes, hence analyzes would normally be restricted to the evaluation of only two image planes. However, it is possible that a co-expression of e.g. a fluorescent marker protein like GFP is suitable also for detecting the expression level of a product. Then the already implemented fluorescence plane scanning could readily be used for determination of the expression level. That would be a distinct advantage because it is difficult to measure the expression level manually, at this state of the development.

Another application of a microtiter plate scanning extension would be the possibility to carry out simple media optimization experiments in microtiter plates alongside a daily non-invasive measurement of cell number and viability. Cell cultivation in microtiter-plates and generation of growth-functions of every well would allow numerous experiments to be carried out in parallel. This could not be realized with small-scale bioreactors because of the expenditure of manpower. After cultivation, a simple product titer determination would be enough to correlate measured growth-rates and yield. This would help to determine the amount of essential media components that are important for the production process.

---

Before a scanning procedure of microtiter-plates can be realized some problems have to be solved:

The current autofocus is not suitable for scanning the complete plate before the actual measurement starts, because the autofocus is too slow. A way to overcome this problem might be the development of an edge detection algorithm that scan only some edges of the microtiter plate and measures the changes of light refraction of these edges during scanning in the vertical direction. With them, it should be possible to detect the spatial position of the plate.

Another problem is the meniscus of the liquid in the well that refracts light into the plane of detection. This light leads to an inhomogeneous background illumination that can be corrected either mathematically or by using special microtiter plate covers to prevent refraction.

#### 6.8.5. Binding assays with spherical agarose beads

At present, the system has been constructed only for the measurement of cell specific parameters, but it is quite possible that the system can detect any other objects that have similar optical properties to mammalian cells. First experiments has been done with HiTrap Protein A Sepharose beads from Pharmacia with an average particle size of 34  $\mu\text{m}$ . These spherical crosslinked agarose beads contain covalently attached protein A using a N-hydroxysuccinimide coupling method. The swollen gel beads have a binding capacity for human IgG of approximately 20 mg/ml drained gel. The idea is to use these beads as miniature "test sticks" to detect the amount of produced antibody. When these beads are mixed with a cell sample, protein A can bind the antibody, produced by the cells. With a second fluorescence labeled antibody that also bind to protein A or the previously bound antibody, the amount of bound antibody could be quantified by a FullScan of only the fluorescence plane.

## 7. Literature

- |   |      |   |                 |   |
|---|------|---|-----------------|---|
| <b>Bettger W. J., Ham R. G.</b>   | 1982 | The Nutrient Requirements of Cultured Mammalian Cells   | 4, 249-288      | Adv. Nutr. Res.   |
| <b>Al-Rubeai M.</b>   | 1996 | Apoptosis and Cell Culture Technology   | 59:225-249      | Advances in Biochemical Engineering                                     |
| <b>Al-Rubeai M., Mills D., Emery A. N.</b>  | 1990 | Electron microscopy of hybridoma cells with special regard to monoclonal antibody production  | 4: 13-28        | Cytotechnology  |
| <b>Barnes M. L., Bentley C. M., Dickson A. J.</b>   | 2001 | Characterization of the Stability of Recombinant Protein Production in the GS-NS0 Expression System   | 73,4,261-270    | Biotech. & Bioeng.  |
| <b>Bedner E., Darzynkiewicz Z., Burfeind P., Gorczyca W., Melamed M. R.</b>                     | 1997 | Laser Scanning Cytometry Distinguishes Lymphocytes, Monocytes and Granulocytes by Differences in Their Chromatin Structure                          | 29:191-196      | Cytometry   |
| <b>Bedner E., Li X., Gorczyca W., Melamed M. R., Darzynkiewicz Z.</b>                           | 1999 | Analysis of Apoptosis by Laser Scanning Cytometry   | 35:181-195      | Cytometry   |
| <b>Belloc F., Dumain P., Boisseau M. R., Jalloustre C., Reiffers J., Bernard P., Lacombe F.</b> | 1994 | A Flow Cytometric Method Using Hoechst 33342 and Propidium Iodide for Simultaneous Cell Cycle Analysis and Apoptosis Determination in Unfixed Cells | 17:59-65        | Cytometry   |
| <b>Bierau H., Perani A., Al-Rubeai M., Emery A. N.</b>  | 1998 | A comparison of intensive cell culture bioreactors operating with hybridomas modified for inhibited apoptotic response                              | 62, 195-207     | Journal of Biotechnology  |
| <b>Boehm G., Knoll C., Colomer V. G., Alcaniz-Raya M., Albalat S.</b>                           | 1999 | Three-dimensional segmentation of bone structures in CT images  | 3661,1, 277-286 | Proceedings of SPIE - The international Society for Optical Engineering |
| <b>Bolt P.</b>  | 2000 | Entwicklung und Optimierung einer automatisierbaren Methode zur optischen Detektion zellkulturspezifischer Parameter in tierischen Zellkulturen     | Diplomarbeit    | Technische Universität Berlin   |
| <b>Bömmel H., Duschl A.</b>   | 2001 | Biopharmaka der zweiten Generation  | 1-2/2001        | Bioforum  |
| <b>Bortner C. D., Oldenburg B. E., Cidlowski J. A.</b>  | 1995 | The role of DNA fragmentation in apoptosis  | 5:21            | Trends in Cell Biology  |

<b>Cohen J.</b>	1993	Overview: mechanisms of apoptosis	14,3:126-130	Immunology Today
<b>Darzynkiewicz Z., Juan G., Li X., Gorczyca W., Murakami T., Traganos F.</b>	1997	Cytometry in Cell Necrobiology: Analysis of Apoptosis and Accidental Cell Death (Necrosis)	21:1-20	Cytometry
<b>Darzynkiewicz Z., Traganos F.</b>	1998	Measurement of Apoptoses	62:33-73	Advances in Biochemical Engineering
<b>De Hauwer C., Darro F., Camby I., Kiss R., Van Ham P., Decaestecker C.</b>	1999	In Vitro Motility of Evaluation of Aggregated Cancer Cells by Means of Automatic Image Processing	36:1-10	Cytometry
<b>deZengotita V. M., Miller W. M., Aunins J. G., Zhou W.</b>	2000	Phosphate Feeding Improves High-Cell-Concentration NS0 Myeloma Culture Performance for Monoclonal Antibody Production	69, 5, 566-576	Biotech. & Bioeng.
<b>Dhir D., Morrow K. J., Rhinehart R. R., Wiesner T.</b>	2000	Dynamic Optimization of Hybridoma Growth in a Fed-Batch Bioreactor	76,2; 197-205	Biotech. & Bioeng.
<b>Dive C., Darzynkiewicz Z., Ormerod M.</b>	1995	Measurement of Apoptosis by Flow Cytometry	Book	Tutorial Rimini ISAC XVII
<b>Dutton R. L., Scharer J. M., Moo-Young M.</b>	1998	Descriptive parameter evaluation in mammalian cell culture	26:139-154	Cytotechnology
<b>Faraday D. B. F., Hayter P., Kirkby N. F.</b>	2001	A mathematical model of the cell cycle of a hybridoma cell line	7: 49-68	Biochemical Engineering Journal
<b>Frame K. K., Hu W. S.</b>	1990	The loss of antibody productivity in continuous culture of hybridoma cells	35, 469-476	Biotech. & Bioeng.
<b>Goswami J., Sinskey A. J., Steller H., Stephanopoulos G. N., Wang D. I. C.</b>	1999	Apoptosis in Batch Cultures of Chinese Hamster Ovary Cells	62,6:632-640	Biotech. & Bioeng.
<b>Grindley J., Ogden J.</b>	1999	Protein drugs prove increasingly promising	Oct. 99	???
<b>Kenn, Rapson</b>	1995	Development of a serum-free culture medium for the large scale production of recombinant protein from a Chinese hamster ovary cell line	17: 153-163	Cytotechnology
<b>Konstantinov K. B., Aarts R., Yoshida T.</b>	1993	Expert Systems in bioprocess Control: requisite Features	48: 169-191	Advances in Biochemical Engineering
<b>Kravtsov V. D., Fabian I.</b>	1996	Automated monitoring of apoptosis in suspension cell cultures	Vol. 74. No. 2, p. 577	Laboratory Investigation

- |  |      |  |                 |                                  |
|--|------|--|-----------------|----------------------------------|
| <b>Kromenaker S. J.,<br/>Srienc F.</b>   | 1994 | Stability of Producer Hybridoma Cell Lines After Sorting: A Case Study   | 10:299-307      | Biotechnol. Progress             |
| <b>Malpica N., Ortiz de Solórzano C., Vaquero J. J., Santos A., Vallcorba I., Garcia-Sagred J. M., del Pozo F.</b> | 1997 | Applying Watershed Algorithms to the Segmentation of Clustered Nuclei  | 28:289-297      | Cytometry                        |
| <b>Martelli A. M., Bortul R., Fackelmayer F. O., Tazzari P. L., Bareggi R., Narducci P., Zweyer M.</b>             | 1999 | Biochemical and Morphological Characterization of the Nuclear Matrix From Apoptotic HL-60 Cells  | 72:35-46        | Journal of Cellular Biochemistry |
| <b>Maruhashi F.,<br/>Murakami S., Baba K.</b>  | 1994 | Automated monitoring of cell concentration and viability using an image analysis system  | 15: 281-289     | Cytotechnology                   |
| <b>Mastrangelo A. J.,<br/>Hardwick J. M., Zou S., Betenbaugh M. J.</b>   | 2000 | Part II. Overexpression of bcl-2 Family Members Enhances Survival of Mammalian Cells in Response to Various Culture Insults                            | 67,5;555-564    | Biotech. & Bioeng.               |
| <b>Medarex Inc.</b>  | 2001 | Medarex Research Information   | www.medarex.com | Internet                         |
| <b>Meneses-Acosta A.,<br/>Mendonca R. Z.,<br/>Merchant H.,<br/>Covarrubias L.,<br/>Ramirez O. T.</b>               | 2001 | Comparative Characterization of Cell Death Between Sf9 Insect Cells and Hybridoma Cultures   | 72, 4, 441-457  | Biotech. & Bioeng.               |
| <b>Moore A., Donahue C. J., Hooley J., Stocks D. L., Bauer K. D., Mather J. P.</b>                                 | 1995 | Apoptosis in CHO cell batch cultures: examination by flow cytometry  | 17:1-11         | Cytotechnology                   |
| <b>Moore A., Mercer J., G. Dutina, C. J. Donahue, K. D. Bauer, J. P. Mather, T. Etcheverry, T. Ryll</b>            | 1997 | Effects of temperature shift on cell cycle, apoptosis and nucleotide pools in CHO cell batch cultures  | 23:47-54        | Cytotechnology                   |
| <b>Olsson L.,Schulze U.,<br/>Nielsen J.</b>  |      | On-line bioprocess monitoring - an academic discipline or an industrial tool?  | 17,2: 88-95     | Trends in analytical chemistry   |
| <b>Patel S. D.,<br/>Papoutsakis E. T.,<br/>Winter J. N., Miller W. M.</b>  | 2000 | The Lactate Issue Revisited: Novel Feeding Protocols To Examine Inhibition of Cell Proliferation and Glucose Metabolism in Hematopoietic Cell Cultures | 16: 885-892     | Biotechnol. Progress             |
| <b>Pläsier B., Lloyd D. R.,<br/>Paul G. C., Thomas C.</b>  | 1999 | Automatic image analysis for quantification of apoptosis in animal cell culture by annexin-V   | 229:81-95       | Journal of Immunological Methods |

<b>R., Al-Rubeai M.</b>		affinity assay		
<b>Price J. H., Gough D. A.</b>	1994	Comparison of Phase-Contrast and Fluorescence Digital Autofocus for Scanning Microscopy	16: 283-297	Cytometry
<b>Reed J. C.</b>	1998	Bcl-2 family proteins	17:3225-3236	Oncogene
<b>Rettmann M. E., Han X., Prince J. L.</b>	2000	Watersheds on the cortical surface for automated sulcal segmentation	20-27	Proceedings of the Workshop on Mathematical Methods in Biomedical Image Analysis
<b>Sabri S., Richelme F., Pierres A., Benoliel A-M., Bongrand P.</b>	1997	Interest of image processing in cell biology and immunology	208:1-27	Journal of Immunological Methods
<b>Sauer P. W., Burky J. E., Wesson M. C., Sternard H. D., Qu L.</b>	2000	A High-Yielding, Generic Fed-Batch Cell Culture Process for Production of Recombinant Antibodies	67:5; 585-597	Biotech. & Bioeng.
<b>Schügerl K.</b>	2001	Progress in monitoring, modeling and control of bioprocesses during the last 20 years	85, 149-173	Journal of Biotechnology
<b>Seifert D., Phillips J. A.</b>	1999	The Production of Monoclonal Antibody in Growth-Arrested Hybridomas Cultivated in Suspension and Immobilized Modes	15, 655-666	Biotechnol. Progress
<b>Sgonc R., Wick G.</b>	1994	Methods for the Detection of Apoptosis	105:327-332	Int. Arch Allergy Immunol.
<b>Simpson N. H., Milner, Al-Rubeai M.</b>	1997	Prevention of Hybridoma Cell Death by bcl-2 During Suboptimal Culture Conditions	54,1:1-16	Biotech. & Bioeng.
<b>Simpson N. H., Singh R. P., Perani A., Goldenzon C., Al-Rubeai M.</b>	1998	In Hybridoma Cultures, Deprivation of Any Single Amino Acid Leads to Apoptotic Death, Which is Suppressed by the Expression of the bcl-2 Gene	59,1:90-98	Biotech. & Bioeng.
<b>Singh R. P., Emery A. N., Al-Rubeai M.</b>	1996	Enhancement of Survivability of Mammalian Cells by Overexpression of the Apoptosis-Suppressor Gene bcl-2	52:166-175	Biotech. & Bioeng.
<b>Singh R.P., Al-Rubeai M.</b>	1997	Apoptosis and its control in cell culture systems	23:87-93	Cytotechnology
<b>Singh R.P., Al-Rubeai M.</b>	1998	Apoptosis and Bioprocess Technology	62:167-184	Advances in Biochemical Engineering
<b>Singh R.P., Al-Rubeai M., Gregory C. D., Emery A. N.</b>	1994	Cell Death in Bioreactors: A Role for Apoptosis	44:720-726	Biotech. & Bioeng.
<b>Soille P.</b>	1998	Morphologische Bildverarbeitung	Book	Springer-Verlag Berlin

<b>Soille P., Vincent L.</b>	1990	Determining watersheds in digital pictures via flooding simulations	SPIE Vol. 1360 240-250	Visual Communications and Image Processing
<b>Tey B. T., Singh R. P., Piredda L., Piacentini M., Al-Rubeai M.</b>	1999	Influence of Bcl-2 on Cell Death During the Cultivation of Chinese Hamster Ovary Cell Line Expressing a Chimeric Antibody	68:1,31-43	Biotech. & Bioeng.
<b>Thomas C. R., Paul G. C.</b>	1996	Applications of image analysis in cell technology	7:35-45	Current Opinion in Biotechnology
<b>Umesh Adiga P. S., Chaudhuri B. B.</b>	1999	Region based techniques for segmentation of volumetric histo-pathological images	61, 23-47	Computer Methods and Programs in Biomedicine
<b>van Adrichem J. H. M.</b>	1997	Monitoring of cell biological mechanisms of cell death in production cel lines	Diss ETH Nr. 12142	Eidgenössische Technische Hochschule Zürich
<b>Varley J., Birch J.</b>	1999	Reactor design for large scale suspension animal cell culture	29:177-205	Cytotechnology
<b>Vincent L, Soille P.</b>	1991	Watersheds in Digital Spaces: An Efficient Algorithm Based on Immersion Simulations	13, 6	IEEE Transactions on Pattern Analysis and Machine Intelligence
<b>Vollath D.</b>	1988	The influence of the scene parameters and of noise on the behavior of automatic focusing algorithms	152,2: 133-146	Journal of Microscopy
<b>Walter R. J., Berns M. W.</b>	1981	Computer-enhanced video microscopy: digitally processed microscope images can be produced in real time	Nov;78(11): 6927-31	Proc. Natl. Acad. Sci. USA
<b>Weber G. F., Daley J., Kraeft S-K., Chen L. B., Cantor H.</b>	1997	Measurement of Apoptosis in Heterogenous Cell Populations	7:136-144	Cytometry
<b>Wegner S., Oswald H., Wust P., Fleck E.</b>	1997	Segmentierung mit der Wasserscheidentransformation	Juni	Spektrum der Wissenschaft
<b>Weisser M., Tieg S., Wendel A., Uhlig S.</b>	1998	Quantification of Apoptotic and Lytic Cell Death by Microscopy in Combination With Artificial Neural Networks	31:20-28	Cytometry
<b>Werner R. G.</b>	2001	Gentechnik in der Arzneimittel-Entwicklung- Biopharmazeutika eröffnen neue Wege der Therapie	Nr. 5	CHEManager
<b>Werner R. G.,Walz F., Konrad A.</b>	1992	Safety and economic aspects of continuous mammalian cell culture	22; 1-2; 51-68	Journal of Biotechnology
<b>Werner R.G.</b>	1998	Innovative and Economic Potential of Mammalian Cell Culture	48:423-426	Arzneim.-Forsch./Drug Res.
<b>Wilkinson M. H. F.</b>	1995	Fluoro-Morphometry-Adding Fluorometry to an Image Processing System for Bacterial	Dissertation	Chemical Engineering and

		Morphometry		Processing
<b>Wit P., Busscher H. J.</b>	1998	Application of an artificial neural network in the enumeration of yeasts and bacteria adhering to solid substrata	32, 281-290	Journal of Microbiological Methods
<b>Xie L., Wang D. I. C.</b>	1994	Fed-Batch Cultivations of Animal Cells Using Different Medium Design Concepts and Feeding Strategies	43,11; 1175-1189	Biotech. & Bioeng.
<b>Xie L., Wang D. I. C.</b>	1994	Applications of improved stoichiometric model in medium design and fed-batch cultivation of animal cells in bioreactor	15: 17-29	Cytotechnology
<b>Yi J., Park H-S., Ra J. B.</b>	1999	Semantic object segmentation scheme for X-ray body images	3661, II, 094-910	Proceedings of SPIE - The international Society for Optical Engineering
<b>Zalewski K.</b>	1995	Entwicklung eines Bildanalyse-Systems zur on-line Charakterisierung von Hefesuspensionen	17, 127	Fortschritt-Berichte VDI
<b>Zalewski K., Buchholz R.</b>	1996	Morphological analysis of yeast cells using an automated image processing system	48: 43 -49	Journal of Biotechnology
<b>Zanghi J. A., Fussenegger M., Bailey J. E.</b>	1999	Serum Protects Protein-Free Competent Chinese Hamster Ovary Cells Against Apoptosis Induced by Nutrient Deprivation in Batch Culture	64,1; 108-119	Biotech. & Bioeng.
<b>Zanghi J. A., Schmelzer A. E., Mendoza T. P., Knop R. H., Miller W. M.</b>	1999	Bicarbonate Concentration and Osmolarity Are Key Determinants in the Inhibition of CHO Cell Polysialylation Under Elevated pCO <sub>2</sub> or pH	Vol. 65, No. 2, 182-191	Biotech. & Bioeng.
<b>Zhang Q., Litchfield J. B., Reid J. F., Ren J., Chang S-W.</b>	1995	Coupling a machine vision sensor and a neural net supervised controller: controlling microbial cultivations	38:219-228	Journal of Biotechnology
<b>Zhou W., Chen C-C., Buckland B., Aunins J.</b>	1997	Fed-Batch Culture of Recombinant NS0 Myeloma Cells with High Monoclonal Antibody Production	55,5; 783-792	Biotech. & Bioeng.

## 8. Appendix

### 8.1. Scripts

#### 8.1.1. Fullscan & Processing Script

```

method FULLSCAN & Processing V2.2
// Fullscan and Image Processing Procedure
// last modified 09.01.01
// 04.01.01 reduce syringes speed by 100 steps/s
// 09.01.01 increase flow-through chamber load speed to 200 steps/s
// 16.01.01 new info text
//
comment start full scan
mcu_write (xM12)(yM12)(zM12);
s2_check Full Scan cannot be executed - S2 is empty
button Bitte Fluoreszenz-Lampe einschalten (Schalter Steckerleiste Video & Mikro)
form
button Insert Sample, please
comment fill tube from inlet to V3 with sample
hamc 01Vv1w270G
hamc 01Pp60s50G
comment discarding tube rinse
hamc 01Vv0w0G
hamc 03Vv0w0G
hamc 01Dd60t50G
comment DAPI to mixer
s2_count -1
hamc 02Vv0w0G
hamc 02Dd100t100G
comment Loading sample
hamc 01Vv1w270G
hamc 01Pp400s50G
comment mixing - back to sample tube
hamc 01Dd400t50G
comment Loading sample for staining
hamc 01Vv1w270G
hamc 01Pp400s50G
comment Need Help !
button Plunge sample tube into EtOH, please

```

```

comment deliver sample (and DAPI) to mixer
hamc 01Vv0w0G
hamc 03Vv0w60G
hamc 02Vv0w90G
hamc 01Dd400t50G
comment incubation time - waiting 60 seconds
wait 60
comment sample + DAPI to S1
hamc 03Vv0w120G
hamc 01Pp400s50G
comment sample to chamber (speed 200 steps/s)
hamc 01Vv0w0G
hamc 03Vv1w240G
hamc 01Dd400t200G
comment Sedimentation Phase - Waiting 180 Seconds
wait 180
comment starting FULL Scan Procedure
wait 2
comment Full Scan in progress
fullscan
processing
// CIP Script for cleaning the entire liquid system
// Version 1.5
// last modified 04.01.01
// copy of CIP complete cleaning 04.01.01
//
comment Starting Cleaning Procedure
comment empty sampletube 1 of 2
hamc 01Vv1w270G
hamc 01Pp400s100G
hamc 01Vv0w0G
hamc 03Vv0w0G
hamc 01Dd400t200G
comment empty sampletube 2 of 2
hamc 01Vv1w270G
hamc 01Pp400s100G
hamc 01Vv0w0G
hamc 03Vv0w0G
hamc 01Dd400t200G
comment Loading mixer with CIP solution via mixer top
hamc 03Vv0w180G
hamc 01Vv0w0G
hamc 01Pp1000s100G
hamc 03Vv0w60G
hamc 02Vv0w90G
hamc 01Dd1000t200G
comment Loading chamber with CIP solution
hamc 03Vv0w180G

```

```
hamc 01Vv0w0G
hamc 01Pp400s100G
hamc 03Vv0w240G
hamc 01Dd400t200G
comment Cleaning Mixer - Waiting 10 seconds
wait 10
comment Loading mixer with H2O via mixer top 1 of 1
hamc 03Vv0w300G
hamc 01Vv0w0G
hamc 01Pp1000s100G
hamc 03Vv0w60G
hamc 02Vv0w90G
hamc 01Dd1000t200G
comment Loading mixer with H2O via mixer bottom 1 of 3
hamc 03Vv0w300G
hamc 01Vv0w0G
hamc 01Pp1000s100G
hamc 03Vv0w120G
hamc 01Dd1000t200G
comment Loading mixer with H2O via mixer bottom 2 of 3
hamc 03Vv0w300G
hamc 01Vv0w0G
hamc 01Pp1000s100G
hamc 03Vv0w120G
hamc 01Dd1000t200G
comment Loading mixer with H2O via mixer bottom 3 of 3
hamc 03Vv0w300G
hamc 01Vv0w0G
hamc 01Pp1000s100G
hamc 03Vv0w120G
hamc 01Dd1000t200G
comment empty mixer via mixer bottom
hamc 03Vv0w120G
hamc 01Pp1000s100G
hamc 03Vv1w0G
hamc 01Dd1000t200G
comment Loading mixer with H2O via mixer top
hamc 03Vv0w300G
hamc 01Vv0w0G
hamc 01Pp1000s100G
hamc 03Vv0w60G
hamc 02Vv0w90G
hamc 01Dd1000t200G
comment Loading mixer with H2O via mixer bottom 1 of 2
hamc 03Vv0w300G
hamc 01Vv0w0G
hamc 01Pp1000s100G
hamc 03Vv0w120G
hamc 01Dd1000t200G
comment Loading mixer with H2O via mixer bottom 2 of 2
hamc 03Vv0w300G
hamc 01Vv0w0G
hamc 01Pp1000s100G
hamc 03Vv0w120G
hamc 01Dd1000t200G
comment empty mixer via top
hamc 03Vv0w60G
hamc 02Vv0w90G
hamc 01Pp1000s100G
hamc 03Vv0w0G
hamc 01Dd1000t200G
comment empty mixer 1 of 2 via bottom
hamc 03Vv0w120G
hamc 01Pp1000s200G
hamc 03Vv0w0G
hamc 01Dd1000t200G
comment waiting for rinse
wait 10
comment empty mixer 2 of 2 via bottom
hamc 03Vv0w120G
hamc 01Pp1000s200G
hamc 03Vv0w0G
hamc 01Dd1000t200G
comment chamber: cleaning with water - 1. time
hamc 03Vv0w300G
hamc 01Pp1000s100G
hamc 03Vv0w240G
hamc 01Dd1000t200G
comment chamber: cleaning with water - 2. time
hamc 03Vv0w300G
hamc 01Pp1000s100G
hamc 03Vv0w240G
hamc 01Dd1000t300G
comment chamber: cleaning with water - 3. time
hamc 03Vv1w300G
hamc 01Vv0w0G
hamc 01Pp1000s100G
hamc 03Vv1w240G
hamc 01Dd1000t300G
beep
comment cleaning complete
```

### 8.1.2. SnapScan Script

```
method long time study with DAPI staining
comment start long time study
mcu_write (xM12)(yM12)(zM12);
s2_check Full Scan cannot be executed - S2 is empty
button Bitte Fluoreszenz-Lampe einschalten (Schalter Steckerleiste Video & Mikro)
form
button Insert Sample, please
comment fill tube from inlet to V3 with sample
hamc 01Vv1w270G
hamc 01Pp60s50G
comment discarding tube rinse
hamc 01Vv0w0G
hamc 03Vv0w0G
hamc 01Dd60t50G
comment DAPI to mixer
s2_count -1
hamc 02Vv0w0G
hamc 02Dd100t100G
comment Loading sample
hamc 01Vv1w270G
hamc 01Pp400s50G
comment mixing - back to sample tube
hamc 01Dd400t50G
comment Loading sample for staining
hamc 01Vv1w270G
hamc 01Pp400s50G
button Plunge sample tube into EtOH, please
comment deliver sample (and DAPI) to mixer
hamc 01Vv0w0G
hamc 03Vv0w60G
hamc 02Vv0w90G
hamc 01Dd400t50G
comment incubation time - waiting 60 seconds
wait 60
comment sample + DAPI to S1
hamc 03Vv0w120G
hamc 01Pp400s50G
```

```
comment sample to chamber
hamc 01Vv0w0G
hamc 03Vv1w240G
hamc 01Dd400t200G

button sample is loaded
mcu_write (xM13)(yM13)(zM13);
button please position stage and nosepiece manually and press OK
mcu_write (xM12)(yM12)(zM12);

comment taking bright field picture (first)
snap_dt_abs auto,0,0,60,100,both

comment clean the staining system
comment loading sample tube with EtOH
hamc 01Vv1w270G
hamc 01Pp500s200G
hamc 01Vv0w0G
hamc 03Vv0w0G
hamc 01Dd500t300G
comment loading syringe 1 with H2O
hamc 03Vv1w300G
hamc 01Vv0w0G
hamc 01Pp1000s200G
comment discarding water
hamc 01Vv0w0G
hamc 03Vv0w0G
hamc 01Dd1000t300G
comment Cleaning with CIP-Solution
hamc 03Vv0w180G
hamc 01Vv0w0G
hamc 01Pp400s200G
hamc 03Vv0w240G
hamc 01Dd400t200G
comment Cleaning in Progress - waiting 2 seconds
wait 2
comment Filling Chamber with water (1 of 2)
hamc 03Vv0w300G
hamc 01Pp1000s200G
```

```
hamc 03Vv0w240G
hamc 01Dd1000t300G
comment Cleaning with H2O - waiting 2 seconds
wait 2
comment Filling Chamber with water (2 of 2)
hamc 03Vv0w300G
hamc 01Pp1000s200G
hamc 03Vv0w240G
hamc 01Dd1000t300G
comment script ended
```

-

## 8.2. Labview Source Code

### 8.2.1. "Out of focus" algorithm

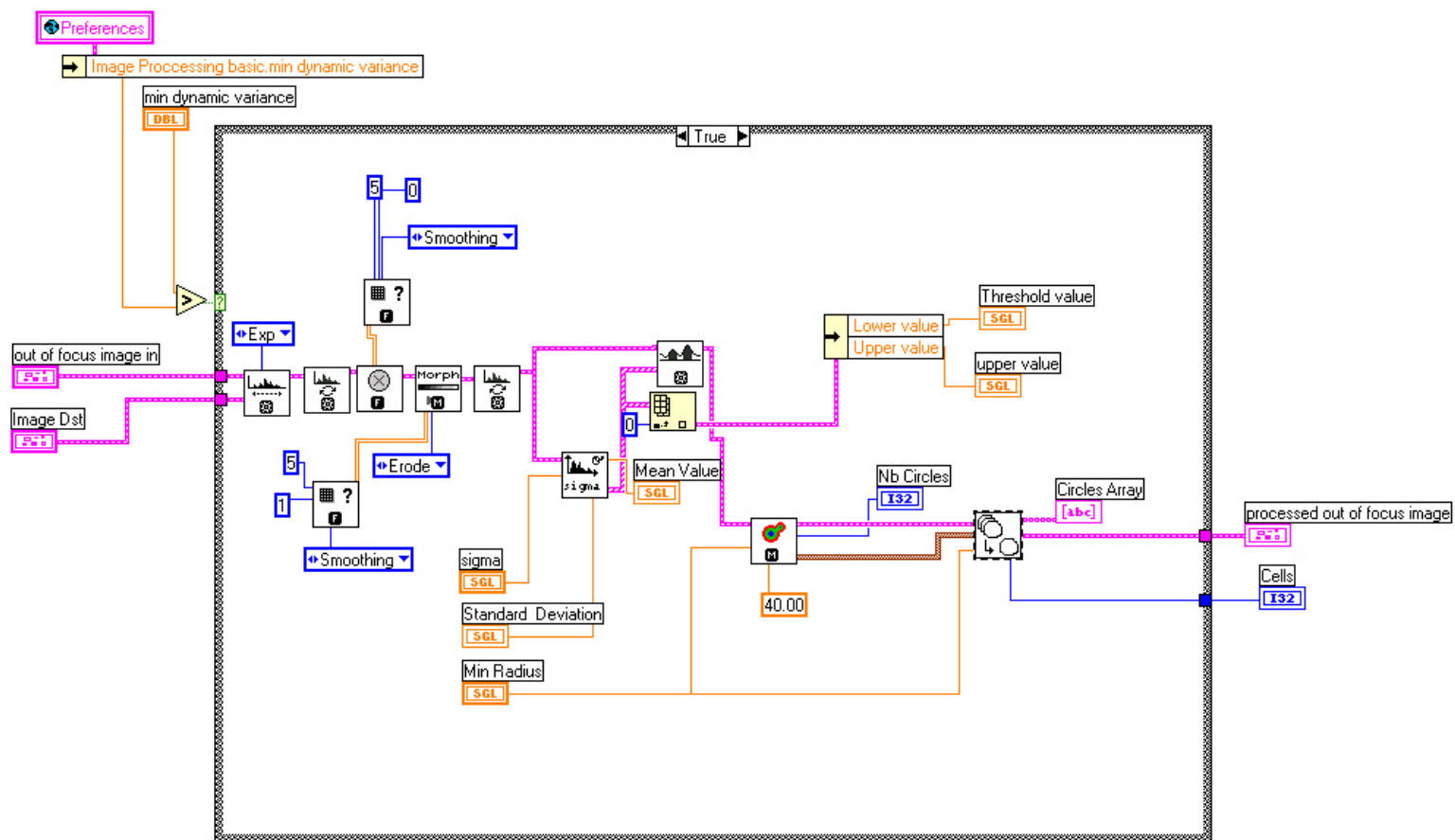


Fig. 8-1 Labview source code "out of focus" algorithm

8.2.2. Focus Functions - Source code

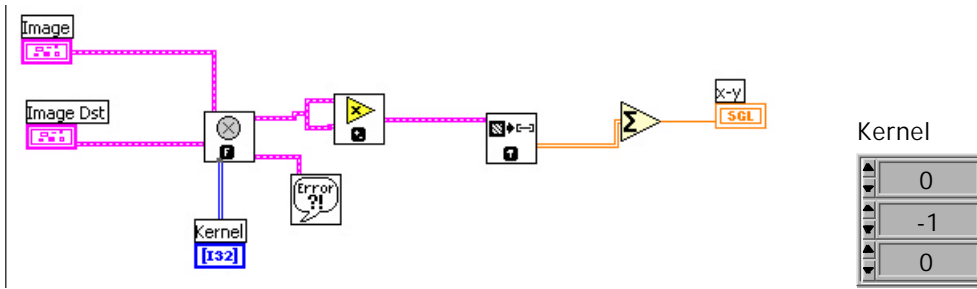


Fig. 8-2 Labview source code of focus function F1

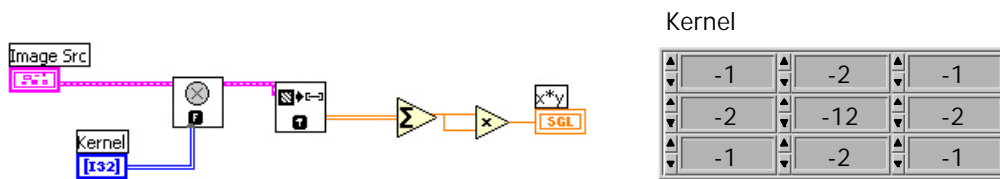


Fig. 8-3 Labview source code of focus function F4

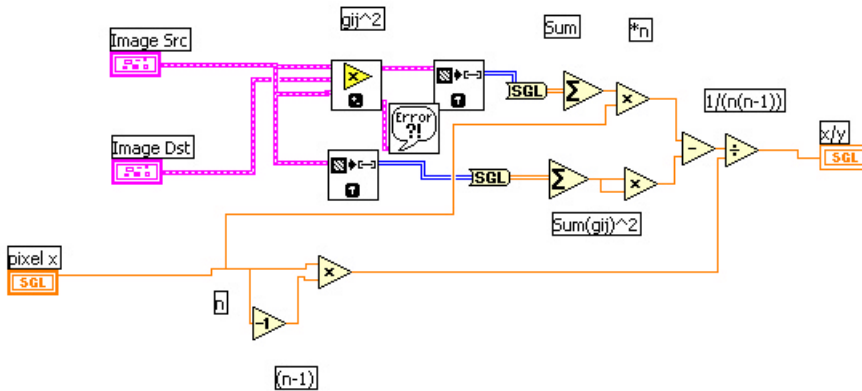


Fig. 8-4 Labview source code of focus function F5

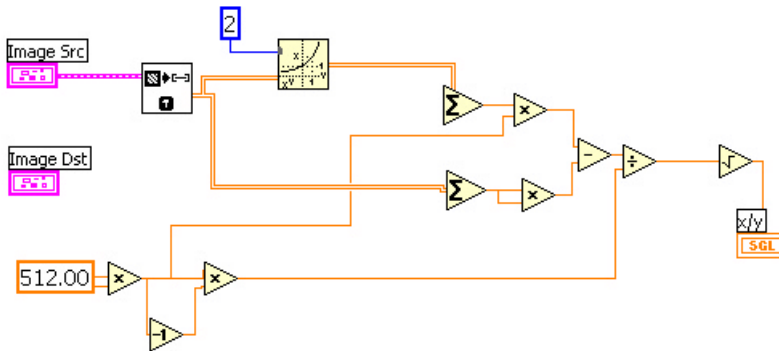


Fig. 8-5 Labview source code of focus function F6

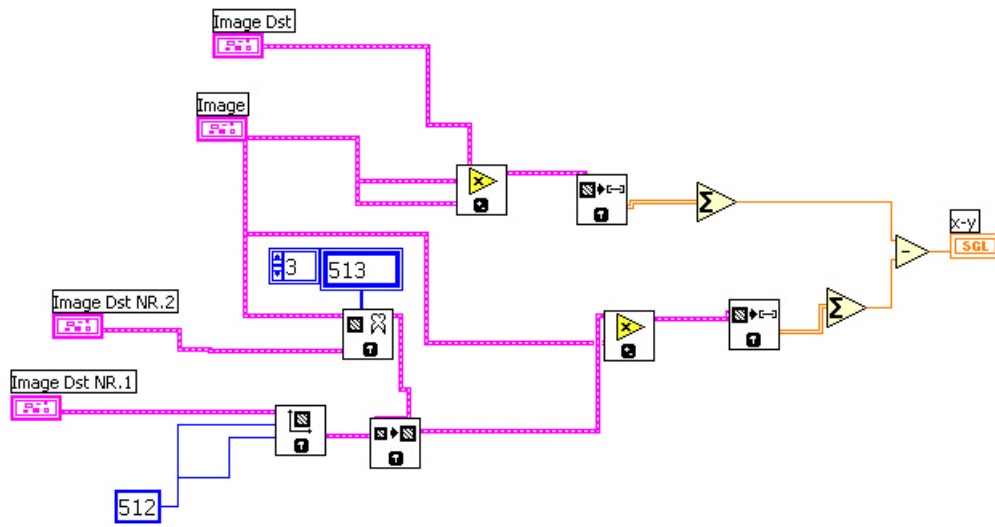


Fig. 8-6 Labview source code of focus function F9

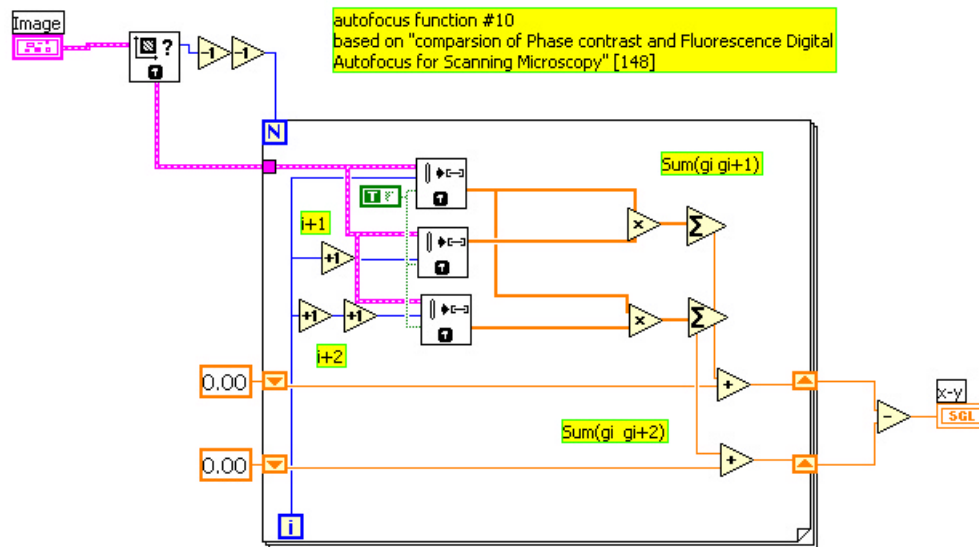


Fig. 8-7 Labview source code of focus function F10

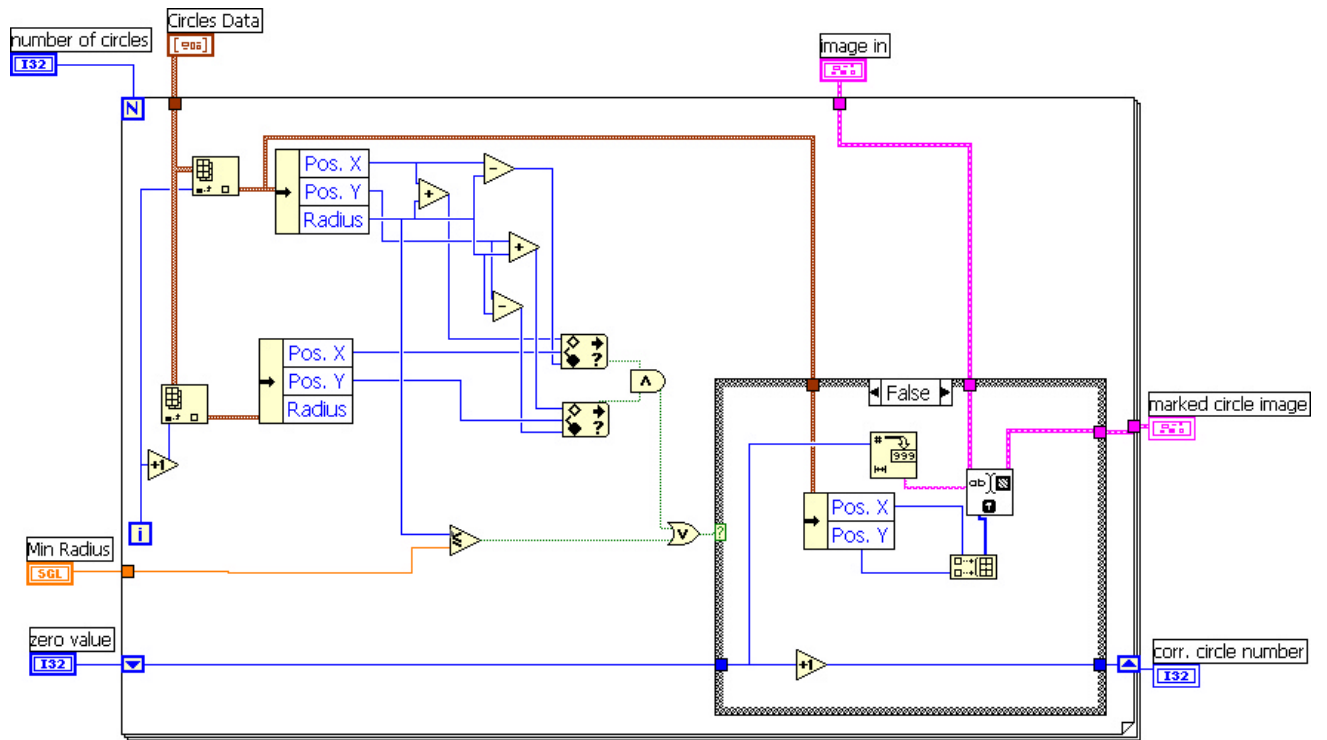


Fig. 8-8 Labview source code: circle function correction algorithm